The Dissertation Committee for Charles Davis Burton
certifies that this is the approved version of the following dissertation:

Measurement of J/ψ meson production in association with a $W^{\pm}$ boson in pp data at $13\,\mathrm{TeV}$ collected by the ATLAS Experiment

Committee:

Peter Onyisi, Supervisor

Timothy R Andeen Jr

Can Kilic

Mike Boylan-Kolchin

Christina Markert

Measurement of J/ψ meson production in association with a $W^{\pm}$ boson in pp data at $13\,\mathrm{TeV}$ collected by the ATLAS Experiment

by

Charles Davis Burton

DISSERTATION

Presented to the Faculty of the Graduate School of

The University of Texas at Austin

in Partial Fulfillment

of the Requirements

for the Degree of

DOCTOR OF PHILOSOPHY

THE UNIVERSITY OF TEXAS AT AUSTIN

August 2022

Dedicated to Noodle.

Acknowledgments

The presence of just one name on the byline is misleading: I could not have done this without the support, guidance, and resources provided by family, friends, and colleagues alike.

My thanks begin with my parents, Jay and Brenda Burton. Without their strong investment of time and effort into my education—from youth into adulthood—none of this would have been possible. I thank the rest of my family for their constant love and support.

I have been fortunate to have inspirational and knowledgeable teachers throughout my life. During my undergraduate years, Matthias Liepe and Anders Ryd offered me fruitful opportunities and positive guidance in the earliest stages of my research work.

Undoubtedly, the most important individual in my development as a scientist is my advisor, Peter Onyisi. He gave me both detailed guidance and wide latitude for independent discovery, which has allowed me to explore and understand the fantastic breadth and depth of experimental particle physics. I thank him for always being willing to follow the details of my work, guiding me when I was lost, and always asking thought-provoking questions. My professional development as a scientist is uniquely attributable to his efforts.

Of course, I am thankful to the entire LHC staff and the ATLAS Collaboration for the successful operation of the accelerator and detector. The data I analyzed were only available with their long-term support. I appreciate the vast computing resources made available by US ATLAS, without which I could not have performed significant components of this measurement. I especially thank the following past and present ATLAS Collaborators: Tim Andeen, Harish Potti, Aaron Webb, Avik Roy, Mesut Unal, Devanshu Panchal, Marc Tost, Michelle Contreras, Lauren Larson, Rohin Narayan, Kyungeon Choi, and Kevin Barends.

My friends, both in Austin and around the country, provided comradery, inspiration, and fun. Especially, I thank Jordan, Natalie, Erin, Bea, Ace, Brant, Greg, Suzanne, Steven, Laura, Jared, Roger, Micah, and Michelle.

Finally, I am grateful to my partner, Hannah Stahl. Whether I was progressing or stuck, eager or frustrated, content or confused, she has been there to cheer me on and bounce ideas off. I could not have done this without her.

Measurement of J/ψ meson production in association with a $W^{\pm}$ boson in pp data at $13\,\text{TeV}$ collected by the ATLAS Experiment

by

Charles Davis Burton, Ph.D.
The University of Texas at Austin, 2022

Supervisor: Peter Onyisi

This dissertation presents a measurement of the production cross-section of J/ψ mesons in association with a $W^{\pm}$ boson in $\sqrt{s} = 13\,\text{TeV}$ pp collisions by the ATLAS experiment, using $139\,\text{fb}^{-1}$ of integrated luminosity produced by the Large Hadron Collider at CERN. Events are selected with $W^{\pm} \rightarrow \ell^{\pm}\nu$ and $J/\psi \rightarrow \mu^{+}\mu^{-}$. The ratio of the prompt $J/\psi + W^{\pm}$ cross-section to the inclusive $W^{\pm}$ cross-section is presented for J/ψ transverse momenta in the range $8 - 200\,\text{GeV}$ and rapidity $\left|y_{J/\psi}\right| < 2.1$, and is presented as a differential measurement as a function of J/ψ transverse momenta and rapidity. Comparisons are made with theoretical predictions for single-parton and double-parton production events.

Table of Contents

Acknowledgments **5**

Abstract **7**

List of Tables **12**

List of Figures **14**

Chapter 1. Introduction **20**

1.1 Quantum Field Theory 20
1.2 Experimental Predictions and Tests 21
1.3 Perturbation Theory 24
1.4 The Limits of Perturbation Theory 25
1.5 Quantum Chromodynamics 27
1.6 Quarkonia in QCD 28
1.7 Tests of NRQCD Models 30
1.8 Prompt $J/\psi + W^{\pm}$ Production 32
1.9 Double-parton Scattering 32
1.10 Summary 35

Chapter 2. Experimental Setup **37**

2.1 CERN 37
2.2 The LHC 38
2.2.1 LHC Beams 38
2.2.2 Accelerator Technology 40
2.2.3 Beam Structure 42
2.2.4 Collisions 42
2.3 The ATLAS Detector 44
2.3.1 Detector Design Philosophy 44

2.3.2 Magnet System 46
2.3.3 Inner Detector 47
2.3.4 Calorimeters 51
2.3.5 Muon Spectrometer 58
2.3.6 Trigger, Readout, and Data Acquisition 61

Chapter 3. Event Reconstruction **65**
3.1 Tracking 66
3.2 Calorimeter Clusters 68
3.3 Electrons 68
3.4 Muons 70
3.4.1 Low-p_{T} Muons 71
3.5 Jets 72
3.6 Missing Transverse Energy 73
3.6.1 Soft $E_{\mathrm{T}}^{\mathrm{miss}}$ 74
3.7 Overlap Removal 76

Chapter 4. Monte Carlo Generation and Simulation **78**
4.1 Matrix Element Generators 78
4.2 General-purpose Event Generators 80
4.3 Detector Response Simulation 82
4.4 Monte Carlo Simulation Samples 83
4.4.1 Inclusive $W^{\pm}$ Samples 84
4.4.2 QCD Multi-jet Sample 84
4.4.3 Associated $J/\psi + W^{\pm}$ Samples 85
4.4.4 SPS Generator Parameters 86

Chapter 5. Data and Event Selection **88**
5.1 Run 2 Dataset 88
5.2 Trigger Selection 88
5.3 Event Selection 91
5.4 Inclusive $W^{\pm}$ Selection 91
5.5 Associated $J/\psi + W^{\pm}$ Selection 93
5.6 Yields 94

Chapter 6. Signal Extraction and Background Estimation **96**
6.1 Prompt J/ψ Extraction 96
6.1.1 J/ψ Vertex Finding 99
6.1.2 Efficiency and Acceptance Corrections 103
6.2 Associated $J/\psi + W^{\pm}$ Background Estimations 104
6.2.1 QCD Multi-jet 104
6.2.2 Prompt $J/\psi + Z$ 106
6.2.3 Simultaneous QCD multi-jet and prompt $J/\psi + Z$ Fit 107
6.2.4 Pileup 111
6.3 Inclusive $W^{\pm}$ Background Estimations 112

Chapter 7. Single and Double Parton Scattering **115**
7.1 Distinguishing Observables 115
7.2 $\Delta\varphi\,(J/\psi, W^{\pm})$ for DPS estimation 116
7.3 $E_{\mathrm{T}}^{\mathrm{miss}}$ Reconstruction Bias 117
7.3.1 Hadronic Recoil Acceptance 118
7.3.2 Effects on Reconstructed $E_{\mathrm{T}}^{\mathrm{miss}}$ 120
7.3.3 Effects on $\Delta\varphi\,(J/\psi, W^{\pm})$ 121
7.4 Other Angular Variables 122

Chapter 8. Systematic Uncertainties **129**
8.1 Prompt J/ψ Model 129
8.2 Lepton Background Estimations 130
8.3 Inclusive $W^{\pm}$ Backgrounds 132
8.4 $W^{\pm}$ Acceptance and Efficiency 132
8.5 Muon Reconstruction Efficiency 134
8.6 J/ψ Spin Alignment 134
8.7 Summary and Ranking 134

Chapter 9. Results and Conclusions **138**

Appendices **141**

Appendix A. Data Tables **142**

Bibliography **146**

Vita **157**

List of Tables

4.1 List of Monte Carlo samples used for studies of inclusive W production. 84
4.2 List of Monte Carlo samples used for studies of associated W production. Predicted cross-sections have large theoretical uncertainties, and are not listed. 85
4.3 LDMEs for SPS production. The values differ because the two generators use different conventions for defining these model parameters. 87

5.1 Good run lists and measured luminosities for Run 2 pp collision data-taking periods. 89
5.2 Summary of the lowest unprescaled single-lepton triggers used in this analysis to identify a $W^{\pm}$ candidate. The trigger naming conventions are described in the body. 90
5.3 Selection criteria used to identify $W^{\pm}$ candidates in inclusive and associated events. 92
5.4 J/ψ selection criteria. 93
5.5 Pair selection criteria. 94

6.1 Mass-τ model used to generate s-weights for associated events. 98
6.2 The QCD multi-jet background is largely eliminated by using a number of cuts, which are listed here. 106
6.3 The data are divided into six selections regions. Region A is rich in signal, region D is rich in QCD multi-jet background, and region F is rich in prompt $J/\psi + Z$. The other three regions are mixtures. 107

8.1 List of systematic uncertainties considered in the analysis. . . 135

A.1 QCD multi-jet background estimates for the electron channel. Backgrounds are estimated by fitting the data in each p_{T}/y bin to a sum of DPS, $b\bar{b}$, and Z templates. 143

A.2 Prompt $J/\psi + Z$ background estimates for the electron channel. Backgrounds are estimated by fitting the data in each p_{T}/y bin to a sum of DPS, $b\bar{b}$, and Z templates. 143
A.3 QCD multi-jet background estimates for the muon channel. Backgrounds are estimated by fitting the data in each p_{T}/y bin to a sum of DPS, $b\bar{b}$, and Z templates. 144
A.4 Prompt $J/\psi + Z$ background estimates for the muon channel. Backgrounds are estimated by fitting the data in each p_{T}/y bin to a sum of DPS, $b\bar{b}$, and Z templates. 144
A.5 Measured ratio of the associated $J/\psi + W^{\pm}$ production cross-section to the inclusive $W^{\pm}$ production cross-section in the electron channel. Values are reported differentially in J/ψ transverse momentum and rapidity. 145
A.6 Measured ratio of the associated $J/\psi + W^{\pm}$ production cross-section to the inclusive $W^{\pm}$ production cross-section in the muon channel. Values are reported differentially in J/ψ transverse momentum and rapidity. 145

List of Figures

1.1 The QCD factorization theorem allows one to apply field theoretic calculations of elementary particle interactions to the collision of composite hadrons. 23

1.2 The parton distribution functions produced by the NNLO MSHT20 analysis. PDFs are shown at two different scales, $\mu^2 = 10\,\mathrm{GeV}^2$ (left) and $\mu^2 = 10^4\,\mathrm{GeV}^2$ (right). Image courtesy of Ref. [7]. . . 24

1.3 Theoretical predictions using the SM are compared to experimental measurements performed by ATLAS, for a variety of processes. Figure courtesy of Ref. [21]. 26

1.4 The value of the QCD coupling constant (α_s) as a function of energy scale (Q). At the energy scale of the charm quark mass, α_s becomes large, and perturbation theory becomes imprecise. Figure courtesy of Ref. [7]. 28

1.5 Double-parton scattering, where multiple parton-parton interactions occur in the same proton-proton collision, can occur at the LHC. QCD factorization theorems can be applied to DPS interactions. 33

1.6 Measurements of σ_eff for DPS production across a variety of production channels. Evidence suggests that the value of σ_eff is process-dependent and energy-independent. Figure courtesy of Ref. [52]. 35

2.1 The accelerator complex at CERN uses a series of linear and circular accelerators to generate a beam of charged particles and accelerate it to high energies. Image courtesy of Ref. [57]. 39

2.2 SRF cavities generate large electric fields, which are used to accelerate a beam of charged particles. Image courtesy of Ref. [58]. 40

2.3 Cross-section of an LHC dipole magnet. Superconducting magnets are used to guide the beam around the accelerator ring. Image courtesy of Ref. [59]. 41

2.4 Cut-away diagram of the ATLAS detector with its various subdetector components. 45

2.5 Diagram of the ATLAS magnet system. Image courtesy of Ref. [71]. 47

2.6 Schematic of the barrel components of the ATLAS inner detector. Image courtesy of Ref. [62]. 48

2.7 Schematic of the endcap components of the ATLAS inner detector. Image courtesy of Ref. [62]. 48

2.8 Cutaway diagram of the ATLAS calorimetry system. Image courtesy of Ref. [62]. 52

2.9 Cells for the ATLAS Liquid Argon Calorimeter. Image courtesy of Ref. [62]. 53

2.10 Cumulative amount of material, in units of interaction lengths, as a function of $|\eta|$. This includes the ID, all calorimeters, and all services. Image courtesy of Ref. [62]. 54

2.11 Schematic of one Tile Calorimeter module. Image courtesy of Ref. [62]. 56

2.12 Diagram of layout of the absorbing and active material within the forward calorimeter, as viewed along the direction of the beam line. Image courtesy of Ref. [62]. 57

2.13 Diagram of the ATLAS Muon Spectrometer, with the various components labelled. Image courtesy of Ref. [62]. 59

2.14 Diagram of one MDT chamber. Drift tubes are stacked a few layers deep to form a multi-layer. Two multi-layers are attached to a support structure to form one chamber. Image courtesy of Ref. [62]. 59

2.15 Layout of the anode wires and cathode strips in one CSC cell. Left: view looking down the direction of the wires (towards the beam pipe). Right: view looking perpendicular to the direction of the wires and parallel to the cathode strips. 60

2.16 The ATLAS Trigger system showing the trigger decision paths and data flow. A low-level trigger identifies events that may have included a hard process. Those events and their ROIs are passed to higher-level triggers. Events passing an HLT are read out and stored. 62

3.1 Electron identification efficiency in Run 2 data as a function of transverse energy (left) and pseudo-rapidity (right). The "Tight" working point was used the analysis presented here. Images courtesy of Ref. [86]. 69

3.2 Muon identification efficiency in Run 2 data as a function of transverse momentum (left) and pseudo-rapidity (right). The "Tight" working point was used in the analysis presented here. Images courtesy of Ref. [87]. 71

3.3 Muon identification efficiency for the Low-Pt reconstruction algorithm in Run 2 data as a function of transverse momentum and pseudo-rapidity. Image courtesy of Ref. [87]. 72

3.4 Performance of the $E_{\mathrm{T}}^{\mathrm{miss}}$ calculation in simulated $Z \to \mu\mu$ events. The calo-based soft $E_{\mathrm{T}}^{\mathrm{miss}}$ term degrades the overall $E_{\mathrm{T}}^{\mathrm{miss}}$ resolution, especially in high pileup (large N_{PV}) conditions (left). The hadronic recoil activity is not accurately incorporated, leading to a bias of a few GeV (right). Images courtesy of Ref. [88]. 75

4.1 A visualization of an event generated using Sherpa. This event includes proton fragmentation, a hard collision, hadron formation, and parton showering. Image courtesy of Ref. [100]. . . . 81

5.1 Efficiency of the combined single-lepton triggers as a function of the transverse energy or momentum of the fully reconstructed object. Images courtesy of Refs. [118] and [119]. 91

5.2 Cutflow diagram for the selections described in the previous sections. 95

6.1 Distribution of J/ψ candidate mass and τ for events passing the associated selections. These events include prompt, non-prompt, and combinatorial background. 97

6.2 Projections of 2D fit in a single p_T/y bin onto the mass (top) and pseudo-proper time (bottom) dimensions. Components show the relative contributions of J/ψ signal (prompt and non-prompt) and combinatorial background. 100

6.3 Projections of 2D fits integrated across the twelve J/ψ p_T/y bins and projected onto the mass and pseudo-proper time dimensions. Components show the relative contributions of J/ψ signal (prompt and non-prompt) and combinatorial background. 101

6.4 Pulls of the sum of the twelve independently-performed 2D fits of the data to the model. The fits were found to perform well, especially in the region near the prompt J/ψ signal peak. . . . 102

6.5 Muon efficiency maps for each of the four years of data-taking, calculated as a function of muon p_{T} and η. 103

6.6 J/ψ acceptance maps as a function of $p_{\mathrm{T}}^{J/\psi}$ and $y^{J/\psi}$. Acceptance values are calculated for a variety of spin-alignment profiles. Additionally, the bottom-right plot shows the ratio of the largest value of the seven acceptance maps to the smallest value in each bin. 105

6.7 Estimations of the QCD multi-jet and prompt $J/\psi + Z$ background in the electron channel, summed over all bins. A template fit is performed to the s-weighted data to determine the signal fraction in the analysis region (A). 109

6.8 Estimations of the QCD multi-jet and prompt $J/\psi + Z$ background in the muon channel, summed over all bins. A template fit is performed to the s-weighted data to determine the signal fraction in the analysis region (A). 110

6.9 The pileup is estimated by fitting a Gaussian PDF to the wide component of the Δz_0 distribution in the region $|\Delta z_0| > 3\,\text{mm}$, and extrapolating to the region at $|\Delta z_0| < 0.5\,\text{mm}$. 111

6.10 Estimation of the electroweak and QCD multi-jet backgrounds in the electron channel. A template fit is performed to the inclusive $W^{\pm}$ data to determine the signal fraction in the analysis region (A). 113

6.11 Estimation of the electroweak and QCD multi-jet backgrounds in the electron channel. A template fit is performed to the inclusive $W^{\pm}$ data to determine the signal fraction in the analysis region (A). 114

7.1 Distributions of $\Delta\varphi\,(J/\psi, W^{\pm})$, the azimuthal angle separation between J/ψ and $W^{\pm}$, using reconstruction and truth information. SPS shapes are produced with the `HelacOnia` MC generator. 117

7.2 Vector sum of truth particle p_{T} in inclusive J/ψ production, projected onto the J/ψ momentum axis. On top, no selections have been applied. On the bottom, only particles with $|\eta| < 2.5$ and $q \neq 0$ are included. With those selections, a bias which peaks at 6 GeV in the direction of the J/ψ is observed. 119

7.3 Negative of the reconstructed $E_{\text{T}}^{\text{miss}}$ vector, projected onto the J/ψ axis, in inclusive J/ψ production. The observed bias is consistent with excluding forward and neutral particles in the hadronic recoil. 120

7.4 A schematic of the effects of a bias in the $E_{\text{T}}^{\text{miss}}$. Even a small bias opposite the direction of the J/ψ can vastly change the reconstructed value of $\Delta\varphi\,(J/\psi, W^{\pm})$ for soft $W^{\pm}$ bosons. . . . 121

7.5 MC samples are used to produce templates of the variable $\Delta y\,(J/\psi, \ell^{\pm})$ for SPS and DPS. The templates for data and MC are shown in each analysis bin. 123

7.6 MC samples are used to produce templates of the variable $\Delta\varphi\,(J/\psi, \ell^{\pm})$ for SPS and DPS. The templates for data and MC are shown in each analysis bin. 124

7.7 MC samples are used to produce two-dimensional templates of the variables $\Delta y\,(J/\psi, \ell^{\pm})$ and $\Delta\varphi\,(J/\psi, \ell^{\pm})$ for DPS and SPS. The distribution in data is fit to a weighted sum of the templates. The projection onto the $\Delta y\,(J/\psi, \ell^{\pm})$ axis is shown here. 125

7.8 MC samples are used to produce two-dimensional templates of the variables $\Delta y\,(J/\psi, \ell^{\pm})$ and $\Delta\varphi\,(J/\psi, \ell^{\pm})$ for DPS and SPS. The distribution in data is fit to a weighted sum of the templates. The projection onto the $\Delta\varphi\,(J/\psi, \ell^{\pm})$ axis is shown here. 126

7.9 MC samples are used to produce two-dimensional templates of the variables $\Delta y\,(J/\psi, \ell^{\pm})$ and $\Delta\varphi\,(J/\psi, \ell^{\pm})$ for DPS and SPS. The distribution in data is fit to a weighted sum of the templates. For the three fitted yield parameters, 1σ, 2σ, and 3σ confidence intervals are shown. 127

7.10 MC samples are used to produce two-dimensional templates of the variables $\Delta y\,(J/\psi, \ell^{\pm})$ and $\Delta\varphi\,(J/\psi, \ell^{\pm})$ for DPS and SPS. The distribution in data is fit to a weighted sum of the templates. The fractional yields are shown here. 128

8.1 The systematic uncertainty originating from the QCD multi-jet MC template is estimated by scaling up the template normalization to match the data in validation region C, as seen here. 131

8.2 The systematic uncertainty originating from cancellation of the $W^{\pm}$ acceptance is estimated using a DPS MC sample. The ratio of selected to generated events is shown as a function of $p_{\mathrm{T}}^{W^{\pm}}$. 133

8.3 Ranking of systematic and statistical uncertainties in the electron channel. 136

8.4 Ranking of systematic and statistical uncertainties in the muon channel. 137

9.1 Measured ratio of the associated $J/\psi + W^{\pm}$ production cross-section to the inclusive $W^{\pm}$ production cross-section in the electron channel. Error bars on the data show the combination of statistical and systematic uncertainties. Shaded regions show the uncertainty due to the unknown spin alignment profile of the J/ψ. 139

9.2 Measured ratio of the associated $J/\psi + W^{\pm}$ production cross-section to the inclusive $W^{\pm}$ production cross-section in the electron channel. Error bars on the data show the combination of statistical and systematic uncertainties. Shaded regions show the uncertainty due to the unknown spin alignment profile of the J/ψ. 139

9.3 The measured cross-section ratio is compared to a model of double-parton scattering. The value of $\sigma_{\mathrm{eff}} = 9.2\,\mathrm{mb}$ is chosen so that the lowest $p_{\mathrm{T}}^{J/\psi}$ bin is saturated with DPS. The $p_{\mathrm{T}}^{J/\psi}$ distribution from DPS does not agree with data in all bins, suggesting the presence of an SPS contribution. 140

Chapter 1

Introduction

Experimental elementary-particle physics is the study of the fundamental building blocks of matter and their interactions. Physicists mathematically describe subatomic particles and their interactions using fields, within a framework called Quantum Field Theory (QFT). The Standard Model (SM) of particle physics [1–3] is one such field theory, which is constructed to explain more parts of physical reality than any other single theory. While it has succeeded at predicting a vast array of particles and phenomena across an enormous range of energy scales, the SM is considered incomplete, since it does not explain some experimentally-observed objects and phenomena like gravity, dark matter, and neutrino masses.

1.1 Quantum Field Theory

Quantum Field Theory is a mathematical framework which combines quantum mechanics with special relativity. In it, the fundamental elements of the universe are "fields," and the elementary particles associated with a field are treated as quantized excitations of that field. The dynamics of each field and the interactions between two or more fields are modeled by constructing a Lagrangian. The Lagrangian of any theory contains a set of fields, some interaction terms which govern how those fields interact, and a set of parameters (called coupling constants) which control the relative strength of those interactions.

1.2 Experimental Predictions and Tests

QFT is used to make predictions of observable quantities. Perhaps most prominently, it is used to calculate the probability of a specific particle interaction process to occur in a given collision. Based on an analogy to classical physics, this interaction probability is called a "cross-section" and has units of area. Cross-sections are denoted with the symbol σ.

The process for deriving a predicted cross-section from a given Lagrangian is detailed in a number of standard texts (e.g. Refs. [4] and [5]), so I will provide only a broad overview here. The probability of a scattering process occurring is proportional to the square of the matrix element $\mathcal{M}$. The matrix element, analogous to a scattering amplitude in ordinary quantum mechanics, is calculated using the interacting term of the S-matrix, which itself depends on the exponential of the interacting part of the Lagrangian. That is, very roughly,

$$\sigma \propto |\mathcal{M}|^2 \propto \left|\left\langle f \left| e^{i\int_{-\infty}^{\infty} dt\mathcal{L}_{\mathrm{int}}(t)} \right| i \right\rangle\right|^2 . \tag{1.1}$$

Essentially, given a field theory, one can predict the probability of an interaction occurring—i.e. a scattering cross-section.

One of the most robust ways to experimentally test the SM is with particle colliders. By colliding two or more particles together, one can directly observe their interactions. Then, the theoretically-predicted cross-sections can be compared to the experimentally-observed values. In order to probe the laws of physics at very small distances (much smaller than the size of an atom), these collisions must occur at very high energies.

Hadron colliders do not immediately fit into this scheme since they do not directly collide *elementary* particles. Instead, they collide composite particles such as protons. However, by using the QCD factorization theorem [6], one can still apply field-theoretic calculations to predict cross-sections in hadron collisions. This is done by factorizing a hadron collider cross-section into (a) the fragmentation of hadrons into the constituent point-like partons—where each parton carries a fraction of the hadron's longitudinal momentum—and (b) the interactions of those partons in the manner described by Eq. 1.1. This factorization of the cross-section of a collision of 2 hadrons is expressed as

$$\sigma_{2\to n} = \sum_{i,j} \int_0^1 dx_i \int_0^1 dx_j f_i\left(x_i\right) f_j\left(x_j\right) \hat{\sigma}_{ij}. \tag{1.2}$$

In this equation, $\hat{\sigma}_{ij}$ are the cross-sections of the parton-level interactions. These are weighted by the parton distribution functions (PDFs) $f(x)$, which return the probability of a given parton carrying a momentum fraction x. The QCD factorization of a hadronic interaction is shown diagrammatically in Figure 1.1.

The PDFs are determined experimentally—primarily via deep inelastic

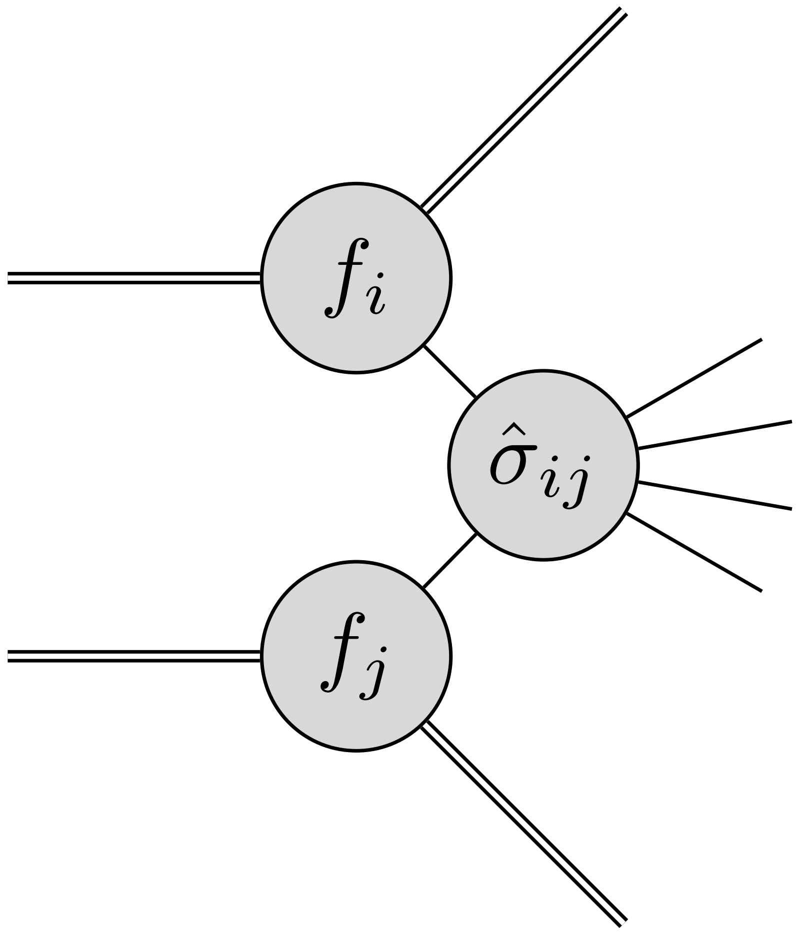

Figure 1.1: The QCD factorization theorem allows one to apply field theoretic calculations of elementary particle interactions to the collision of composite hadrons.

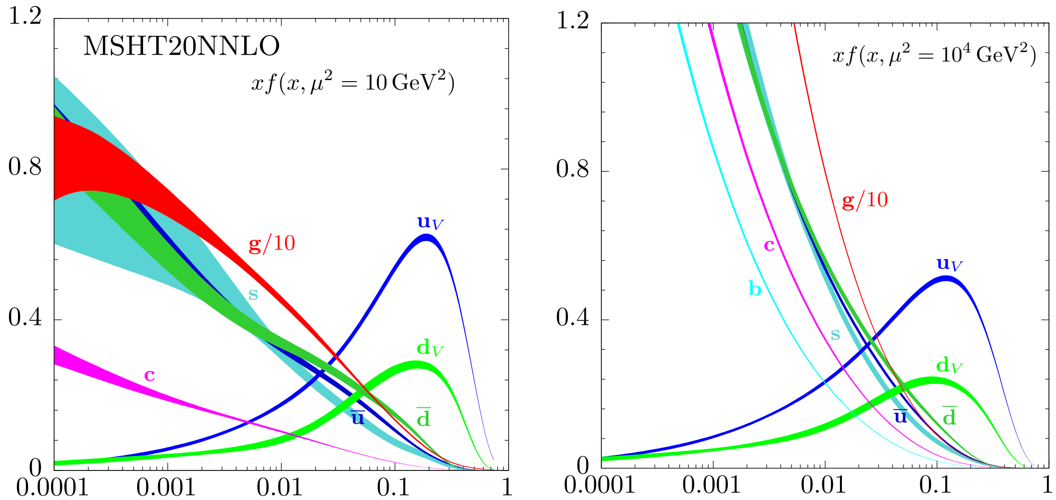

Figure 1.2: The parton distribution functions produced by the NNLO MSHT20 analysis. PDFs are shown at two different scales, $\mu^2 = 10\,\mathrm{GeV}^2$ (left) and $\mu^2 = 10^4\,\mathrm{GeV}^2$ (right). Image courtesy of Ref. [7].

lepton-nucleon scattering experiments. For a detailed review, see [8–14]. A number of groups have produced PDFs from a fit to many experimental results [15–19]. The most recent PDF determinations of the various groups have shown good agreement with one another. The PDFs generated by the MSHT group are shown in Figure 1.2.

1.3 Perturbation Theory

In a given QFT, if a coupling constant in a Lagrangian is small, the S-matrix (and consequently the cross-section) can be expanded in terms of increasing powers of that quantity. The terms in this series expansion are commonly visualized using Feynman Diagrams [20]. One can then add up the contributions of all of these Feynman diagrams to some fixed order in perturbation theory; the resulting quantity is then directly related to the probability of some input-to-output transition occurring.

In practice, cross-section calculations are performed numerically. A computer program called a "matrix element generator" is provided a set of Feynman rules (derived from a given Lagrangian), a set of coupling parameters, a set of input particles, the momenta of those input particles, and a set of output particles. The program then predicts the probability of such a transition occurring.[1] Experimentalists replicate these conditions in the laboratory by colliding particles and experimentally measuring the probability of some transition. This has proven an exceptionally successful strategy for particle physicists: the Standard Model has been used to accurately predict cross-sections across at least twelve orders of magnitude [21], as shown in Figure 1.3.

1.4 The Limits of Perturbation Theory

The perturbative expansion of a cross-section does not provide accurate results at every energy scale. The problem stems from the fact that (despite the name) coupling constants are not constant, but are instead energy-dependent. Moreover, it has been demonstrated that, at some finite energy scale, the coupling constants of any local field theory (including the SM Lagrangian) become infinite [22]. This divergence is referred to as a Landau Pole. For

[1] `MadGraph` and `Sherpa` are examples of such programs. Their operation is detailed in Chapter 4.

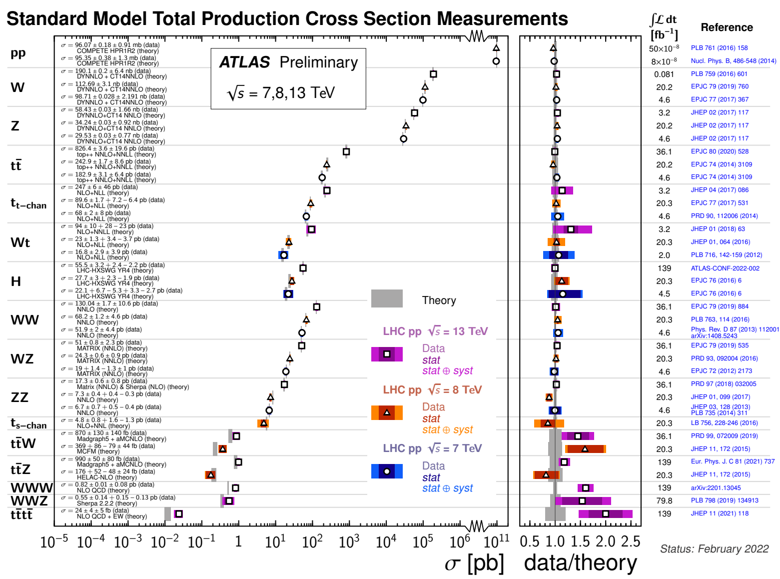

Figure 1.3: Theoretical predictions using the SM are compared to experimental measurements performed by ATLAS, for a variety of processes. Figure courtesy of Ref. [21].

many theories such as quantum electrodynamics (QED) [20], the theory of interactions of charged particles and light, this poses only a minor problem practically: since the energy scale at which QED encounters a divergence (and the Lagrangian can not be perturbatively expanded accurately) is much larger than current experimental reaches [5], high-precision theory predictions can still be made for experimental tests of QED.

1.5 Quantum Chromodynamics

The quantum field theory describing the strong force is quantum chromodynamics (QCD). It has an SU(3) gauge symmetry, with six quark fields that interact through vector gauge bosons called gluons. The QCD Lagrangian is given by

$$\mathcal{L}_{\mathrm{QCD}} = \bar{\psi}_i \left(i\gamma^\mu \left(D_\mu\right)_{ij} - m\delta_{ij} \right) \psi_j - \frac{1}{4} G^a_{\mu\nu} G^{\mu\nu}_a, \tag{1.3}$$

where ψ_i are the quark fields, $\left(D_\mu\right)_{ij} = \partial_\mu \delta_{ij} - i g_s \left(T_a\right) \mathcal{A}^a_\mu$ is the gauge-covariant derivative (which incorporates the coupling constant into the theory for quark-gluon interactions), γ^μ are the Dirac matrices, and $G^a_{\mu\nu}$ are the gluon field strength tensors (which also include the strong force coupling for gluon-gluon interactions). A key property of QCD is that it has "asymptotic freedom" [23]. That is, the coupling constant decreases at high energy scales (or equivalently, short distance scales). Thus, perturbative QCD has been an effective tool for making precision predictions and measurements at relativistic energy scales [24]. On the other hand, the existence of a Landau Pole (Λ_{QCD}) at low

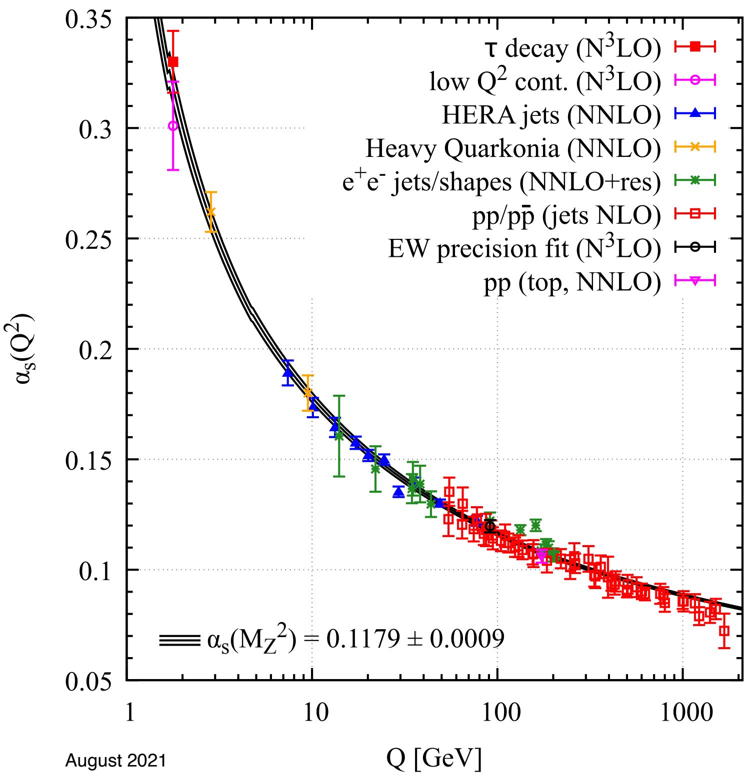

Figure 1.4: The value of the QCD coupling constant (α_s) as a function of energy scale (Q). At the energy scale of the charm quark mass, α_s becomes large, and perturbation theory becomes imprecise. Figure courtesy of Ref. [7].

energy scales (longer distances) makes QCD theory predictions at, for example, the nuclear scale extremely difficult to perform. The value of the coupling constant of QCD is shown in Figure 1.4 across a large range of energy scales.

1.6 Quarkonia in QCD

In principle, QCD should be able to provide an accurate description of the physics of quarks, such as the formation, interactions, and decay of hadrons, which are bound states of multiple quarks. Generally, the energy scales involved in modeling bound states—the quark masses m—lie in the non-perturbative regime of QCD, thus limiting the accuracy of perturbative QCD calculations.

This issues with perturbative modeling of hadrons were partially resolved for the specific case of heavy quarkonia, which are bound states of a charm quark and charm anti-quark (charmonia), or bottom quark and bottom anti-quark (bottomonia).[2] A prominent example of a heavy quarkonium particle is the J/ψ, which is the lightest vector state of charmonium. In the case of heavy quarkonia, the constituent quark mass is much larger than the other energy scale of the theory, Λ_{QCD}. Under that condition, the relative velocity of the quarks is a small number $v \ll 1$, an expansion can be performed in powers of v, and calculations can be efficiently performed. Because the quark velocity is treated as a small expansion parameter, this framework is called non-relativistic QCD (NRQCD).

One prominent use case for the NRQCD framework is to predict the production cross-sections of quarkonia. In this framework, the prediction is factorized into in two steps. First, at the high-energy scale, perturbative QCD is used to model the short-distance production of a pair of heavy quarks ($\mathcal{Q}\bar{\mathcal{Q}}$) with the same momenta. Then, at the low-energy scale, a non-perturbative NRQCD step describes the hadronization of this heavy quark pair into the

[2]Hypothetically, heavy quarkonia particles with top quarks would exist, but the short lifetime of the top quark prevents this state from actually forming.

color-neutral meson that can be observed. In the second step, the transition between the short distance $\mathcal{Q}\bar{\mathcal{Q}}$ production and the final-state meson are governed by long-distance matrix elements (LDMEs). In NRQCD models, the values of the matrix elements are universal parameters which can be determined by fits to experimental data. For the cross-section of producing a quarkonium meson X in a hadron collider, the NRQCD factorization assumption is expressed as

$$\sigma_{2\to X} = \sum_{ijn} \int dx_1 dx_2 f_i(x_1) f_j(x_2) \cdot \hat{\sigma}\left(ij \to \mathcal{Q}\bar{\mathcal{Q}}[n]\right) \cdot \left\langle \mathcal{O}_n^X \right\rangle, \tag{1.4}$$

where n sums over all available $\mathcal{Q}\bar{\mathcal{Q}}$ Fock states ${}^{2S+1}L_J^{[1,8]}$.

1.7 Tests of NRQCD Models

After the first experimental observation of quarkonium states [25, 26], attempts were made to predict their production cross-sections using NRQCD. Initial models used a color-singlet (CS) model, in which the $\mathcal{Q}\bar{\mathcal{Q}}$ state is produced in a color-neutral state with the same quantum numbers as the observed meson. A notable example of this is the attempt to predict the prompt[3] production cross-section of the J/ψ meson [27–29]. However, measurements performed by the CDF Collaboration at the Tevatron showed a large discrepancy between the predicted and observed cross-sections [30, 31]. The observed discrepancies by CDF were especially large (a factor of 50 off from predictions)

[3]Non-prompt J/ψ production from b-decays is typically treated separately.

at high J/ψ transverse momentum (p_T). Similar excesses of J/ψ production in data were observed by the UA1 and D0 Collaborations [32, 33].

The color-octet (CO) mechanism [34–38] was introduced to resolve the observed discrepancy between theory and experiment. In CO models, $\mathcal{Q}\bar{\mathcal{Q}}$ states with a variety of quantum numbers are permitted to hadronize into any available physical quarkonium state via soft gluon emission. The relaxation of the CS quantum number constraints greatly increases the number of available intermediate $\mathcal{Q}\bar{\mathcal{Q}}$ states. The inclusion of these alternate modes in CO models alters the predictions of both the inclusive cross-section and the J/ψ p_T spectrum. The CO LDME parameters are determined using fits to experimental data.

Experimental results from the Large Hadron Collider (LHC) have been used to test models of CS and CO production. All four LHC collaborations—ATLAS, ALICE, CMS, and LHCb—have performed some form of J/ψ cross-section measurement. Using LDME parameters derived from fits to data from the Tevatron, the combined CS and CO predictions were used to predict the prompt J/ψ production cross-section [39–41] with moderate success. Still, other components of the CS and CO models, such as the predicted polarization state of the J/ψ, contradict the observations from the ALICE, CMS, and LHCb [42–44]. After decades of modeling and experimental measurements, the production mechanisms of J/ψ mesons in hadronic collisions are still not well understood.

1.8 Prompt $J/\psi + W^{\pm}$ Production

To better understand CO production modes of quarkonia, one seeks to find a channel in which CO is the dominant production mode. It has been proposed that prompt production of J/ψ mesons associated with a $W^{\pm}$ boson is a clean probe of the CO production mode [45–47]. Others have suggested that the CS effects in the prompt J/ψ+$W^{\pm}$ channel have been underestimated, and the CS contribution will be at least comparable [48].

Measurements of the prompt $J/\psi + W^{\pm}$ cross-section have been performed at 7 TeV and 8 TeV by the ATLAS Collaboration [49, 50]. Now, the ATLAS Run 2 dataset provides the opportunity for a measurement utilizing an unprecedented amount of data in this channel—enough data to provide angular distributions differentially in J/ψ transverse momentum and rapidity. These angular distributions can be used to further test and constrain various models of quarkonia production in high-energy hadron colliders.

1.9 Double-parton Scattering

In any given *pp* collision, the presence of multiple partons introduces the possibility of multi-parton interactions (MPI); see [51] for a comprehensive review. One form of MPI is double parton scattering (DPS), which is a single *pp* collision in which two pairs of partons interact inelastically. A sketch of a DPS interaction is shown in Figure 1.5. Significant theoretical interest in DPS interactions has accompanied the availability of large, high-energy collision datasets produced by LHC experiments.

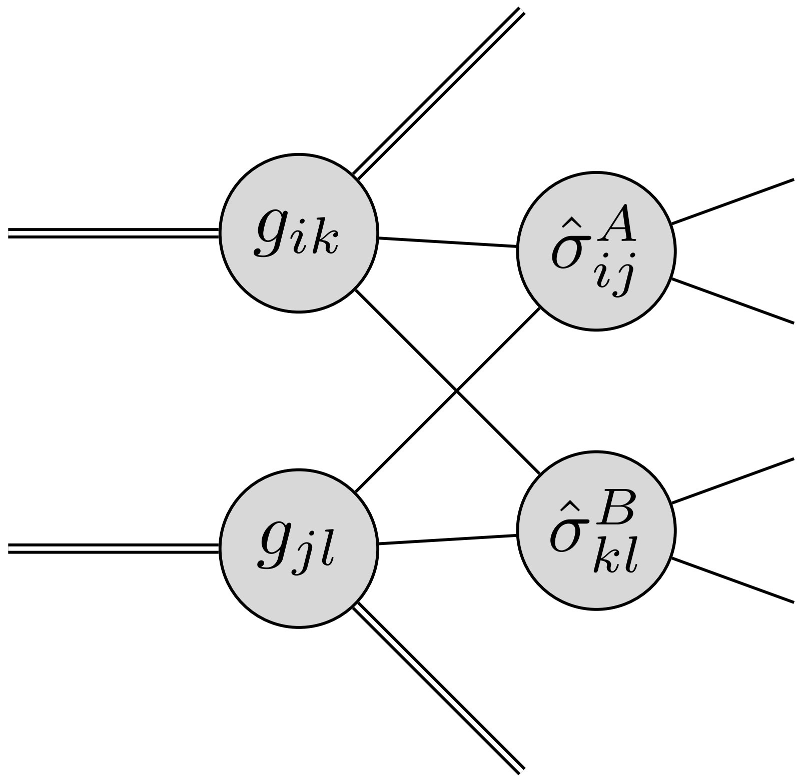

Figure 1.5: Double-parton scattering, where multiple parton-parton interactions occur in the same proton-proton collision, can occur at the LHC. QCD factorization theorems can be applied to DPS interactions.

Just as was done for single-parton scattering (SPS) calculations in Section 1.2, the QCD factorization theorems can be used to predict DPS cross-sections in hadron collisions. In the case of DPS, the PDFs depend on the momentum fractions of each parton, x_i and x_j, as well as the transverse separation between the partons $\mathbf{b}$. The DPS cross-section formula is then given by

$$\sigma_{\text{DPS}}^{AB} = \frac{1}{1+\delta_{AB}} \sum_{ijkl} \int dx_i dx_j dx_k dx_l \hat{\sigma}_{ij}^{A} \hat{\sigma}_{kl}^{B} \int d^2\mathbf{b} g_{ik}(x_i, x_k, \mathbf{b}) g_{jl}(x_j, x_l, \mathbf{b}), \tag{1.5}$$

where δ_{AB} is the Kronecker delta, $\hat{\sigma}_{ij}$ and $\hat{\sigma}_{kl}$ are the usual parton-level cross-sections, g_{ik} and g_{jl} are the double-parton distribution functions, and $\mathbf{b}$ is the transverse distance between the two parton-level processes. In the simplest model of DPS, one assumes that the double-parton distribution functions further factorize as

$$g_{ij}\left(x_i, x_j, \mathbf{b}\right) = f_i\left(x_i\right) f_j\left(x_j\right) G\left(\mathbf{b}\right). \tag{1.6}$$

Using this, Eq. 1.5 reduces to the "DPS pocket formula,"

$$\sigma_{AB}^{\text{DPS}} = \frac{1}{1+\delta_{AB}} \frac{\sigma_A \sigma_B}{\sigma_{\text{eff}}}, \tag{1.7}$$

where σ_A and σ_B are the usual SPS cross-sections for processes A and B, and σ_{eff} is a parameter called the "effective cross-section." The DPS factorization assumption of Eq. 1.6 does not include numerous higher-order effects (all detailed in Ref. [51]), and so σ_{eff} is likely process-dependent and kinematic-dependent.

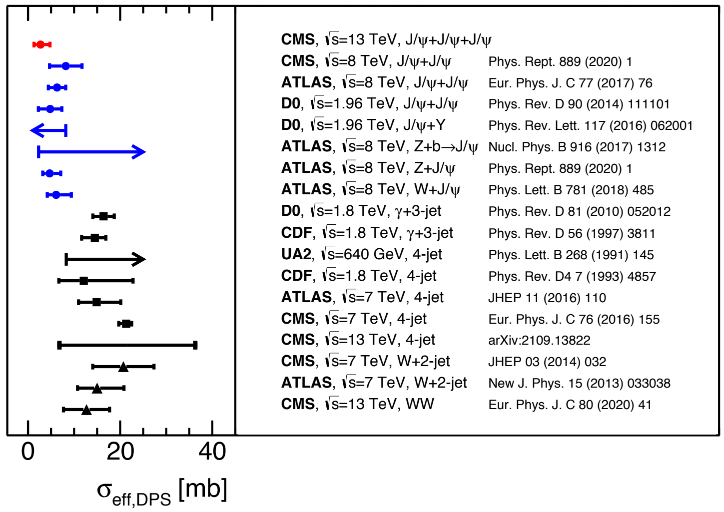

Figure 1.6: Measurements of σ_{eff} for DPS production across a variety of production channels. Evidence suggests that the value of σ_{eff} is process-dependent and energy-independent. Figure courtesy of Ref. [52].

Numerous measurements of DPS processes have been performed in recent years, and values of σ_{eff} have been estimated, albeit each in a model-dependent way. A summary of these measurements is presented in Figure 1.6. Here too, the large ATLAS Run 2 dataset offers an unparalleled opportunity to study DPS production in $J/\psi + W^{\pm}$ events. With angular distributions of events in bins of J/ψ transverse momentum and rapidity, detailed analyses of DPS production mechanisms may be performed.

1.10 Summary

In summary, the measurement of the associated production of prompt J/ψ mesons with $W^{\pm}$ bosons can be used to understand charmonium production mechanisms in hadronic collisions. This cross-section measurement tests models of QCD at the boundary between the perturbative and non-perturbative regimes.

"Prompt" production refers to a J/ψ which is produced directly from the proton-proton collision, or indirectly from the decay of heavier, directly-produced charmonium state (e.g. $\psi(2S) \rightarrow J/\psi$). On the other hand, "non-prompt" production occurs when a J/ψ is produced in the weak decay of a b-hadron (e.g. $B_s \rightarrow J/\psi\phi$). There are multiple modes of prompt associated production: SPS and DPS. In this analysis, I measure the cross-section of the sum of the two modes. Additionally, by providing the distributions of angular separations observed in the data, I suggest how the different modes of production might be experimentally separated.

In this dissertation, I will explain how the ATLAS detector operates, the data are recorded and reconstructed, simulations are produced, events are selected, the signal is extracted, and the backgrounds are estimated. Additionally, I will enumerate and estimate the systematic uncertainties associated with each of these steps. In the end, using the full ATLAS Run 2 dataset, I will present the measured double-differential cross-section ratio of associated $J/\psi + W^{\pm}$ production to inclusive $W^{\pm}$ production,

$$R = \frac{1}{\sigma\left(W^{\pm}\right)} \cdot \frac{d^2\sigma\left(J/\psi + W^{\pm}\right)}{dp_T dy} \cdot \mathcal{B}\left(J/\psi \rightarrow \mu^+\mu^-\right). \tag{1.8}$$

Chapter 2

Experimental Setup

The data presented in this dissertation were generated by the Large Hadron Collider (LHC), a high-energy particle accelerator built by the Conseil Européen pour la Recherche Nucléaire (CERN), and collected by the ATLAS detector, built and operated by the ATLAS Collaboration. In this chapter, I will describe the organizations, accelerator complexes, detectors, and computer networks used to generate, collect, process, and store the data.

2.1 CERN

CERN is a European research organization which provides resources and infrastructure (in the form of lab space, accelerators, and personnel) for elementary-particle physics research. Its main site is on the Franco-Swiss border near the city of Geneva, Switzerland. Since its founding in 1954, the organization has hosted international collaborations formed from research and higher-education institutes in more than 70 countries. Numerous groundbreaking discoveries in nuclear and particle physics research have been made through experiments hosted at CERN.

2.2 The LHC

The LHC [53–56] is an 27 km circular particle accelerator, which is located approximately 100 m underground, beneath the Franco-Swiss border. The LHC is the largest component of a vast particle accelerator network at CERN. The LHC produces two high-energy beams of protons, lead nuclei, and other heavy nuclei.

2.2.1 LHC Beams

The analysis presented in this dissertation uses data collected from the collisions of two proton beams, so I will focus on the production chain for those [56]. Heavy nuclei beams are produced with a slightly different chain. The chain begins with H^- ions, which are provided to a linear accelerator called Linac-4. A strong electric field accelerates the ions to an energy of 160 MeV. The electrons are stripped from the ions as they exit Linac-4. The next stage in the chain involves a sequence of synchrotrons, each of which gradually increases the energy of the beam. The Proton Synchrotron Booster (PSB) increases the beam energy to 2 GeV, the Proton Synchrotron (PS) increases it to 26 GeV, and the Super Proton Synchrotron (SPS) raises it to 450 GeV, which is the injection energy of the LHC. A diagram of the LHC accelerator chain is shown in Figure 2.1.

At last, the proton beams are injected from the SPS into one of two beam pipes of the LHC. One beam circulates clockwise, while the other circulates counter-clockwise. Over the course of approximately 25 minutes, the

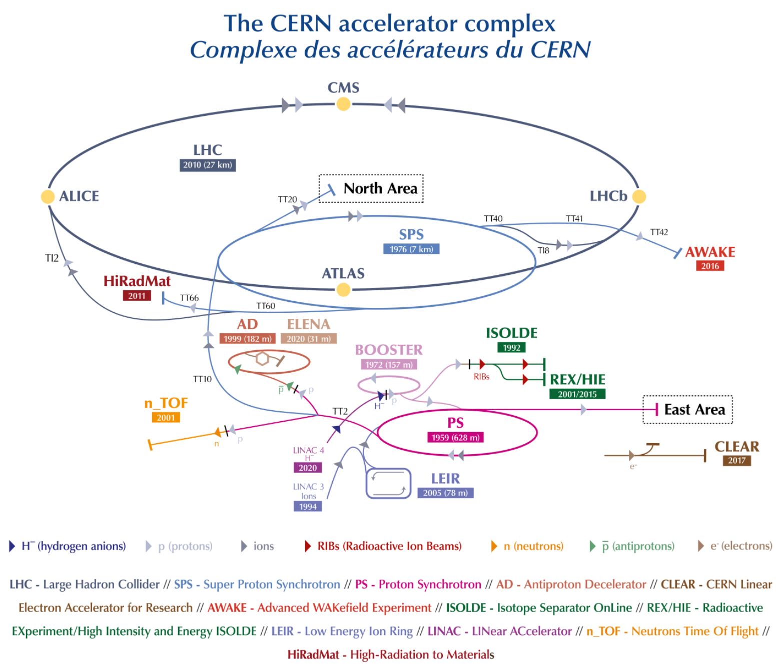

Figure 2.1: The accelerator complex at CERN uses a series of linear and circular accelerators to generate a beam of charged particles and accelerate it to high energies. Image courtesy of Ref. [57].

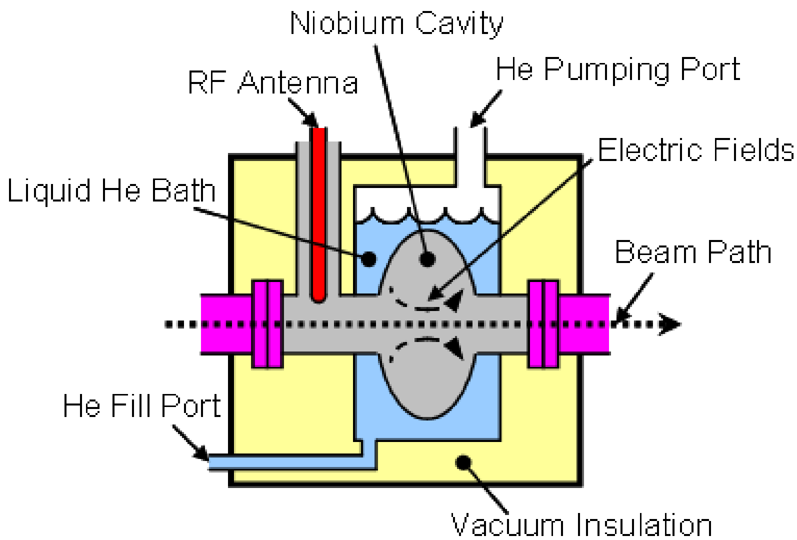

Figure 2.2: SRF cavities generate large electric fields, which are used to accelerate a beam of charged particles. Image courtesy of Ref. [58].

LHC is filled with protons and each beam is accelerated up to an energy of 6.5 TeV, which was the beam energy used in the collection of Run 2 data.

2.2.2 Accelerator Technology

The charged particles used in the collisions are accelerated using strong electric and magnetic fields. The strong electric fields of the linear acceleration steps are generated by creating resonant superconducting radio frequency cavities [60]. A diagram of such a cavity is shown in Figure 2.2. Inside the LHC, the beam is guided around the ring using dipole magnets, and quadrupole magnets are used to control and focus the beam. The LHC magnets are made superconducting by holding them at cryogenic temperatures with liquid helium. A cross-section of an LHC dipole magnet is shown in Figure 2.3.

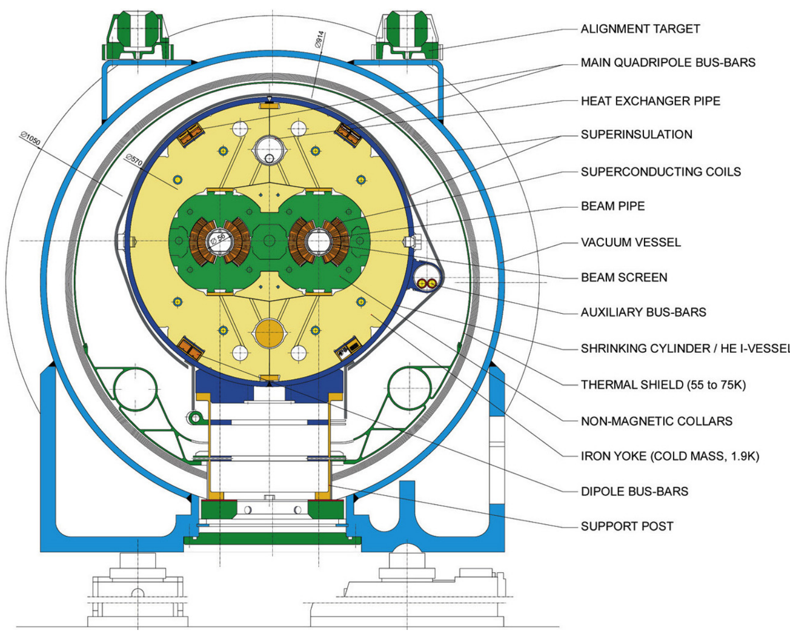

Figure 2.3: Cross-section of an LHC dipole magnet. Superconducting magnets are used to guide the beam around the accelerator ring. Image courtesy of Ref. [59].

2.2.3 Beam Structure

The distribution of protons within the beam follows a specific structure. Protons are distributed along the beam in clumps called "bunches," where each bunch comprises approximately 10^{11} protons. The LHC accelerator chain allows operators to create a wide variety of bunch patterns [56]. In typical Run 2 operation, each beam holds approximately 2500 bunches.

The beam profile of a single bunch is affected by many interactions, but is approximately a three-dimensional Gaussian [61]. The longitudinal width is approximately $\sigma_z = 40\,\mathrm{mm}$, while the transverse width is $\sigma_T = 0.37\,\mathrm{mm}$. Neighboring bunches are spaced approximately 7.5 m apart along the beam. The beam is continually monitored in the LHC control room by the LHC Beam Quality Monitor.

2.2.4 Collisions

At four locations around the LHC, the two beams are focused and made to intersect. A detector has been built at each of those four locations. ATLAS [62] and CMS [63] are the LHC's two general-purpose detectors. ALICE [64] is a specialized detector for studying the collisions of lead ions. Finally, LHCb [65] focuses on studying the physics of b-hadrons.

The bunches are timed so that they pass through one another at the center of each detector, called the "interaction point." The intersection of two bunches is called a "bunch crossing." The bunch crossing rate for Run 2 of the LHC was 40 MHz.

In any given bunch crossing, multiple inelastic pp collisions may occur. The average number of pp collisions per bunch crossing is called "pileup."

The rate of interactions produced by the LHC is measured with a value called "instantaneous luminosity," which is defined as the ratio of the production rate of a given process to the cross-section of that process,

$$\mathcal{L} = \frac{1}{\sigma}\frac{dN}{dt}, \tag{2.1}$$

and is given in units of inverse area per time. Physically, the luminosity can be understood as the geometric overlap of the two beams as they pass through one another in each bunch crossing. Thus, when multiplied with the cross-section of a certain process, the product is the event rate of that process. ATLAS luminosity measurements are performed using a Cherenkov detector called LUCID-2 [66, 67], which is calibrated by measuring the beam profile with a van der Meer scan [68].

A related quantity is the "integrated luminosity," which is the time integral of the instantaneous luminosity. During Run 2, the LHC delivered a total of $156\,\text{fb}^{-1}$, of which $139\,\text{fb}^{-1}$ was recorded by the ATLAS detector during which all detector subsystems were fully operational.

Most of the parton-level collisions at the LHC have a low center-of-mass energy [69]. These "soft" scattering processes, which involve parton collisions with low momentum transfer, produce a wide array of fairly ordinary particles and bound states. Only rarely does a collision occur with a very large center-of-mass energy. These "hard" interactions have enough energy to produce more exotic particles such as top quarks or $W^{\pm}$ bosons. Thus, to probe the physics of hard interactions, one must use a detector which can quickly and accurately identify and store those events, while simultaneously ignoring the majority of events, which are soft interactions.

2.3 The ATLAS Detector

The ATLAS detector [62] is a general-purpose particle detector located at the LHC. It is cylindrical, 25 m in diameter, 44 m in length, and weighs about 7000 tons. The detector covers nearly the entire 4π steradian solid angle around the interaction point, and is designed to physically contain as many of the particles produced in a collision event as possible.[1] The detector comprises three major subcomponents. The Inner Detector (ID), which exists inside a solenoidal magnetic field, provides high-granularity charged particle tracking. The Calorimetry system absorbs and measures the energy of particles passing through it. Finally, the Muon Spectrometer, situated inside a toroidal magnetic field, identifies and measures muons. A diagram of the full detector is shown in Figure 2.4. In the following sections, I will detail the technology and capabilities of each of the detector's components.

2.3.1 Detector Design Philosophy

The particles that ATLAS seeks to probe are often very short-lived. For example, the Higgs Boson, a Standard Model particle that ATLAS was

[1] An idealized version of such a detector is called a "hermetic 4π detector."

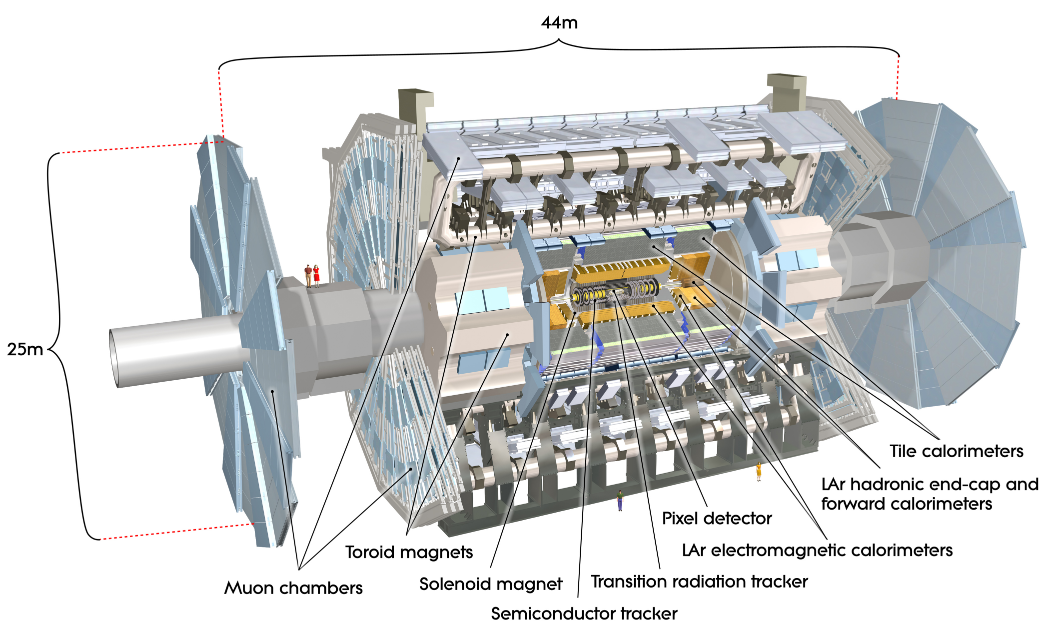

Figure 2.4: Cut-away diagram of the ATLAS detector with its various sub-detector components.

designed in part to discover, has a predicted lifetime of 10^{-22} s. Thus, there is no way to observe a Higgs boson directly. Instead, the strategy for studying these particles is to study their decay products. The overarching design philosophy of ATLAS is to measure nearly every long-lived particle that passes through some part of the detector. ATLAS can directly observe and measure electrons, muons, photons, and hadrons.

For charged particles, ATLAS is designed to identify the trajectory they take through the detector. The curvature of a particle's path in the magnetic field is used to identify the charge and momentum of the particle. Furthermore, the origins of the various trajectories in an event are grouped into common points called vertices. For both charged and neutral particles, ATLAS is designed to measure their energies. The software used to identify and measure these particles is described in Chapter 3.

2.3.2 Magnet System

A system of cryogenic magnets creates a strong and stable magnetic field throughout the detector [70]. The magnetic field it creates bends the trajectories of charged particles as they pass through the detector, allowing for the measurement of their momenta. The magnet system comprises three sections: a solenoidal magnet produces a 2 T magnetic field in the central region of the detector, a set of eight barrel toroidal magnets produce a 4 T (peak) magnetic field, and two endcap toroidal magnets produce a 4 T (peak) magnetic field. The subcomponents of the ATLAS magnet system are labeled

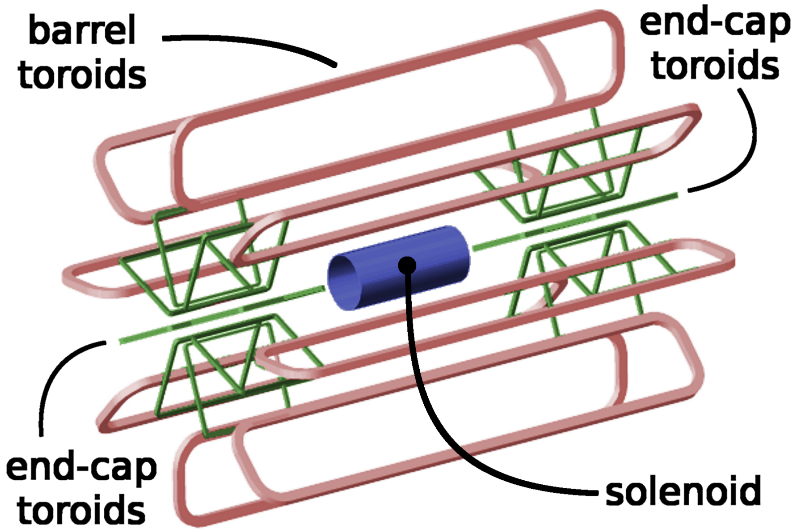

Figure 2.5: Diagram of the ATLAS magnet system. Image courtesy of Ref. [71].

in Figure 2.5.

2.3.3 Inner Detector

The component of ATLAS nearest to the interaction point is the inner detector (ID) [72, 73]. The ID is further subdivided into the Pixel Detector, the Semi-Conductor Tracker (SCT) and the Transition Radiation Tracker (TRT). A diagram of all of these components is shown in Figures 2.6 and 2.7. The ID is cylindrical, measuring 1 m in diameter and 6 m in length. Its primary purpose is to provide high-resolution measurements of the trajectories taken by charged particles as they move away from the interaction point and pass through the detector.

As a charged particle passes through the inner detector, it interacts

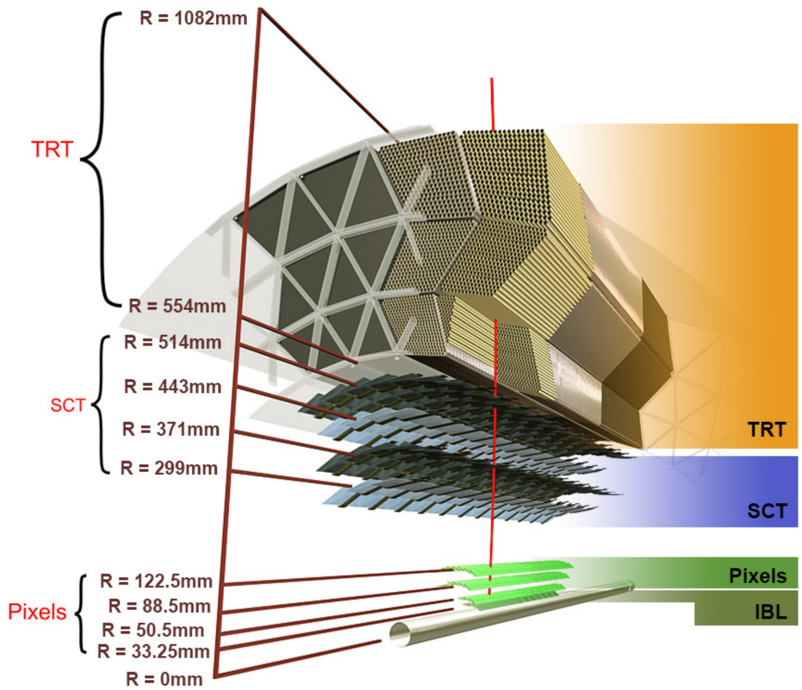

Figure 2.6: Schematic of the barrel components of the ATLAS inner detector. Image courtesy of Ref. [62].

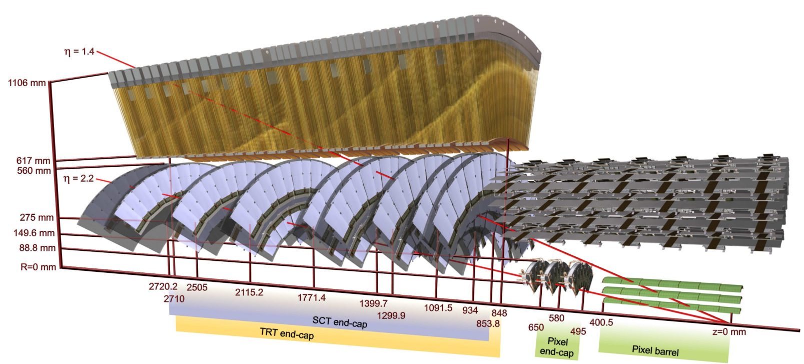

Figure 2.7: Schematic of the endcap components of the ATLAS inner detector. Image courtesy of Ref. [62].

with each of the many layers. A singular interaction of a charged particle with some active component of the ID is called a “hit.” ATLAS pattern-recognition software later combines related hits to form a “track,” which is a set of hits consistent with having originated from a single particle passing through the ID. The ID resolution is therefore important, since the exact shape of a track directly relates to the measured momentum of the particle. Additionally, the ID is designed to provide good resolution of the origin of each track. This ability is important for distinguishing certain types of events at the analysis stage. For example, a high-resolution ID is necessary to differentiate the production of prompt J/ψ mesons (originating from the primary vertex) from non-prompt J/ψ mesons (originating from a displaced vertex from the decay of a b-hadron) in data.

The pixel detector [74] is closest to the interaction point. It has four coaxial cylindrical layers. The innermost layer is also called the insertable B-layer (IBL). The primary purpose of this sub-detector is to provide high spatial resolution for vertex finding, track-vertex association, and track parameter measurements. Each pixel is made of oxygenated n-type silicon, and most pixels have an active area of $50 \times 400\,\mu\mathrm{m}^2$ (10% of the pixels are slightly larger). As a charged particle passes through a pixel, electron-hole pairs are created in the doped silicon. A bias voltage across the sensor separates these charges, generating a current. This current is then amplified and compared to a threshold value.

The SCT [75] surrounds the pixel detector, providing continued tracking of particles as they travel away from the interaction point. Like the pixel detector, it detects passing particles by their ionization of silicon. For the SCT, the active silicon is arranged in 285 μm thick "micro-strip" sensors. The shape of the micro-strips varies to accommodate the complex geometry of the ID layout.

The TRT [76] uses a different technology than the silicon-based Pixel and SCT detectors. It is composed of straw-shaped gas-filled drift tubes, which each have a diameter of 4 mm. A charged particle passing through one of these straws will ionize the Xe-based or Ar-based gas mixture. The ionized electrons can then be read out by the electronics system. The drift time is used to provide track resolution that is smaller than the straw diameter. The barrel layer has 73 layers of straws, and the endcap regions have 80. While the per-hit resolution is worse compared to the Pixel and SCT detectors, this sub-detector's performance is enhanced by the large average number of hits per particle. Additionally, the space between the straws is filled with polymer fibers. Charged particles passing through that medium may emit transition radiation. The probability of the radiation emission process is proportional to the particle's Lorentz factor $\gamma = E/m$. Thus, the presence or absence of this transition radiation is used to better distinguish electrons (which typically have a larger Lorentz factor) from muons and hadrons.

2.3.4 Calorimeters

The ATLAS calorimetry system [77–79] lies outside the ID and solenoid magnet. It comprises numerous components: the liquid argon electromagnetic calorimeter (EMCal) components measure energy deposits from electrons and photons, while the hadronic calorimeters (HCal) do the same for hadrons. Additionally, the Forward Calorimeter (FCal) measures energy deposits from both electromagnetic and hadronic sources in the region of the detector closest to the beam line. The arrangement of the various calorimeters within the ATLAS detector is shown in Figure 2.8. The calorimeters are constructed with alternating layers of absorbing material, which interacts with the high-energy particles to produce showers, and active material, which captures and measures the energy of those showers. The absorbing and active materials for each calorimeter are selected to best measure the targeted particles, while also minimizing construction costs.

The calorimeters have been designed to meet a number of design requirements. Each must be thick enough to absorb the full energy of the relevant particles. They must do this even for very energetic particles, as anything that "punches through" the calorimetry system contaminates the muon system. At the same time, the energy resolution of the calorimeters is important, even across many orders of magnitude of energy. For example, the resolution of the calorimeters directly impacts the calculation of the missing transverse energy, $E_{\mathrm{T}}^{\mathrm{miss}}$. This in turn directly affects the ability of the detector to measure the transverse momentum vector of a $W^{\pm}$ boson produced in a collision.

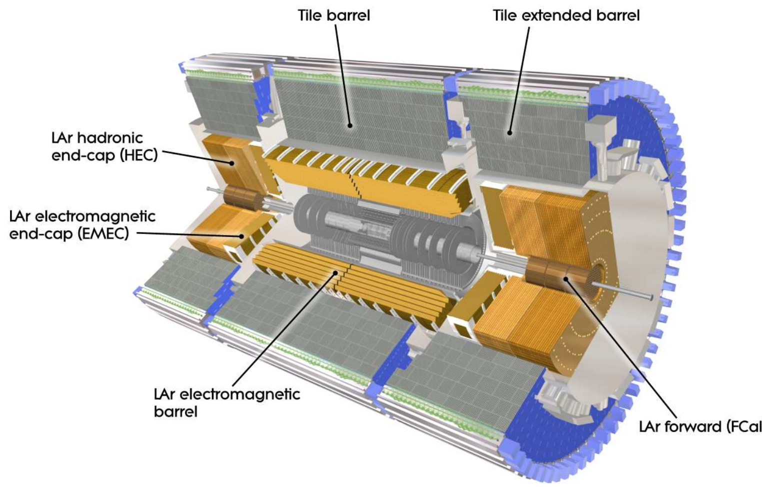

Figure 2.8: Cutaway diagram of the ATLAS calorimetry system. Image courtesy of Ref. [62].

Finally, the calorimeter segmentation is designed to help distinguish the energy deposits of electrons, photons, and hadrons. This feature is an important component of particle identification.

The electromagnetic calorimeters are constructed using lead as the absorber and liquid argon (LAr) as the active material. To ensure complete angular coverage of the calorimeter, the absorbers and electrodes of each cell are arranged in an accordion shape. This ensures that there are no gaps for electrons or photons to miss the absorbing material. The calorimeter is segmented into cells—shown in Figure 2.9—that allow for a three-dimensional measurement of energy deposits. There are three radial segments. The first layer is composed of thin strips, which is designed to improve angular resolution of energy deposits. The second layer has square cells, and captures most

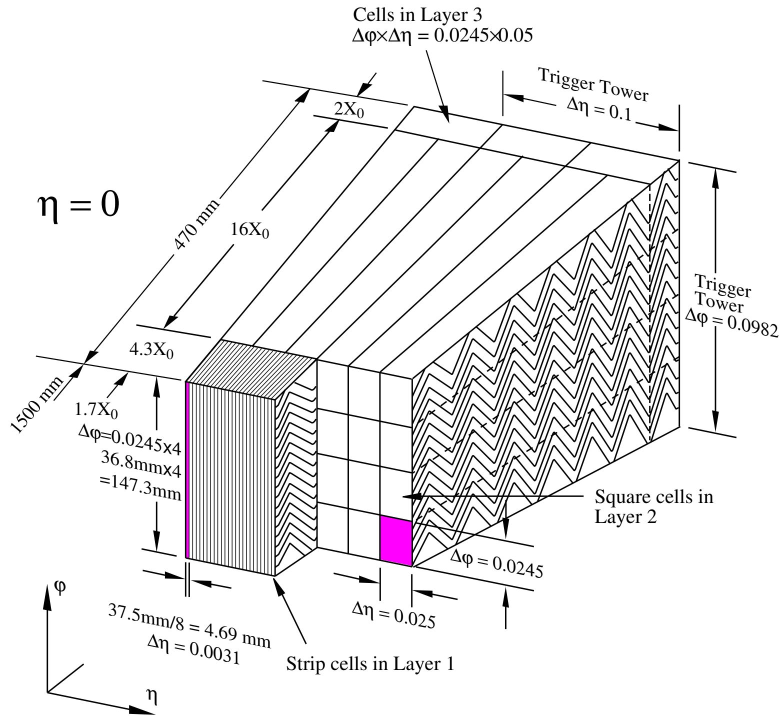

Figure 2.9: Cells for the ATLAS Liquid Argon Calorimeter. Image courtesy of Ref. [62].

of the energy of electromagnetic showers. The back layer has the coarsest segmentation, as it is used primarily to capture energy deposits from the tails of very energetic particles. This third segment is important for distinguishing very high-energy EM deposits from hadronic ones.

Before reaching the calorimeter, particles interact with a significant amount of material, such as the beam pipe, the ID, and the solenoid magnet. The material budget of the inner detector and electromagnetic calorimeter is shown in Figure 2.10. This introduces an uncertainty into the measurement of the energies of particles. To mitigate this, a liquid argon pre-sampler (with-

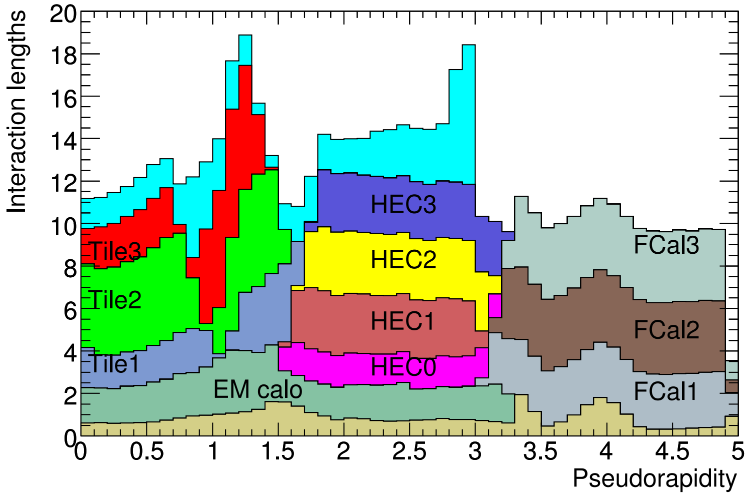

Figure 2.10: Cumulative amount of material, in units of interaction lengths, as a function of $|\eta|$. This includes the ID, all calorimeters, and all services. Image courtesy of Ref. [62].

out any absorbing material) is placed in front of the calorimeter to measure upstream electromagnetic energy losses. Additionally, in order to avoid the largest energy measurement uncertainties, electrons in the angular segment of the detector ($1.37 < |\eta| < 1.52$) that contains significant amounts of interacting material—commonly called the "crack" region—are typically excluded in the analysis stage.

The hadronic calorimeters, situated just outside the electromagnetic calorimeter, feature a variety of designs and active materials. The EMCal absorbs two thirds of the energy of a typical hadronic shower. Thus, the core purpose of the hadronic calorimetry system is to absorb and measure the remaining energy and protect the muon system from hadronic contamination.

The central region of the detector is occupied by the Tile Calorimeter, which uses steel as the absorber and scintillating tiles as the active medium. These materials are arranged into cells, as shown in Figure 2.11. The incoming hadron interacts with the steel and produces a shower of particles. Those particles then interact with the plastic tiles that—through a process called scintillation—convert the energy into flashes of light. The scintillation light is picked up by optical fibers and transferred to the readout electronics. The hadronic endcap calorimeters use a combination of flat copper plates as the active material and LAr as the absorber.

Finally, the forward calorimeter also uses a variety of active materials and LAr as the absorber. FCal has three modules, arranged radially. The first module uses copper as the active material in order to measure energy from electromagnetic particles. The outer two layers use tungsten, and target hadronic calorimetric activity. The electrodes are shaped into an array of rods and tubes, as shown in Figure 2.12. FCal is not used for precision energy measurements and resolution. However, due to its proximity to the beam line, it receives a high particle flux, so its presence is important for making the detector as hermetic as possible. Additionally, due to this large flux, it receives some of the highest radiation doses of the entire detector, so is designed to withstand a large radiation dose over its scheduled lifetime.

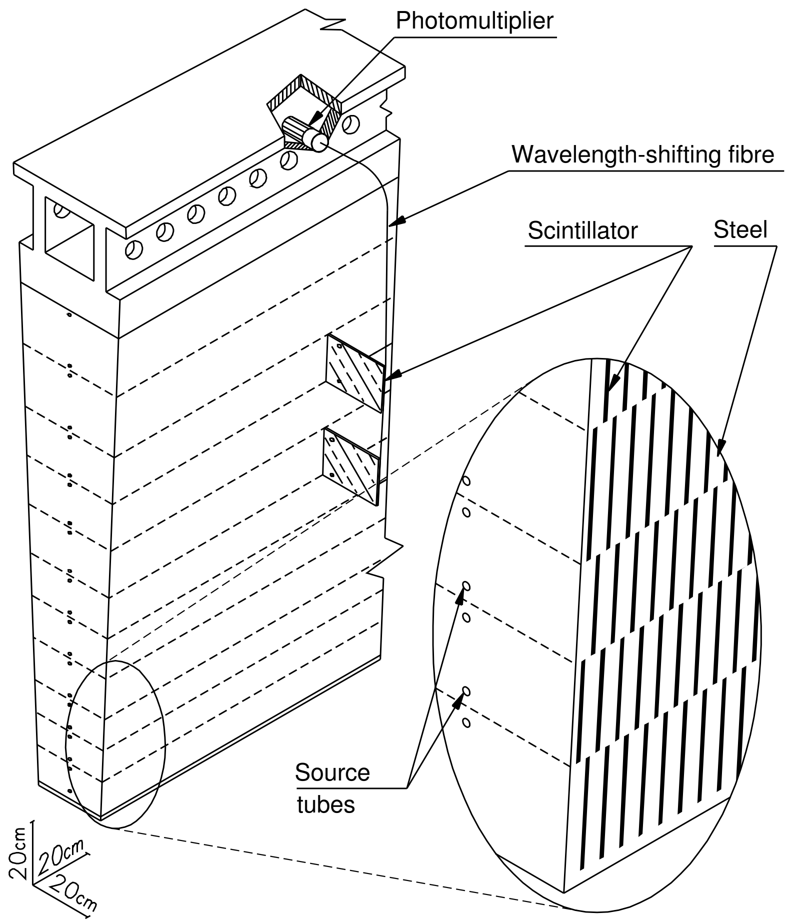

Figure 2.11: Schematic of one Tile Calorimeter module. Image courtesy of Ref. [62].

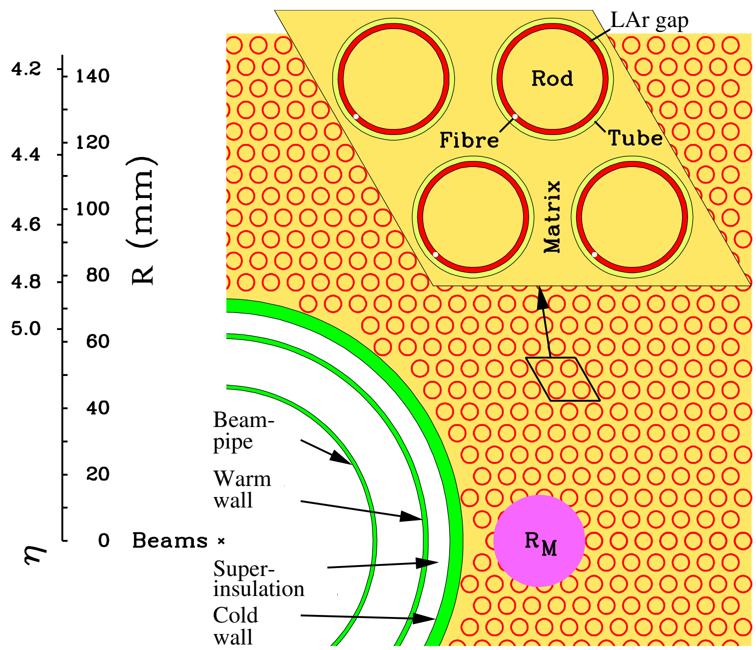

Figure 2.12: Diagram of layout of the absorbing and active material within the forward calorimeter, as viewed along the direction of the beam line. Image courtesy of Ref. [62].

2.3.5 Muon Spectrometer

The detector sub-system of ATLAS that is most distant from the interaction point is the Muon Spectrometer (MS), which is designed to observe, measure, and trigger on muons that pass through all other layers of the detector. The MS exists inside a toroidal magnetic field, and is used to greatly improve the identification of high-transverse-momentum muons produced in a collision. Additionally, the MS allows for very efficient reconstruction of $J/\psi \to \mu^+\mu^-$ decays. (The muon channel significantly outperforms the $J/\psi \to e^+e^-$ channel.) The precision track measurement of the muons uses two technologies: Monitored Drift Tubes (MDT) and Cathode Strip Chambers (CSC). In order to trigger on high-momentum muons, a complementary fast muon detection system uses Resistive Plate Chambers (RPC) and Thin Gap Chambers (TGC) to rapidly detect the presence of high-momentum muons. These various components are labeled on the diagram of the MS in Figure 2.13.

The active elements of MDTs are pressurized drift tubes filled with a gaseous mixture of argon and carbon dioxide. A passing muon ionizes the gas, and the ionized electrons are collected by a central anode wire, which is connected to the electronic readout. The arrival time of the signal is used to measure the drift radius of the ionized electrons from the ionization point to the anode, providing high position resolution information. The MDT tubes are arranged in layers of three or four tubes, called "multi-layers". Two multi-layers are then combined on either side of a metal support structure to form a single "chamber." A diagram of a MDT chamber is shown in Figure 2.14.

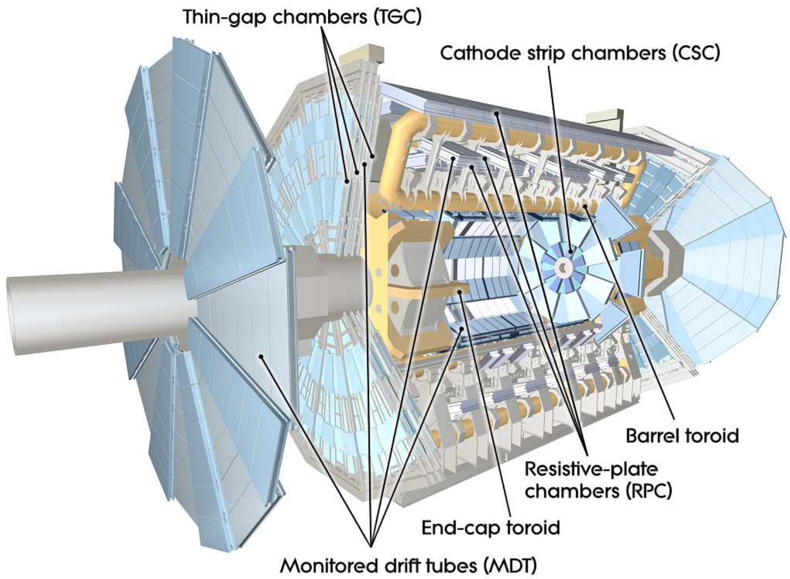

Figure 2.13: Diagram of the ATLAS Muon Spectrometer, with the various components labelled. Image courtesy of Ref. [62].

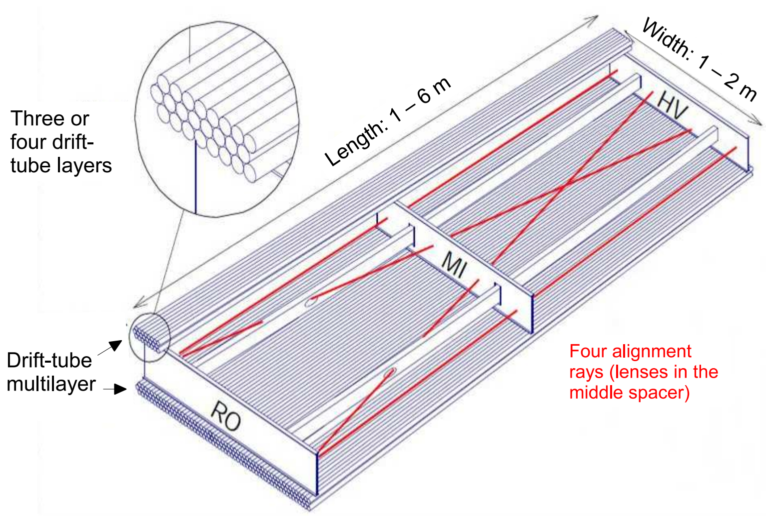

Figure 2.14: Diagram of one MDT chamber. Drift tubes are stacked a few layers deep to form a multi-layer. Two multi-layers are attached to a support structure to form one chamber. Image courtesy of Ref. [62].

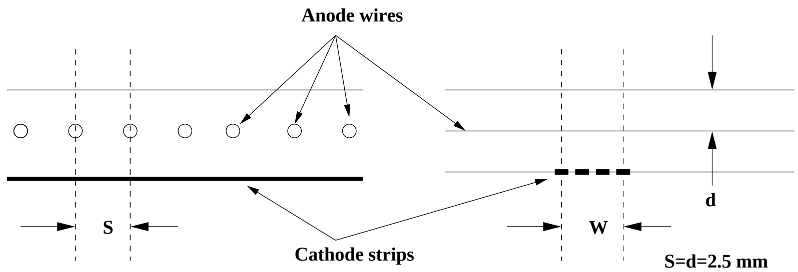

Figure 2.15: Layout of the anode wires and cathode strips in one CSC cell. Left: view looking down the direction of the wires (towards the beam pipe). Right: view looking perpendicular to the direction of the wires and parallel to the cathode strips.

The performance of MDTs degrades at high hit rates. Therefore, CSCs are instead used for precision muon measurements in the regions of the detector with higher muon fluxes. Each CSC is a thin chamber filled with a gaseous Ar-CO_2 mixture. Inside the chamber, there is a sequence of anode wires running perpendicular to a sequence of cathode strips, as shown in Figure 2.15. The distribution of the charge deposits on neighboring strips is combined to provide high-resolution position tracking of muons.

RPCs are used to provide fast identification and measurement of muons with comparatively low resolution. Each RPC is constructed with two parallel plates separated by 2 mm and is filled with a gaseous mixture of $C_2H_2F_4$, Iso-C_4H_{10}, and SF_6. The ionized electrons from a passing high-energy muon are read out on metallic strips. Two layers are combined with perpendicular strips (to provide a two-dimensional hit localization) to form one station. One or two RPC stations are attached to each MDT chamber in the barrel region of the spectrometer system. In the endcap detectors, TGCs perform the same role.

TGCs are multi-wire proportional chamber detectors filled with carbon dioxide and n-pentane, and provide fast readout of signals from high-momentum muons for the trigger system.

2.3.6 Trigger, Readout, and Data Acquisition

A multi-stage trigger system [80, 81] is used to select events for storage based the type of collision that occurred. Generally, processes with large cross-sections are well-understood from decades of prior experiments, so one generally does not want to record those events. Instead, the trigger system attempts to identify events to record which are physically interesting. Each “trigger” is a set of conditions that, if met, initiates a full readout of the data collected by all detector subsystems. Unprescaled triggers fire anytime the conditions are met. Prescaled triggers, which typically have less stringent requirements and target more common processes, have an associated “prescale” factor, which is a probability that an event should be stored when the prescaled trigger’s conditions are met. Before data-taking begins, a “trigger menu” is created based on the planned LHC collision environment. The menu is carefully adjusted so that the sum of the rate of all triggers is equal to the maximum readout capabilities of the data acquisition (DAQ) system, and minimal changes are made during a given year of data collection.

The trigger process occurs in two stages. First, the Level-1 (L1) trigger, which is hardware-based and uses fast electronics, performs a rapid measurement of each event. It uses low-granularity information from the calorimeters

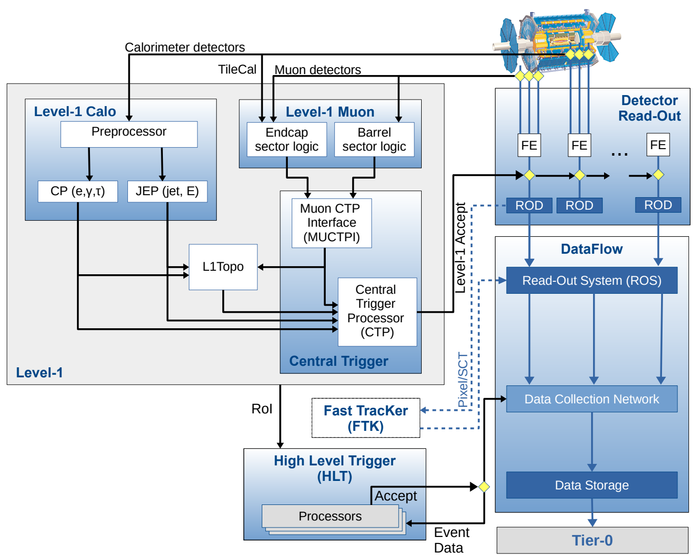

Figure 2.16: The ATLAS Trigger system showing the trigger decision paths and data flow. A low-level trigger identifies events that may have included a hard process. Those events and their ROIs are passed to higher-level triggers. Events passing an HLT are read out and stored.

and muon spectrometer to decide whether a hard process occurred. If an L1 trigger passes, it identifies regions of interest (ROI) which are forwarded onto the next stage. The L1 trigger rate is approximately 100 kHz. Next, the high-level trigger (HLT) [82] uses the ROI data from the L1 trigger to perform a full-granularity partial readout of the detector. This stage is software-based and fires at an average rate of 1 kHz. Events which pass the HLT are fully read-out and stored permanently for analysis. The complete trigger process is shown diagrammatically in Figure 2.16.

Events may be targeted by a specific trigger based on the presence of a high-p_{T} charged lepton, significant calorimetric activity, or a large amount of missing transverse energy. Additionally, some triggers search for a combination of these items. Each trigger is built to identify important signatures for one or more of the numerous ATLAS analyses.

For the analysis presented in this dissertation, associated $J/\psi + W^{\pm}$ and inclusive $W^{\pm}$ events are identified by using a trigger that requires at least one isolated, high-p_{T} lepton (from a leptonic $W^{\pm}$ decay). As an example, suppose a high p_{T} muon passes through the barrel region of the MS. This muon is first identified by the L1 muon trigger by searching for coincident hits in three concentric RPC layers. From these hits, a low-resolution momentum measurement is made. If it passes the p_{T} threshold, that area is designated as an ROI, and the event is passed to the HLT system. There, the barrel muon is reconstructed using the precision tracking information from the ID and CSCs. At this stage, isolation criteria can be applied to reject muons from b-hadron decays. If the reconstructed muon passes the HLT muon p_{T} threshold, the entire event is read out and stored.

Chapter 3

Event Reconstruction

The data collected from the sub-detectors described in the previous chapter are electronic signals that correspond to the interaction of particles with the active material of the detector. These raw electronic signals either represent the location of a charged particle passing through a piece of the ID or MS, or an energy deposit from a particle into a calorimeter cell.

The initial stage of reconstruction performs two actions: sequences of hits in the ID or MS are combined into charged particle "tracks" and energy deposits in nearby calorimeter cells are combined into calorimeter "clusters." Next, the track and cluster information is combined across the various sub-detectors to reconstruct candidate particles. Reconstruction can directly identify electrons, muons, photons, and long-lived hadrons in recorded events. Various object definitions and identification methods are used to identify these objects. The presence particles with very short lifetimes in an event can be determined at the analysis stage using combinations of the observed particles and statistical inference. Additionally, the presence of particles which travel through the detector but do not interact with it—e.g. neutrinos—can be inferred from the rest of the observed event.

In this section, I will explain the algorithms, procedures, and definitions that are used to identify and measure particles in the raw detector data. Collectively, this process is called “reconstruction.”

3.1 Tracking

The ATLAS track reconstruction algorithm [83] seeks to identify any charged particle tracks in the ID which have $p_{\mathrm{T}} > 0.5\,\mathrm{GeV}$ and $|\eta| < 2.5$, and to associate each track to a production vertex. The tracking algorithm takes the raw data from the ID and converts it into a set of parameterized curved paths of candidate charged particles. The process proceeds in three steps: pre-processing, track-finding, and post-processing.

In the pre-processing step, raw values of charge deposits and drift radii are converted into space-point measurements of charged particle hits. As a charged particle passes the pixel and SCT detectors, it may leave charge deposits on multiple pixels, called a cluster. The relative magnitudes of these charge deposits on nearby pixels are combined to produce a single space-point measurement of a charged particle. Similarly, the charge deposits from SCT modules are combined into singular spatial measurements. The raw drift time measurements of the TRT tubes are likewise converted into charged particle location points. The output of this step is a set of “hits,” which are points where a charged particle interacted with some layer of the detector.

In the track-finding step, multiple hits are combined to form a “track,” which is a subset of the hits that are consistent with having originated from a single particle passing continuously through multiple layers of the detector. This step begins with a track seed, which is a set of nearby hits in the innermost pixel layers. Next, the seeds are extended outward to any hits in the outer SCT layers. Tracks which have a poor fit quality are removed at this stage. Finally, tracks are extended into the full ID with hit information from the TRT. Once the full track is constructed, the tracks parameters are re-determined using the information from all layers of the detector. Tracks with parameters that deviate significantly from their initial values are labeled as outliers.

Finally, in the post-processing step, a set of common track origins is constructed, and each track is associated to one of these "primary vertices." In each event, the vertex with the largest $\sum p_{\mathrm{T}}^2$ of constituent tracks is selected as the "event primary vertex."

Following these three steps, the final track parameters are computed using all available information. Each track is modeled as a helical trajectory through the ID. The origin and shape of this trajectory is determined by 5 track parameters: d_0 and z_0 are the transverse and longitudinal impact parameters at the point of closest approach to the beam line, ϕ and θ are the azimuthal and polar angles of the helix, and q/p is the charge to momentum ratio of the track. In later steps of reconstruction, the tracks are used to identify electrons and muons.

3.2 Calorimeter Clusters

Particles deposit their energy in the calorimeter in the vicinity of their path through the absorbing material. The observed energy deposits are organized into "clusters," which are localized energy deposits in nearby cells [84]. Clusters are three-dimensional in both the EM and Hadronic calorimeters. A cluster's shape, magnitude, and proximity to an ID track are all used in later stages of reconstruction to identify specific particles.

3.3 Electrons

The electron reconstruction algorithm [85, 86] combines tracks and calorimeter clusters to form electron candidates. Further selections are applied to these candidates to reduce backgrounds while maintaining uniform high efficiency identification across the full acceptance range of the detector. First, a cluster of energy is identified in the EM calorimeter. Then, the radial position of the cluster is compared to the set of tracks in the inner detector. If the positions of the cluster and a track coincide, the two are matched to form an electron candidate object. Each object is then re-calibrated using the combined information of the associated track and cluster.

This initial set of electron candidates contains photon and hadron backgrounds. Further electron identification selections are applied to the candidates in order to improve the purity of the selected objects. Thirteen different variables are used for discrimination. The variables include properties of the track, the shape of the electromagnetic shower in the calorimeter, and the spa-

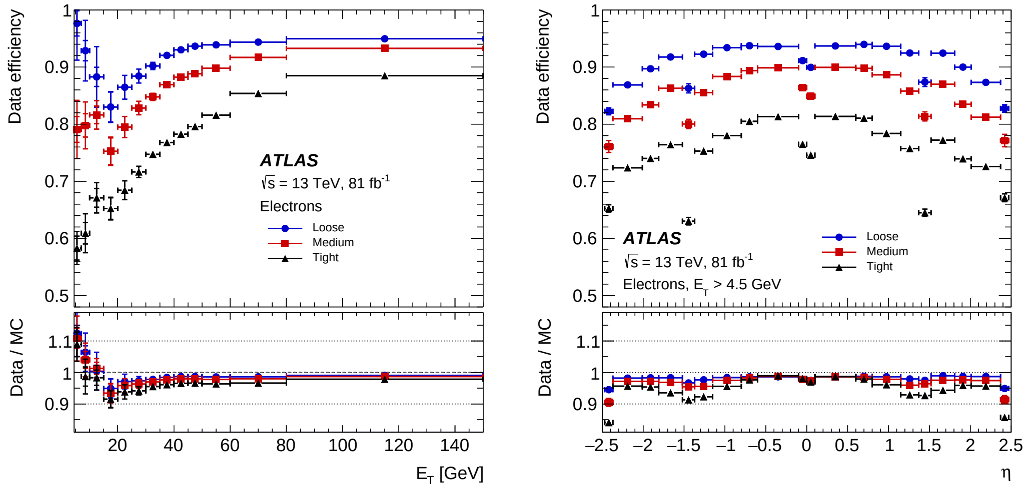

Figure 3.1: Electron identification efficiency in Run 2 data as a function of transverse energy (left) and pseudo-rapidity (right). The "Tight" working point was used the analysis presented here. Images courtesy of Ref. [86].

tial overlap of the track and cluster. These variables are combined to calculate an overall likelihood discriminant. Three electron identification working points are created by placing various cuts on this discriminant (and various other selections) to meet some predefined goals of signal efficiency and background rejection.

In the analysis presented in this dissertation, the Tight identification working point was used. For typical electroweak processes, the average signal efficiency is approximately 80%. The electron identification efficiency as a function of η and E_{T} is shown in Figure 3.1. The presence of background processes is significantly reduced using this method, and the remaining background contamination is estimated at the analysis stage.

3.4 Muons

The ATLAS muon reconstruction [87] algorithm uses similar methods, combining tracks in the inner detector with energy deposits in the EM calorimeters. Additionally, muons interact with the MS, which allows for extremely precise and efficient identification and measurement of these particles across a wide range of transverse momentum values. The ability to accurately reconstruct muons with $p_{\mathrm{T}} > 3\,\mathrm{GeV}$ is extremely important for the study of J/ψ mesons (via the $J/\psi \to \mu^+\mu^-$ decay channel.)

In an initial stage—following a similar process to ID tracking—MS hits are identified and tracks are formed from those hits. Then, the MS tracks are matched to ID tracks and calorimeter clusters to form muon candidates. The combination of information from many sub-detectors allows for near 100% identification efficiency for typical electroweak processes within the acceptance range of the detector. The muon identification efficiency as a function of η and p_{T} is shown in Figure 3.2.

The muon candidates undergo a set of selections based on the number of hits in each sub-detector, the track fit properties, and the compatibility of the individual measurements from the various sub-detectors. Several working points have been developed to meet the many disparate requirements of varied physics measurements being performed using the ATLAS dataset. The needs of high identification efficiency, good background rejection, high momentum resolution, and the ability to distinguish muons from electroweak and hadronic (especially $\pi^{\pm}$ and $K^{\pm}$) decays.

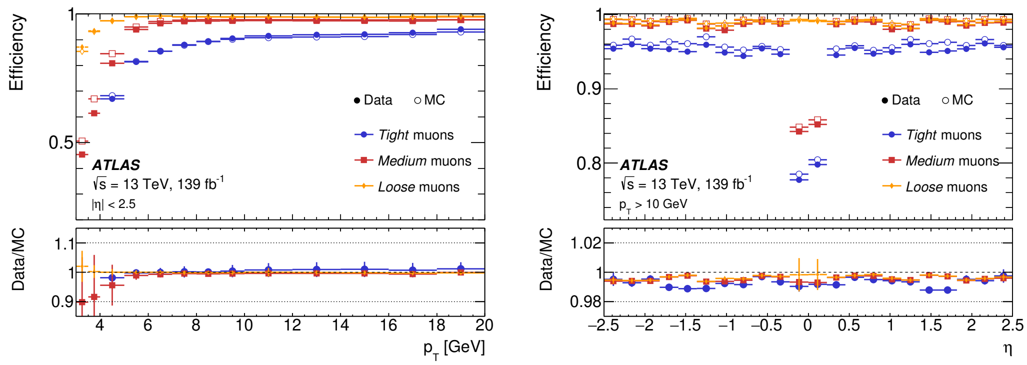

Figure 3.2: Muon identification efficiency in Run 2 data as a function of transverse momentum (left) and pseudo-rapidity (right). The "Tight" working point was used in the analysis presented here. Images courtesy of Ref. [87].

3.4.1 Low-p_T Muons

To better reconstruct muons with low transverse momentum, such as those from a $J/\psi \to \mu^+\mu^-$ decay, a working point was developed to specifically identify muons with $p_T \in (3\,\mathrm{GeV}, 18\,\mathrm{GeV})$. These are less likely to produce full tracks across all layers of the MS, leading to low reconstruction efficiencies using the standard working points. Muons typically lose about 3 GeV of energy in the calorimeters, so reconstruction efficiency below that value is greatly diminished due to the lack of any MS hits.

Several variables are used to train a gradient boosted decision tree (BDT) to best identify muons and reject backgrounds. The BDT is trained with simulated $t\bar{t}$ events, and each variable provided to the BDT is validated with comparison to real data. The muon identification efficiency of the Low-p_T working point is shown in Figure 3.3.

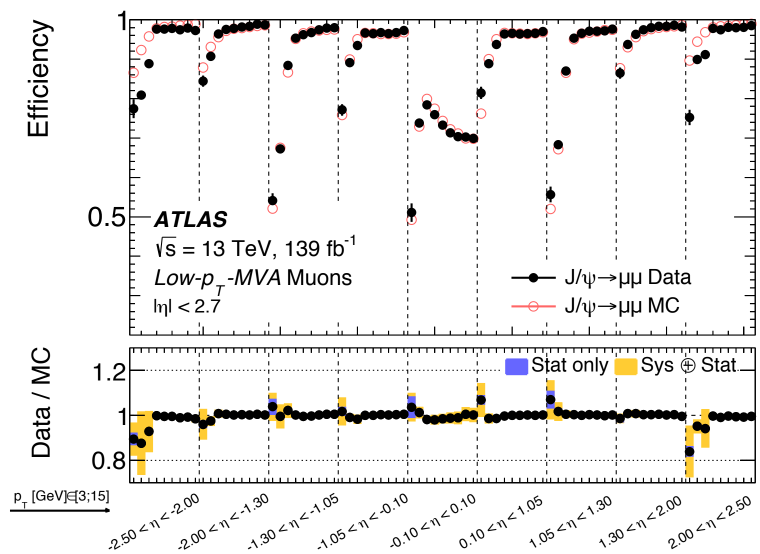

Figure 3.3: Muon identification efficiency for the Low-Pt reconstruction algorithm in Run 2 data as a function of transverse momentum and pseudorapidity. Image courtesy of Ref. [87].

3.5 Jets

Shortly after quarks and gluons are produced, they undergo hadronization and showering, wherein they repeatedly split apart and form hadrons. Due to the nature of their production, the directions of the product hadrons from one initial quark are all strongly correlated. Thus, the presence of a quark or gluon in a hard scattering event is observed in the detector as group of energy deposits. The four-momenta of the constituent hadrons are not individually measured. Instead, they are combined into a single four-momentum of a composite "jet" object.

Even if jets are not actively used in a particular measurement, such as in the measurement of the associated prompt $J/\psi + W^{\pm}$ production cross-section, it is important to accurately measure their transverse energy, since the total transverse energy of all particles in the event is used to infer the existence of particles which pass through the detector unobserved, such as the neutrino from a leptonic $W^{\pm}$ decay.

3.6 Missing Transverse Energy

A number of known and hypothetical particles pass through the detector unobserved. An example within the Standard Model is neutrinos, which are light, neutral leptons that interact extremely weakly with any other forms of matter. Additionally, some BSM models predict LHC production of dark matter or supersymmetric particles that similarly do not interact with the baryonic matter of the detector. Before a given *pp* collision, the system is known to have a negligible transverse momentum component. Therefore, the existence of non-interacting particles in an event can be inferred when the transverse momenta of all observed outgoing particles in an event do not sum to zero. The remainder of this vector sum, the "missing transverse energy," [88] is generally defined as

$$\mathbf{E}_{\mathrm{T}}^{\mathrm{miss}} = -\sum_{i} \mathbf{E}_{\mathrm{T}}^{i}, \tag{3.1}$$

where $\mathbf{E}_{\mathrm{T}}^{i}$ is the transverse energy of a single reconstructed object, and the sum is taken over all objects in the event.

For example, suppose a certain *pp* collision produces only a $W^{\pm}$ boson, which then decays to a muon and a neutrino. The muon can be directly observed by the detector and the transverse component of the neutrino four-momentum can be measured by the fact that the momentum of the muon is not balanced by another observed particle in the transverse plane. Note that the longitudinal component of the neutrino is not measurable, since the longitudinal momentum component of the input quarks or gluons is not known.

The $E_{\mathrm{T}}^{\mathrm{miss}}$ is calculated separately for muons, electrons, and jets. Additionally, an attempt is made to calculate transverse energy which is not included in one of those four terms. Those contributions are combined into a "Soft MET" term,

$$E_{\mathrm{T}}^{\mathrm{miss}} = -E_{\mathrm{T}}^{\mu} - E_{\mathrm{T}}^{e} - E_{\mathrm{T}}^{\mathrm{jet}} - E_{\mathrm{T}}^{\mathrm{soft}}. \tag{3.2}$$

Any energy already included in one term is excluded from being used in the calculation of any other term.

3.6.1 Soft $E_{\mathrm{T}}^{\mathrm{miss}}$

The soft term may be calculated using either calorimeter or track information. The calo-based soft term comprises energy deposits in the calorimeter that are not already associated with some other object. The track-based soft term is constructed from all primary-vertex-associated tracks not being used for another object.

The calo-based soft term includes contributions from neutral and forward particles. (The calorimetry system, including the FCal, provides good coverage for $|\eta| < 4.9$.) However, the resolution of this method is relatively

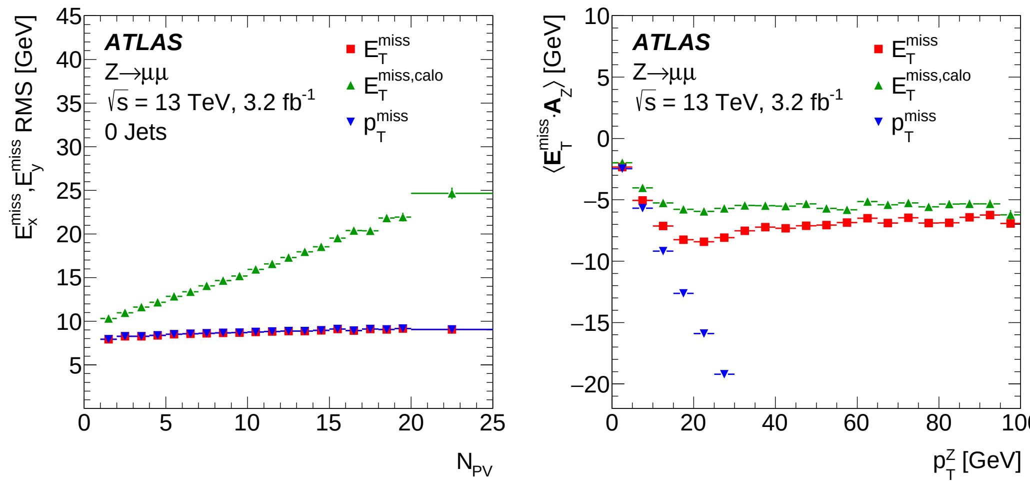

Figure 3.4: Performance of the $E_{\mathrm{T}}^{\mathrm{miss}}$ calculation in simulated $Z \to \mu\mu$ events. The calo-based soft $E_{\mathrm{T}}^{\mathrm{miss}}$ term degrades the overall $E_{\mathrm{T}}^{\mathrm{miss}}$ resolution, especially in high pileup (large N_{PV}) conditions (left). The hadronic recoil activity is not accurately incorporated, leading to a bias of a few GeV (right). Images courtesy of Ref. [88].

poor and degrades significantly in high-pileup conditions.

On the other hand, the track-based soft term utilizes high-precision measurements from the ID. This method has much better resolution, and is relatively stable under high-pileup environments. However, many particles are outside the acceptance of the tracker: neutral particles and forward particles with $|\eta| > 2.5$ are not included in the track-based soft term. Due to the improved resolution, even in high-pileup environments, this method is the nominal choice of soft $E_{\mathrm{T}}^{\mathrm{miss}}$ for most analyses.

The $E_{\mathrm{T}}^{\mathrm{miss}}$ is used in many physics analyses to separate signal and background events in data, so it is critical to accurately and precisely reconstruct this quantity. However, the soft $E_{\mathrm{T}}^{\mathrm{miss}}$ component is fundamentally limited by the information provided by the various sub-detectors. The left-hand side of Figure 3.4 shows the resolutions of total $E_{\mathrm{T}}^{\mathrm{miss}}$ for Z events in data based on different choices of soft $E_{\mathrm{T}}^{\mathrm{miss}}$. This shows that the track-based version significantly outperforms the calo-based option in terms of resolution. On the right-hand side of Figure 3.4, the $E_{\mathrm{T}}^{\mathrm{miss}}$ projection onto the Z flight direction is shown. (The bias should be 0 for Z events.) Much of the hadronic recoil of the event is not included in the soft term, leading to a bias between $2-9\,\mathrm{GeV}$. The $E_{\mathrm{T}}^{\mathrm{miss}}$ with a calo-based soft term performs slightly better, but the bias does remain. A bias under $10\,\mathrm{GeV}$ will often not significantly affect an analysis that utilizes $|E_{\mathrm{T}}^{\mathrm{miss}}|$. However, in the case of $J/\psi+W^{\pm}$, the angular separation of the two particles is important for separating different production modes. A small bias in the $E_{\mathrm{T}}^{\mathrm{miss}}$, for relatively soft $W^{\pm}$ bosons, can significantly change the reconstructed azimuthal direction of the $W^{\pm}$.

3.7 Overlap Removal

After object reconstruction, an overlap removal (OR) algorithm is applied to avoid ambiguities. For Run 2, the OR procedure has been standardized across numerous analyses. For example, one object may be reconstructed by multiple object identification algorithms. Additionally, this process can help remove some backgrounds in the measurement of prompt $J/\psi+W^{\pm}$ production (especially fake leptons, which often overlap jets). Many OR criteria use the radial separation between the two objects, $\Delta R = \sqrt{\Delta\varphi^2 + \Delta\eta^2}$. The following removals are performed in the specified order.

- If two electrons share an ID track, the lower p_{T} one is removed.
- If an electron and muon share an ID track, the electron is removed.
- If $\Delta R\,(e^{\pm}, j) < 0.2$, the jet is removed.
- If a jet has fewer than 3 tracks and $\Delta R\,(\mu^{\pm}, j) < 0.2$, the jet is removed.
- If $\Delta R\,(j, \mu^{\pm}) < 0.4$, the muon is removed.

Chapter 4

Monte Carlo Generation and Simulation

Most analyses of particle physics data rely significantly on comparisons to simulated data. In this chapter, I will discuss how generated events are produced, the detector response is simulated, and what samples were created for this measurement.

4.1 Matrix Element Generators

As discussed in Chapter 1, QFT can be used to predict the probability of a certain particle interaction process for a specific Lagrangian, such as that of the Standard Model. A certain matrix element is expanded in terms of a coupling parameter to produce a series of interactions, where each term can be represented with a Feynman diagram. If the coupling parameter is small, the total probability can be accurately computed using only the first few terms in this expansion. In practice, matrix elements are calculated numerically using Matrix Element Generators. Some commonly-used generators are `MadGraph` [89] and `PowhegBox` [90–92].

To produce simulated events, one provides a generator two sets of information. First, the user provides a set of parameters—particle masses, coupling constants, parton density functions, etc.—which are used during the matrix element calculation. For well-understood processes, these parameters are chosen based on a combination of decades of experimental results. Additionally, the user specifies the desired input and output particles. To improve computational efficiency during the later stages of MC sample generation, one typically also places requirements on the direction and momenta of the output particles. As a complete example, one could request the generator to simulate a collision of two protons that produces a J/ψ, where each incoming proton has an energy of 6.5 TeV and the output J/ψ has a transverse momentum of at least 8 GeV and $|y| < 2.1$. By placing these requirements on the event, it is comparable to an event that could be produced in an LHC collision and reconstructed by the ATLAS detector.

The output of the generator is a dataset of simulated hard scatter events. For the dataset as a whole, the generator predicts a value for the cross-section. Additionally, for each event, it includes a list of input, intermediary, and output particles, as well as an event weight. Finally, for each of the generated particles, it generates a four-momentum vector.

A standardized text-based human-readable (and machine-readable) Les Houche Event (LHE) [93, 94] format exists and is normally used to store the generator outputs. This standard format allows for seamless communication between different generators. The predicted cross-section from the generator is calculated to a fixed order in perturbation theory: leading order (LO), next-to-leading order (NLO), next-to-next-to-leading order (NNLO), etc.

4.2 General-purpose Event Generators

The simulation of a (for example, $2 \rightarrow 2$) hard scattering event is only one component of a full Monte Carlo event simulation. To reasonably compare a simulated event to a real LHC collision, one must use a general-purpose Monte Carlo (GPMC) event generator. Some commonly-used examples are `Pythia` [95, 96], `Herwig` [97–99], and `Sherpa` [100]. GPMCs can model a hard scatter, an underlying event (non-participating spectator quarks and any collisions besides the hard scatter), and QCD phenomena like hadronization and showering. A visualization of such an event is shown in Figure 4.1. Often, a hard scatter is calculated using a dedicated matrix element generator—which may provide more accurate or efficient calculations—stored in the LHE format, and then passed to a GPMC generator, which executes all other functions.

Most of the internal models in a GPMC are not derived from first principles, but instead use QCD-inspired heuristic models and parameterized non-perturbative QCD calculations, which are very difficult to perform analytically. These models and their parameters have been finely tuned to match decades of past experimental results. Still, one can not expect any generator to accurately predict every feature of a collision event. For example, the generator may not accurately reproduce the N_{jet} spectrum or the hadronic p_{T} spectrum observed in data. Thus, it is critical to validate simulated events with data-driven methods.

In order to model the underlying event, most GPMC generators simulate multi-parton interactions (MPI). The `Pythia8` generator extends this

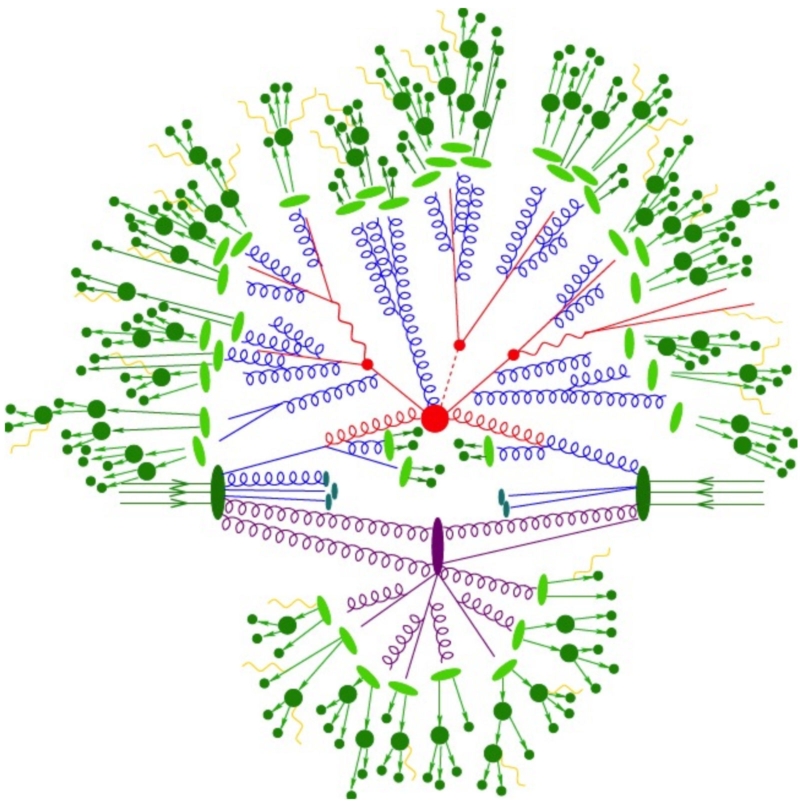

Figure 4.1: A visualization of an event generated using `Sherpa`. This event includes proton fragmentation, a hard collision, hadron formation, and parton showering. Image courtesy of Ref. [100].

feature by allowing the user to specify a specific second hard parton-level scattering. For this analysis, `Pythia 8` was used to simulate double-parton scattering $J/\psi + W^{\pm}$ events.

4.3 Detector Response Simulation

The events recorded in data are subject to effects from the reconstruction process described in Chapter 3. Thus, in order to reasonably compare the data and simulation, it is imperative to replicate this process for the simulated events. The full particle-level event is passed through a sophisticated simulation of the detector [101]. Each long-lived particle in the event is propagated through the detector, and the interactions of each particle with the detector's material are simulated using `Geant` [102]. For example, for a high-energy charged hadron, the software will simulate its interactions with the silicon and metal of the ID, the iron of the solenoidal magnet, the liquid argon of the EM calorimeter, and layers of the hadronic calorimeter. The effects of detector wiring and services, hit recognition efficiency, and gaps in the detector coverage are all included in the simulation.

The models used for simulation are validated and improved using data-driven studies [103]. ATLAS collision data have been used to study the location of the material in the ID, which reduced the overall uncertainty on charged-particle reconstruction efficiency.

The full simulation of the detector is extremely computationally intensive, and uses a significant fraction of the available ATLAS computing resources. To remedy this, many simulation samples use a parameterized model of the detector response in the calorimeters. The software which performs this calculation is called ATLAS Fast-Simulation II (AFII) [104].

At this stage, the detector response can be read out from the simulated detector in the same manner as real data is read out from the real detector. This allows for the inclusion of trigger efficiency, reconstruction efficiency, and detector resolution effects. The event information provided directly by Monte Carlo generators—before any detector effects are applied—is called “truth” or “generator-level” information. The properties of the event after detector effects have been simulated are called “reconstruction” information.

4.4 Monte Carlo Simulation Samples

The analysis presented in this dissertation utilizes a number of MC samples of inclusive $W^{\pm}$ production, associated $J/\psi + W^{\pm}$ production, and other processes that mimic the experimental signatures of those two. These samples were used to estimate background contributions and distinguish different production modes in data.

The parameters of `Pythia8` have been tuned to ATLAS data with the `A14` tune [105]. Either the `CTEQ6L1` [106] or the `NNPDF23LO` [107] parton distribution function set was used for each sample. The simulation also accounts for the effects of pileup. Events are first generated based on an expected pileup profile. After data-taking is completed, the simulated events are re-weighted according to the observed pileup conditions.

Table 4.1: List of Monte Carlo samples used for studies of inclusive W production.

Description	Generator	$\sigma \times$ BR [nb]	Order
$(W^{\pm} \rightarrow l^{\pm}\nu)$ + jets	Powheg + Pythia	60.24	NLO
$(Z \rightarrow l^{+}l^{-})$ + jets	Powheg + Pythia	5.85	NLO
$t\bar{t}$ ($l^{\pm}$ filter)	Powheg + Pythia	0.45	NNLO
t ($l^{\pm}$ filter)	Powheg + Pythia	0.15	NLO
VV ($l^{\pm}$ filter)	Sherpa	0.10	LO/NLO

4.4.1 Inclusive $W^{\pm}$ Samples

The inclusive $W^{\pm}$ signal and background samples were centrally produced by a number of analysis groups which study electroweak and BSM physics. The generation was performed at NLO. A summary of the samples is presented in Table 4.1.

The vector boson, top pair, and single top samples were all produced with `Powheg-Box` using the `CTEQ6L1` PDFs. Hadronization and showering was performed by `Pythia8` with the `A14` tune. The di-boson samples were produced, hadronized, and showered using `Sherpa 2.2.2` generator with the `NNPDF3.0` PDFs.

4.4.2 QCD Multi-jet Sample

A $b\bar{b}$ MC sample is used to estimate the QCD multi-jet background in inclusive and associated events. The $b\bar{b}$ sample is produced with `Pythia8` using the `CTEQ6L1` PDFs and `A14` tune. The events are filtered at generator level to contain a decay to $J/\psi \rightarrow \mu^{+}\mu^{-}$. This sample's primary purpose is to

Table 4.2: List of Monte Carlo samples used for studies of associated W production. Predicted cross-sections have large theoretical uncertainties, and are not listed.

Description	Generator	Order
DPS $J/\psi + W^{\pm}$	`Pythia`	LO
Color-singlet SPS $J/\psi + W^{\pm}$	`HelacOnia` + `Pythia`	LO
Color-octet SPS $J/\psi + W^{\pm}$	`HelacOnia` + `Pythia`	LO
Color-singlet SPS $J/\psi + W^{\pm}$	`MadOnia` + `Pythia`	LO
Color-octet SPS $J/\psi + W^{\pm}$	`MadOnia` + `Pythia`	LO

serve a model for leptons from hadronic decays, often called "fake leptons."

4.4.3 Associated $J/\psi + W^{\pm}$ Samples

Five MC simulation samples of associated prompt J/ψ+$W^{\pm}$ production were created for this analysis: one of double-parton scattering production, two samples of color-singlet single-parton scattering, and two samples of color-octet single-parton scattering. The two matrix element generators used for the SPS samples are `MadOnia` [108] and `HelacOnia` [109]. All samples were produced at LO, since an NLO generator does not exist for these processes. Each of these samples were produced using the aforementioned AFII software for the detector simulation step. A summary of these samples is presented in Table 4.2.

The DPS $J/\psi + W^{\pm}$ sample was generated, hadronized, and showered with `Pythia8` using the `AU2` tune and the `CTEQ6L1` set of parton distribution functions (PDFs). Multidimensional PDFs for DPS processes are not yet widely studied or available, so the DPS factorization assumption of Eq. 1.6

is used. That is, the DPS MC sample assumes uncorrelated J/ψ and $W^{\pm}$ production within the same vertex.

MadOnia, which is a heavy quarkonia package that runs on the matrix element generator MadGraph 4, was used to generate color-singlet and color-octet samples of SPS associated production. I used MG_ME_V4.5.2 with the CTEQ6L1 PDFs to generate LHE events in a private production. The hard scatter LHE events from MadGraph were then interfaced to Pythia8 (again using the AU2 tune) for hadronization and showering.

Another event generator, HelacOnia, which performs the automated computation of heavy-quarkonium helicity amplitudes, was used to produce color-singlet and color-octet samples. For this sample, the package version HELAC-Onia-2.5.5 was used with the CTEQ6L1 PDFs. The samples were again interfaced to Pythia8 with the AU2 tune for hadronization and showering.

4.4.4 SPS Generator Parameters

There are a number of free parameters which can be tuned in both of the SPS matrix element generators that I used, MadOnia and HelacOnia. Most relevant of these are the long-distance matrix elements (LDMEs) from Eq. 1.4. The LDMEs are designed to be universal parameters which model a variety of quarkonia production processes. The color-singlet LDMEs can be estimated using a potential model [110], while the color-octet values are determined by fits to data[111–117]. The specific values used for the generation of the MC samples used in the SPS productions are listed in Table 4.3.

Table 4.3: LDMEs for SPS production. The values differ because the two generators use different conventions for defining these model parameters.

LDME	`MadOnia`	`HelacOnia`
$^1S_0^{[1]}$	0.0645	0.3867
$^3S_1^{[1]}$	0.0645	1.1600
$^1P_0^{[1]}$	0.0179	0.0000
$^3P_0^{[1]}$	0.0179	0.1074
$^3P_1^{[1]}$	0.0179	0.3223
$^3P_2^{[1]}$	0.0179	0.5371
$^1S_0^{[8]}$	0.0095	0.3533
$^3S_1^{[8]}$	0.0027	1.0600
$^1P_0^{[8]}$	0.0013	0.0000
$^3P_0^{[8]}$	0.0013	0.0000
$^3P_1^{[8]}$	0.0013	0.0000
$^3P_2^{[8]}$	0.0013	0.0000

Chapter 5

Data and Event Selection

5.1 Run 2 Dataset

This analysis uses $139\,\text{fb}^{-1}$ of pp collision data at $\sqrt{s} = 13\,\text{TeV}$ collected from 2015 until 2018. Events were required to have been collected during periods of stable proton beams with all ATLAS sub-detectors operational.

The data are segmented in time using the "lumiblock" and "run" units. A lumiblock corresponds to about one minute of data-taking, where LHC beam and ATLAS detector conditions are considered to be constant. Many lumiblocks are combined into a single run. Lumiblocks with good conditions from each year are recorded in an XML file called a "good run list" (GRL). The measured luminosities [66, 67] associated with each GRL are listed in Table 5.1. The total luminosity measurement has an uncertainty of 1.7%. However, because this analysis involves a ratio of two cross-sections, that uncertainty does not contribute significantly to the result.

5.2 Trigger Selection

Both inclusive $W^{\pm}$ and associated $J/\psi + W^{\pm}$ events are required to pass at least one single lepton trigger, which must later be matched to the $W^{\pm}$

Table 5.1: Good run lists and measured luminosities for Run 2 pp collision data-taking periods.

Year	Periods	Processing	Defect	$\mathcal{L}$ (fb^{-1})
2015	D-J	`pro21-02`	`v89`	3.22
2016	A-L	`pro21-01`	`v89`	32.99
2017	B-K	`pro22-01`	`v99`	44.31
2018	B-Q	`pro22-04`	`v102`	58.45

candidate. (Thus, when the ratio of these two cross-sections is calculated, the trigger and reconstruction efficiencies of the two quantities effectively cancel out.)

The trigger menu is determined based on a need to balance high signal efficiency, low background efficiency, and maintaining a combined trigger rate that stays within the available bandwidth of the ATLAS readout and storage system. At high p_{T} (approximately 60 GeV for electrons and 50 GeV for muons), a relatively loose set of requirements on the trigger object candidate still results in a sufficiently low single-lepton trigger rate. However, at lower p_{T} values, additional isolation requirements are placed on the trigger object candidates to improve the rejection of backgrounds.

This analysis uses the lowest unprescaled single-lepton triggers. A summary is presented in Table 5.2. The trigger names follow a predictable naming convention. The high-level triggers—the ones which initiate a full readout and storage of an event—all begin with "HLT_." The next letter indicates what type of trigger it is; for this analysis, single-electron ("e") and single-muon ("mu") triggers are used. The number that follows is the threshold for trans-

Table 5.2: Summary of the lowest unprescaled single-lepton triggers used in this analysis to identify a $W^{\pm}$ candidate. The trigger naming conventions are described in the body.

Year	**Electron Triggers**	**Muon Triggers**
2015	HLT_e24_lhmedium_L1EM20VH HLT_e60_lhmedium HLT_e120_lhloose	HLT_mu20_iloose_L1MU15 HLT_mu50
2016–8	HLT_e26_lhtight_nod0_ivarloose HLT_e60_lhmedium_nod0 HLT_e140_lhloose_nod0	HLT_mu26_ivarmedium HLT_mu50

verse energy or momentum. (Typically, a p_{T} cut that is a few GeV higher is placed on the fully reconstructed object to ensure a high trigger efficiency.) What follows the threshold tag is a set of other requirements. The trigger object may be required to pass some likelihood identification requirements, primary vertex association requirements, or isolation requirements. These requirements are used to keep the overall trigger rate sufficiently low, while still ensuring high signal efficiency.

The single-lepton triggers are designed to provide a large dataset of electroweak processes, such as the production of $W^{\pm}$ bosons, Z bosons, and top quarks. They play an important role in the ATLAS physics program, and so the combination of these triggers alone constitutes about 20% of the total readout bandwidth of the ATLAS trigger system. The combined efficiency of these triggers is shown in Figure 5.1.

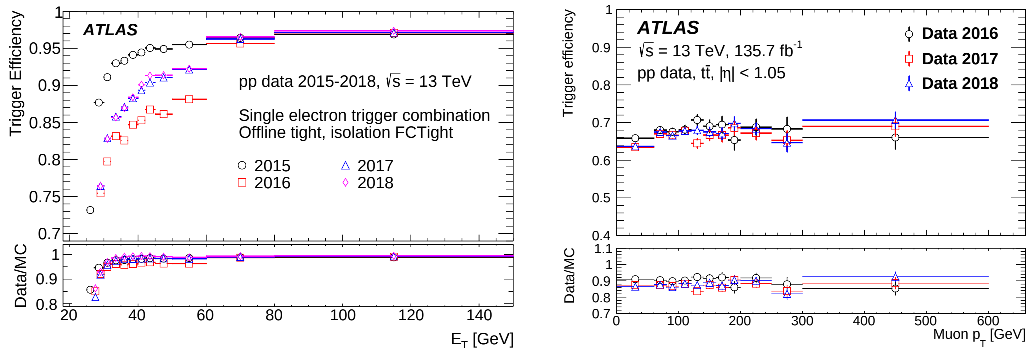

Figure 5.1: Efficiency of the combined single-lepton triggers as a function of the transverse energy or momentum of the fully reconstructed object. Images courtesy of Refs. [118] and [119].

5.3 Event Selection

An event primary vertex is chosen as the reconstructed vertex with the highest $\sum p_{\mathrm{T}}^2$ of all reconstructed tracks. Inclusive $W^{\pm}$ events are identified by requiring a high-momentum lepton—reconstructed and identified according to the algorithms detailed in Chapter 3—that is consistent with a $W^{\pm}$ decay. Associated events are identified with the same lepton requirements, but these events must contain an additional pair of muons consistent with a J/ψ decay.

5.4 Inclusive $W^{\pm}$ Selection

For both inclusive $W^{\pm}$ and associated $J/\psi + W^{\pm}$ events, a $W^{\pm}$ candidate is selected from the subset of events passing one of the unscaled single-lepton triggers in Table 5.2. The event must have a fully reconstructed and calibrated electron or muon that is matched to one of the passed triggers. The lepton must have $p_{\mathrm{T}} > 27\,\mathrm{GeV}$ and $|\eta| < 2.5$. The candidate $W^{\pm}$ lepton is

Table 5.3: Selection criteria used to identify $W^{\pm}$ candidates in inclusive and associated events.

$W^{\pm}$ **Lepton Requirements**
Tight quality lepton ID
$p_{\mathrm{T}} > 27\,\mathrm{GeV}$
$\lvert\eta\rvert < 2.5$
Single-lepton trigger match
Prompt lepton BDT tag
$\lvert z_0 \sin(\theta)\rvert < 0.5$
$\lvert d_0\rvert / \sigma_{d_0} < 5(3)$ for $e^{\pm}(\mu^{\pm})$
Crack electron veto: $\left\lvert\eta^{e^{\pm}}\right\rvert \notin (1.37, 1.52)$
Event Requirements
$E_{\mathrm{T}}^{\mathrm{miss}} > 20\,\mathrm{GeV}$
$M_T(W^{\pm}) > 40\,\mathrm{GeV}$
No tight $\ell^+\ell^-$ pair (except J/ψ candidate)

required to originate from the event primary vertex by applying track parameter cuts. Events are required to have missing energy and a large transverse mass. The transverse mass is a quantity defined from a combination of the transverse properties of the lepton and the neutrino/$E_{\mathrm{T}}^{\mathrm{miss}}$, and is defined as

$$m_T\left(W^{\pm}\right) = \sqrt{2p_{\mathrm{T}}^{\ell^{\pm}} E_T^{\mathrm{miss}}\left(1 - \cos\left(\phi^{\ell^{\pm}} - \phi^{\nu}\right)\right)}. \tag{5.1}$$

To select prompt leptons from $W^{\pm}$ decays and remove non-prompt leptons from heavy flavor decays, lepton isolation criteria are applied. This is done using the output of a Boosted Decision Tree (BDT) to separate these two components [120]. The full set of $W^{\pm}$ boson selection criteria are summarized in Table 5.3.

Table 5.4: J/ψ selection criteria.

J/ψ **Muon Requirements**
Low-p_{T} quality lepton ID
$p_T > 3\,\mathrm{GeV}$
$\lvert\eta\rvert < 2.5$
Not $W^{\pm}$ candidate lepton
Di-muon Requirements
Opposite sign pair
Fit to common vertex
$p_{\mathrm{T}}^{\mu\mu} \in (8, 200)\,\mathrm{GeV}$
$\lvert y^{\mu\mu}\rvert < 2.1$
$m^{\mu\mu} \in (2.7, 3.6)\,\mathrm{GeV}$
$\tau^{\mu\mu} \in (-1, 9)\,\mathrm{ps}$
$\lvert\Delta z_0 \sin(\theta)\rvert < 10\,\mathrm{mm}$

5.5 Associated $J/\psi + W^{\pm}$ Selection

Associated $J/\psi + W^{\pm}$ events must pass all the requirements in §5.4, and must include two additional muons. Each muon must pass the low-p_{T} working point [87], have $p_{\mathrm{T}} > 3\,\mathrm{GeV}$, and have $|\eta| < 2.5$. The muons must have opposite charges, be fit to a common vertex, and have an invariant mass near that of the known J/ψ mass. The di-muon vertex is then considered a J/ψ candidate, which is required to have $p_{\mathrm{T}} > 8\,\mathrm{GeV}$, $|y| < 2.1$, and separation from the primary vertex $|\Delta z_0 \sin(\theta)| < 10\,\mathrm{mm}$. Neither J/ψ muon may simultaneously serve as the $W^{\pm}$ candidate muon. The J/ψ selections are summarized in Table 5.4.

In associated $J/\psi + W^{\pm}$ events, once J/ψ and $W^{\pm}$ candidates are both identified, final cuts are placed on the *pair* of objects. In $W \to \mu\nu_{\mu}$ events, we consider the di-muon pair formed by the $W^{\pm}$ muon and the muon

Table 5.5: Pair selection criteria.

$J/\psi + W^{\pm}$ **Requirements**
$m\left(\mu_{W^{\pm}}, \mu_{J/\psi}^{\text{O.S.}}\right) \notin (81, 101)\,\text{GeV}$
$m\left(\ell_{W^{\pm}}, \mu_{J/\psi}^{1}, \mu_{J/\psi}^{2}\right) \notin (6.25, 6.30)\,\text{GeV}$
$\lvert\Delta z\,(J/\psi, W^{\pm})\rvert < 0.5\,\text{mm}$

in the J/ψ candidate with an opposite electrical charge. Events are vetoed when the invariant mass of this pair lies within 10 GeV of the Z boson mass. Additionally, events are vetoed where the invariant mass of the three-lepton system lies within 25 MeV of the B_c mass. Finally, to reduce the background from pileup, a cut on $\lvert\Delta z\,(J/\psi, W^{\pm})\rvert$ is applied. The cuts on the object pair are summarized in Table 5.5.

5.6 Yields

The total number of events passing the associated $J/\psi + W^{\pm}$ selections is 25,934. Figure 5.2 shows the cumulative effects of applying each successive cut to the initial (preselected) dataset. The final dataset includes the prompt $J/\psi + W^{\pm}$ signal, as well as backgrounds originating from non-prompt J/ψ mesons, combinatorics, fake leptons, associated prompt $J/\psi + Z$ production, and pileup. In the following chapter, I will discuss how the signal is extracted, and the remaining backgrounds are estimated.

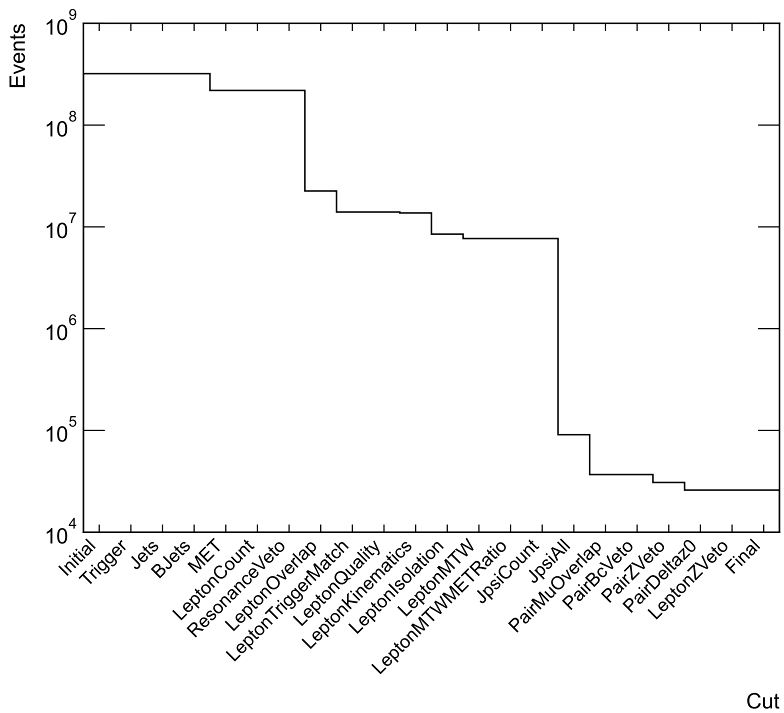

Figure 5.2: Cutflow diagram for the selections described in the previous sections.

Chapter 6

Signal Extraction and Background Estimation

6.1 Prompt J/ψ Extraction

The selection of associated events described in Chapter 5 includes some unknown number of combinatorial background (a muon pair with an invariant mass near the J/ψ peak, but which did not originate from a J/ψ) and non-prompt J/ψ candidates (production originating from b-hadron decay). Therefore, I seek to extract only the component of the data from prompt J/ψ production. The di-muon invariant mass $m^{\mu^+\mu^-}$ is used to distinguish the signal from the combinatorial background. Similarly, the pseudo-proper decay time,

$$\tau^{\mu^+\mu^-} \equiv L_{xy} \cdot m^{\mu^+\mu^-} / p_T^{\mu^+\mu^-}, \tag{6.1}$$

where L_{xy} is the transverse decay length in the laboratory frame[1], is used to separate prompt from non-prompt J/ψ production. The two-dimensional distribution of events passing all the associated J/ψ selections is shown in Figure 6.1.

It is impossible to reject combinatorial and non-prompt backgrounds

[1] $L_{xy} = \frac{\mathbf{L} \cdot \mathbf{p}_{\mathrm{T}}^{\mu^+\mu^-}}{p_{\mathrm{T}}^{\mu^+\mu^-}}$, where $\mathbf{L}$ is the displacement vector of the J/ψ vertex.

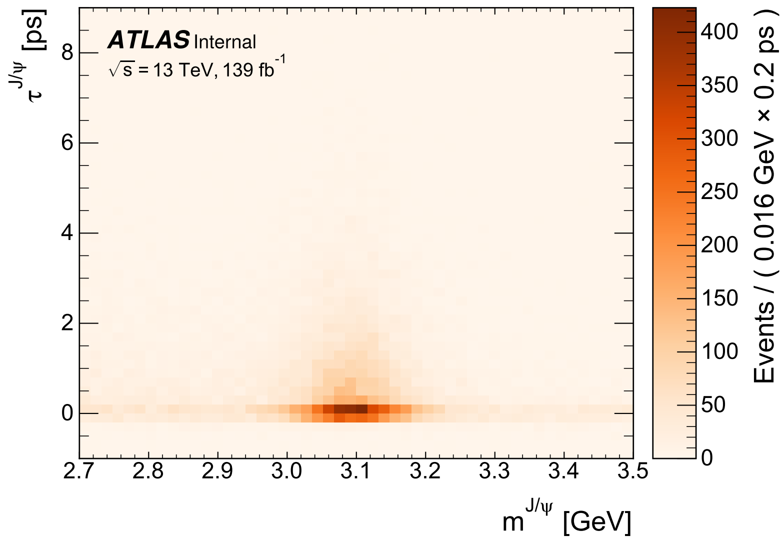

Figure 6.1: Distribution of J/ψ candidate mass and τ for events passing the associated selections. These events include prompt, non-prompt, and combinatorial background.

using cuts alone. One cannot distinguish, for example, a J/ψ candidate with $\tau = 0$ which comes from prompt production, or one which comes from the lower edge of a single-sided exponential distribution modelling the non-prompt production. Similarly, a di-muon candidate with an invariant mass near the 3.1 GeV J/ψ mass peak may have been a true J/ψ, or it may simply be combinatorial background that just happens to fall near that value. One can only say *in aggregate* how many true J/ψ mesons were produced. For this, one must use statistical methods.

For that reason, I use the "s-plot" procedure [121]. For this, I fit the data to a model probability density function (PDF) in m and τ, and generate an s-weight for each event. The s-weights are then used to re-weight the

Table 6.1: Mass-τ model used to generate s-weights for associated events.

Component	**Function**
Prompt Signal	$f_m * CB\left(m;\sigma_{CB},\alpha,n\right) + (1-f_m) * G\left(m;\sigma_G\right)$ $\delta\left(\tau\right) \otimes R\left(\tau;\sigma_\tau,f_R\right)$
Prompt Comb.	$\mathcal{P}_1\left(m\right)$ $\delta\left(\tau\right) \otimes R\left(\tau;\sigma_\tau,f_R\right)$
Non-prompt Signal	$f_m * CB\left(m;\sigma_{CB},\alpha,n\right) + (1-f_m) * G\left(m;\sigma_G\right)$ $\exp\left(-\lambda_S\tau\right) \otimes R\left(\tau;\sigma_\tau,f_R\right)$
Non-prompt Comb. 1	$\mathcal{P}_1\left(m\right)$ $\exp\left(-\lambda_{C1}\tau\right) \otimes R\left(\tau;\sigma_\tau,f_R\right)$
Non-prompt Comb. 2	$\mathcal{P}_1\left(m\right)$ $\exp\left(-\lambda_{C2}\left\|\tau\right\|\right) \otimes R\left(\tau;\sigma_\tau,f_R\right)$
τ Resolution (R)	$f_R * \exp\left(\frac{-\tau^2}{2\sigma_\tau^2}\right) + (1-f_R) * \exp\left(\frac{-\tau^2}{8\sigma_\tau^2}\right)$

data to match the underlying distribution produced by prompt production, non-prompt production, or combinatorial background. In each J/ψ p_T and rapidity bin, the data are fit to a two-dimensional m-τ model, and weights for prompt signal, non-prompt signal, and background are generated.

The model used for s-weighting is as follows. In the mass dimension, the signal is modelled by the sum of a Crystal Ball function and a Gaussian, while the background is modelled by an exponential. The prompt signal is modelled by a delta function at $\tau = 0$ convolved with a resolution function, while the non-prompt is modelled by the sum of a single-sided and double-sided exponential. The lifetime parameters of the exponential functions are allowed to float independently for the signal and background components. The full model is detailed in Table 6.1.

Because of the large number of parameters of this model for a relatively small associated dataset, all parameters of the model, except the yields, are fixed using inclusive J/ψ data (not associated with a $W^{\pm}$). This inclusive J/ψ dataset is obtained by applying the J/ψ selections in Table 5.4 to the Run 2 data. Then, with all parameters left floating, I fit the model to this large dataset in each p_{T}/y bin. Finally, each model is fit to the corresponding associated $J/\psi + W^{\pm}$ data, where only the yield parameters are permitted to float.

A fit of the model to the data is performed separately in each p_T/y bin. Each of the twelve fits was examined individually and found to sufficiently model the data for the purposes of calculating s-weights. The data and results of one bin's two-dimensional fit, projected onto the invariant mass and τ axes, is shown in Figure 6.2. In Figure 6.3, the 2D fits are summed across all twelve J/ψ bins. The pulls of the summed fits, shown in Figure 6.4, show good agreement between the model and data, especially in the central region where the events are concentrated.

6.1.1 J/ψ Vertex Finding

In this analysis, I require that the reconstruction software efficiently identify J/ψ candidates (di-muon pairs) from the reconstructed muons in the event. The algorithm used to find J/ψ candidates is called JpsiFinder, and is

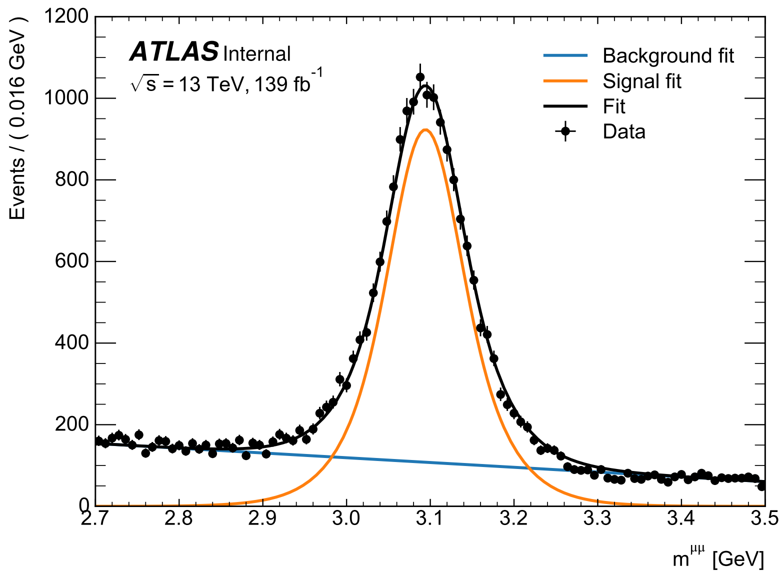

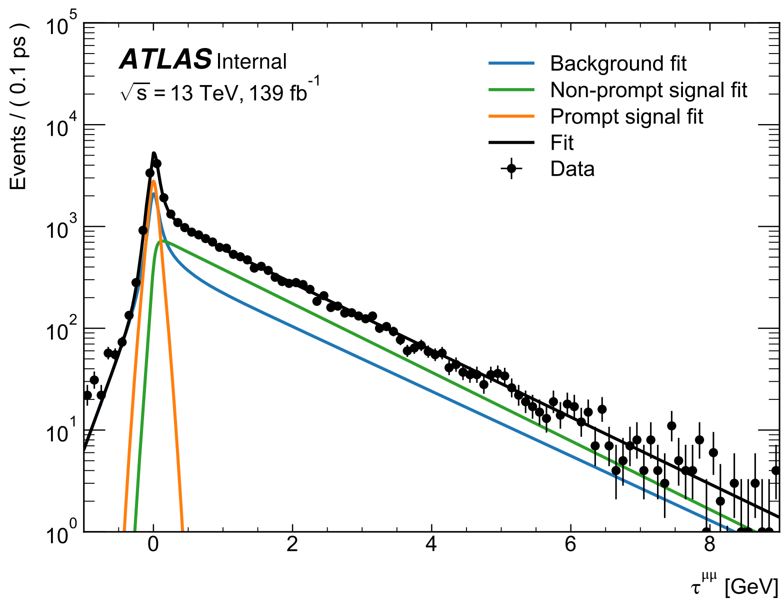

Figure 6.2: Projections of 2D fit in a single p_T/y bin onto the mass (top) and pseudo-proper time (bottom) dimensions. Components show the relative contributions of J/ψ signal (prompt and non-prompt) and combinatorial background.

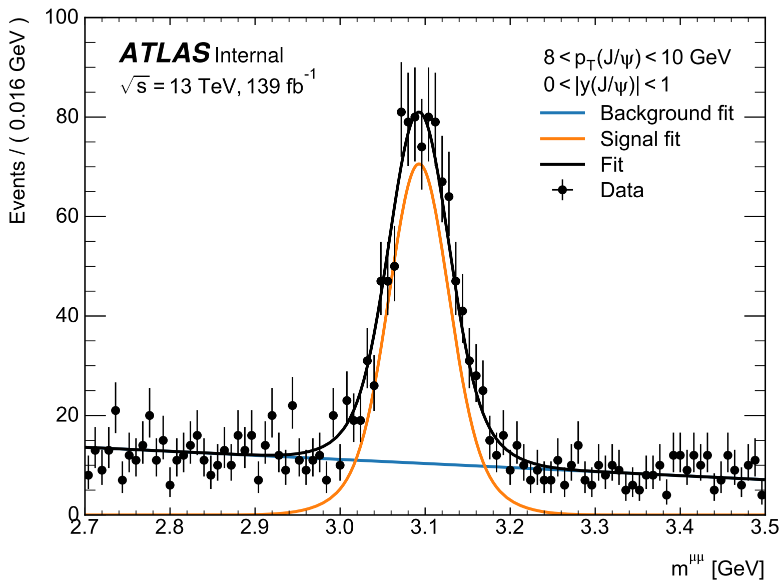

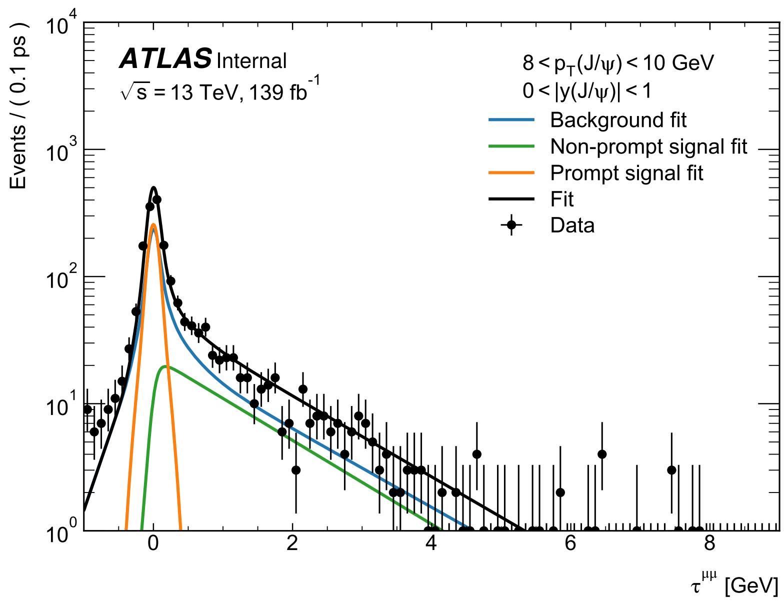

Figure 6.3: Projections of 2D fits integrated across the twelve J/ψ p_T/y bins and projected onto the mass and pseudo-proper time dimensions. Components show the relative contributions of J/ψ signal (prompt and non-prompt) and combinatorial background.

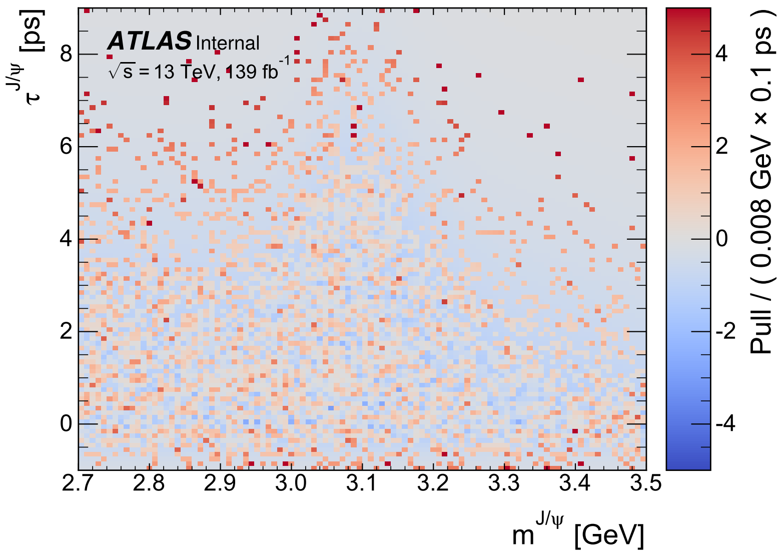

Figure 6.4: Pulls of the sum of the twelve independently-performed 2D fits of the data to the model. The fits were found to perform well, especially in the region near the prompt J/ψ signal peak.

centrally produced by the ATLAS B-physics and Light States (BLS) group. The algorithm operates by considering the set of reconstructed muons in an event. It then finds pairs of opposite-sign muons which are consistent with having originated from a common vertex. A loose chi-squared cut ($\chi^2 < 200$) is placed on how much track parameters must be adjusted to fit the pair to a common vertex.

I use simulated DPS $J/\psi + W^{\pm}$ events to measure the efficiency of this vertex-finding algorithm. For a given $J/\psi \to \mu^+\mu^-$ decay, where the J/ψ lies within the fiducial region and both decay muons are reconstructed, I measure the efficiency with which the J/ψ is identified as a di-muon vertex. In DPS events, I observed that 99.9% of true J/ψ's in the event record were identified

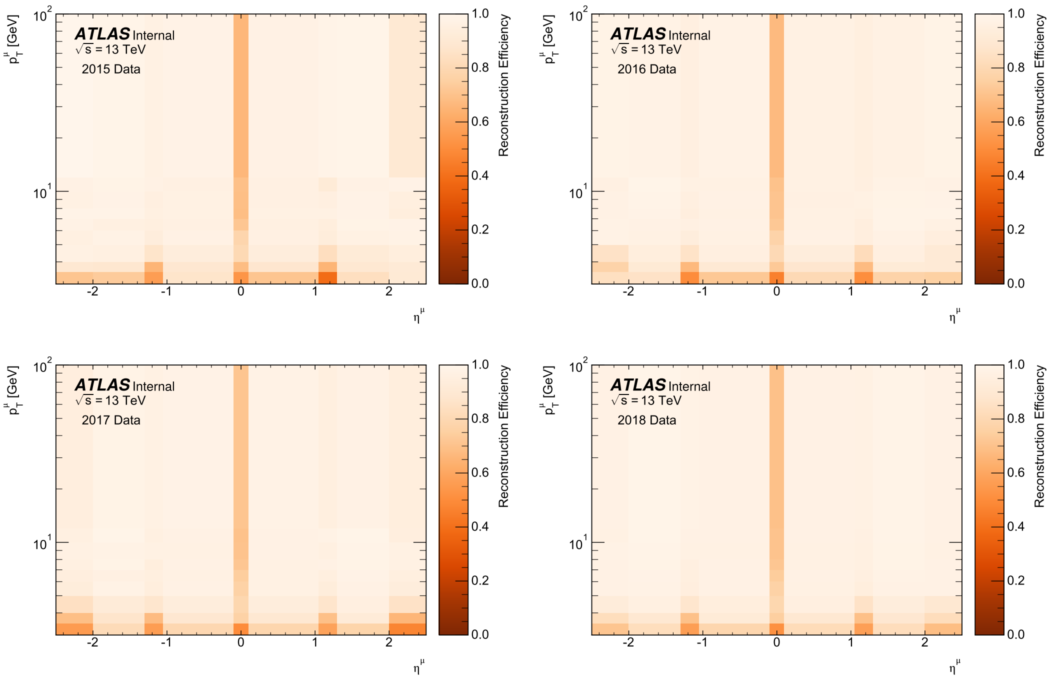

Figure 6.5: Muon efficiency maps for each of the four years of data-taking, calculated as a function of muon p_{T} and η.

from reconstructed muons using this algorithm.

6.1.2 Efficiency and Acceptance Corrections

To account for the acceptance and efficiency effects related to J/ψ reconstruction, each event is weighted by inverse of the efficiency and acceptance factors,

$$w = \frac{1}{\epsilon\left(\mu_1\right) \times \epsilon\left(\mu_2\right) \times \mathcal{A}\left(J/\psi\right)}. \tag{6.2}$$

Muon reconstruction efficiency maps $\epsilon\left(\mu\right)$ have been derived centrally by the Muon Combined Performance (CP) group for the Low-p_{T} muon ID working point. For each J/ψ muon, I obtain the reconstruction efficiency as a function of the muon transverse momentum and pseudo-rapidity. The muon reconstruction efficiency maps used, separated into the four data-taking years, are shown in Fig. 6.5.

Similarly, I re-weight the observed events to account for detector acceptance $\mathcal{A}$ of the J/ψ. A generator-level analysis is performed to derive acceptance maps for the J/ψ. To do this, I calculate the probability that a J/ψ with a given p_{T} and y will decay into two muons which pass the p_{T} and η acceptance criteria in §5.5. The J/ψ polarization is not experimentally known for associated $J/\psi + W^{\pm}$ production. Therefore, I calculate these acceptance corrections for seven possible spin-alignment profiles. These are presented in Fig. 6.6. The range of these results is used as the spin-alignment uncertainty on the final measurement of the cross-section ratio.

6.2 Associated $J/\psi + W^{\pm}$ Background Estimations

6.2.1 QCD Multi-jet

One background process that enters the signal region is QCD multi-jet production. These events do not involve the production of a real $W^{\pm}$, but do mimic the final state signature used for this analysis. These are multi-jet events (typically involving one more b-decays) which include a high-p_{T} lepton from a hadronic source and a J/ψ. The characteristic example would be $b\bar{b}$ event, in which one b decay includes a lepton, and the other decays via $J/\psi \to \mu\mu$. These types of events often referred to as "non-prompt leptons"

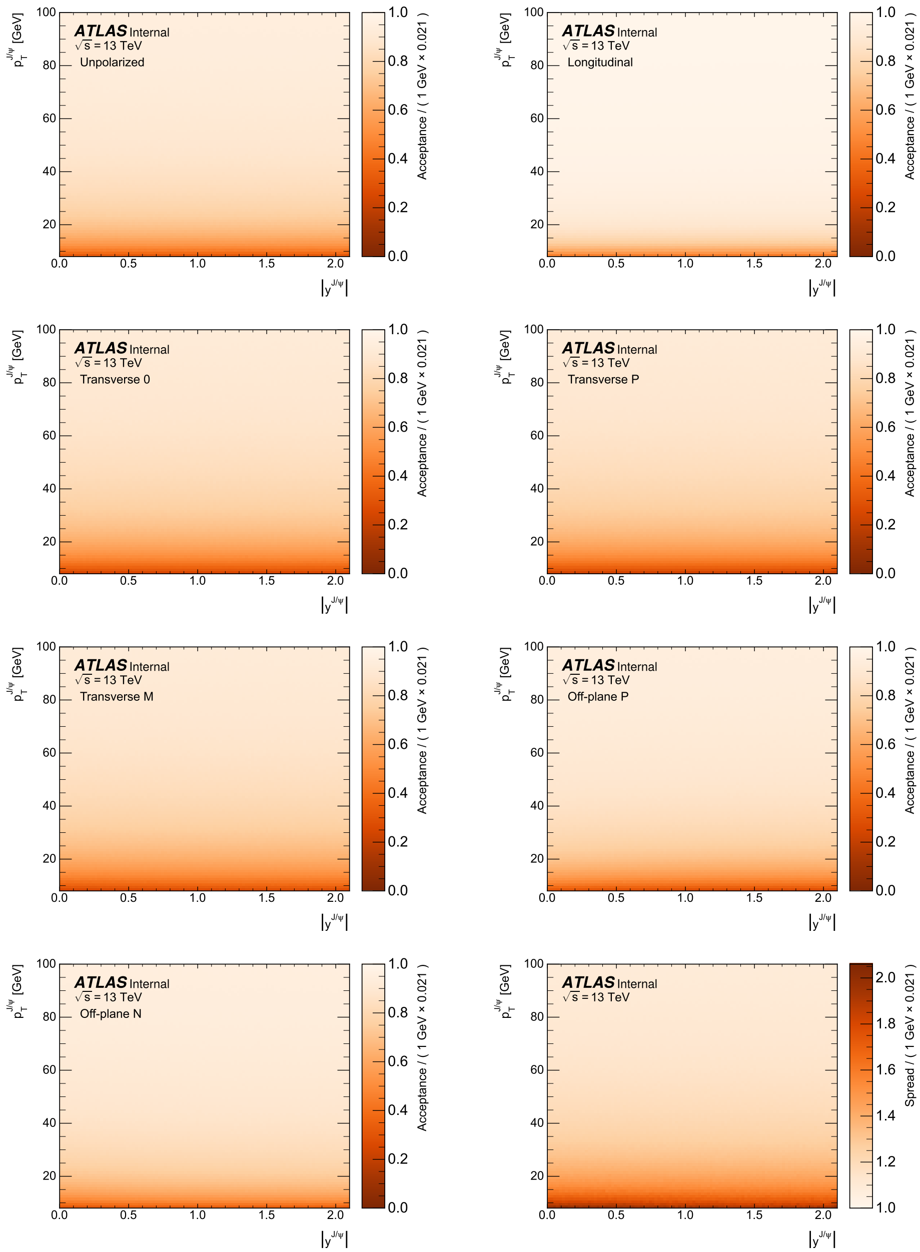

Figure 6.6: J/ψ acceptance maps as a function of $p_{\mathrm{T}}^{J/\psi}$ and $y^{J/\psi}$. Acceptance values are calculated for a variety of spin-alignment profiles. Additionally, the bottom-right plot shows the ratio of the largest value of the seven acceptance maps to the smallest value in each bin.

Table 6.2: The QCD multi-jet background is largely eliminated by using a number of cuts, which are listed here.

Cut	**Purpose**
Overlap removal	Removes leptons near jets.
Prompt lepton veto BDT [120]	PLV is a centrally-produced isolation algorithm to identify prompt leptons and reject non-prompt leptons from b-decays.
$p_{\mathrm{T}}^{\ell} > 27\,\mathrm{GeV}$	QCD multi-jet events have a lower lepton p_{T} spectrum than the high-p_{T} leptons from $W^{\pm}$ decays.
$E_{\mathrm{T}}^{\mathrm{miss}} > 20\,\mathrm{GeV}$	QCD multi-jet events have low $E_{\mathrm{T}}^{\mathrm{miss}}$, whereas $W^{\pm}$ events have a high-p_{T} neutrino.
$M_T\,(W^{\pm}) > 40\,\mathrm{GeV}$	Identifies a $W^{\pm}$ boson in the event. QCD multi-jet events have low transverse mass.

or "fake leptons," and should not be included in the measurement. Most of this background is removed by applying the set of cuts in Table 6.2.

To estimate the remaining contribution of QCD multi-jet events to the signal region, I use a template fit method. I construct a new region that is rich in QCD multi-jet background by inverting the $E_{\mathrm{T}}^{\mathrm{miss}}$, $M_T\,(W^{\pm})$, and PLV isolation cuts. A $b\bar{b}$ simulation sample is then used to estimate the transfer factor of background events to the signal region. A detailed description of the fit procedure is provided in §6.2.3.

6.2.2 Prompt $J/\psi + Z$

A similar method is used to estimate the contribution of prompt J/ψ+Z events to the signal. These events are initially removed from the signal region by rejecting events with a second opposite-sign pair of tight leptons (in addition to the J/ψ di-muon pair), each with $p_{\mathrm{T}} > 10\,\mathrm{GeV}$. The selection efficiency

Table 6.3: The data are divided into six selections regions. Region A is rich in signal, region D is rich in QCD multi-jet background, and region F is rich in prompt $J/\psi + Z$. The other three regions are mixtures.

Region	$E_{\mathrm{T}}^{\mathrm{miss}}$	$M_T\,(W^{\pm})$	Isolation	OS Pair
A	$> 20\,\mathrm{GeV}$	$> 40\,\mathrm{GeV}$	Isolated	Veto
B	$> 20\,\mathrm{GeV}$	$> 40\,\mathrm{GeV}$	Anti-isolated	Veto
C	$< 20\,\mathrm{GeV}$	$< 40\,\mathrm{GeV}$	Isolated	Veto
D	$< 20\,\mathrm{GeV}$	$< 40\,\mathrm{GeV}$	Anti-isolated	Veto
E	$> 20\,\mathrm{GeV}$	–	Isolated	Anti-veto
F	$< 20\,\mathrm{GeV}$	–	Isolated	Anti-veto

of this cut was found to be near unity for prompt $J/\psi + W^{\pm}$ events. The remaining prompt $J/\psi + Z$ events are expected to be events where one of the Z decay leptons is lost (on account of acceptance, reconstruction efficiency, failing lepton ID cuts, or for some other reason).

The $E_{\mathrm{T}}^{\mathrm{miss}}$ and di-lepton requirement cuts are inverted and the $M_T\,(W^{\pm})$ cut is removed, creating a data sample which is background-rich in prompt $J/\psi + Z$. Then, a Z+jets MC sample is used to estimate the transfer factor of events from the background region to the signal region. A detailed description of the fit procedure is provided in §6.2.3.

6.2.3 Simultaneous QCD multi-jet and prompt $J/\psi + Z$ Fit

To estimate the QCD multi-jet and prompt $J/\psi + Z$ backgrounds, the prompt-J/ψ s-weighted data are first separated into the $W^{\pm} \to e^{\pm}\nu_e$ and $W^{\pm} \to \mu^{\pm}\nu_{\mu}$ channels, as the backgrounds may differ between the two lepton flavors. Then, the data are further subdivided into the six regions defined in Table 6.3. Region A is rich in signal, region D is rich in QCD multi-jet background, and region F is rich in prompt $J/\psi + Z$. The other three regions are mixtures.

The distributions from data are fit to a sum of three MC templates, where each models one of the three components in the prompt J/ψ data. A DPS template models the signal shape, a $b\bar{b}$ sample models the lepton behavior of QCD multi-jet events, and a Z+jets sample models the lepton behavior in prompt $J/\psi + Z$ events. Since these are backgrounds which only involve the $W^{\pm}$ candidate lepton, not the J/ψ, the $b\bar{b}$ and Z+jets samples are reasonable choices to model the $W^{\pm}$ candidate lepton's behavior in these events.

The fit results, integrated across all J/ψ bins, are shown in Fig. 6.7. The background-rich regions (D for QCD multi-jet and F for prompt $J/\psi+Z$) strongly constrain the number of background events in the signal region. I estimate the contribution of QCD multi-jet events to be 2.6% across all p_{T}/y bins, while the prompt $J/\psi+Z$ contributes a total of 3.9% to the signal region. When calculating the final cross-section ratio, the QCD multi-jet and prompt $J/\psi + Z$ backgrounds are estimated and subtracted separately in each bin. The estimates for the QCD multi-jet and prompt $J/\psi + Z$ backgrounds are listed in Tables A.1–A.4. Systematic uncertainties relating to this procedure are discussed in §8.2.

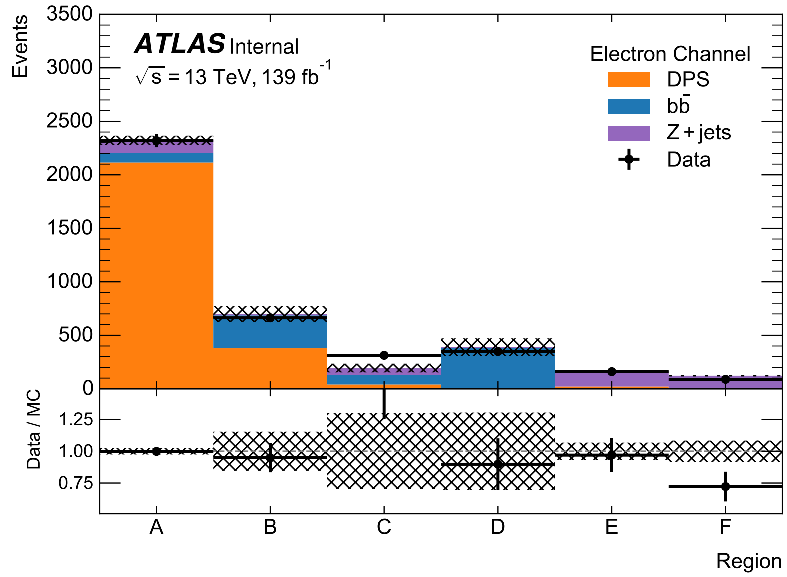

Figure 6.7: Estimations of the QCD multi-jet and prompt $J/\psi+Z$ background in the electron channel, summed over all bins. A template fit is performed to the s-weighted data to determine the signal fraction in the analysis region (A).

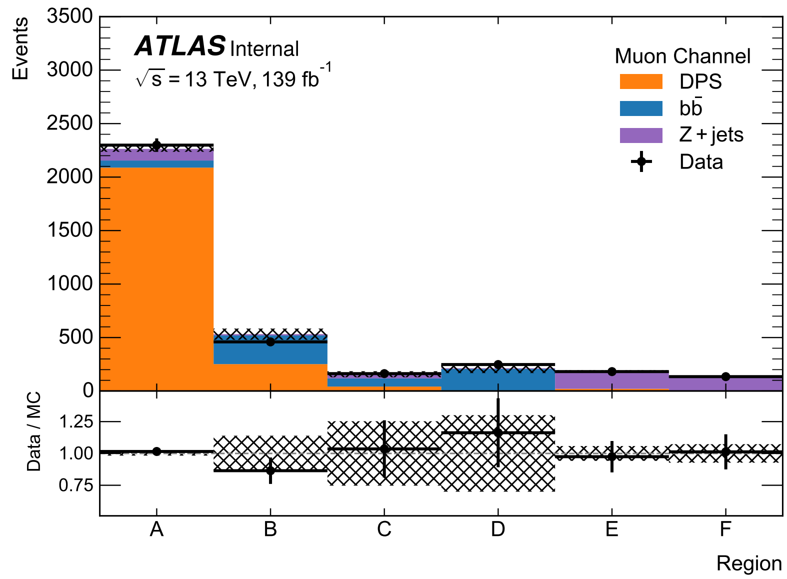

Figure 6.8: Estimations of the QCD multi-jet and prompt $J/\psi + Z$ background in the muon channel, summed over all bins. A template fit is performed to the s-weighted data to determine the signal fraction in the analysis region (A).

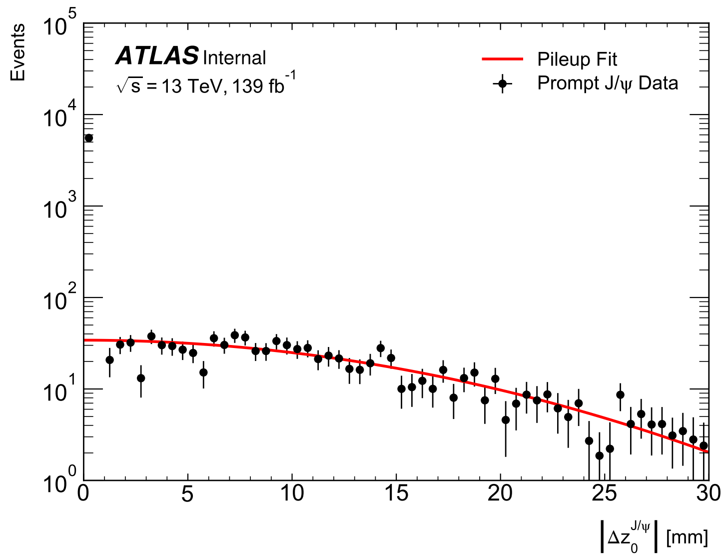

Figure 6.9: The pileup is estimated by fitting a Gaussian PDF to the wide component of the Δz_0 distribution in the region $|\Delta z_0| > 3\,\text{mm}$, and extrapolating to the region at $|\Delta z_0| < 0.5\,\text{mm}$.

6.2.4 Pileup

I seek to estimate events in which one pp interaction in a single bunch crossing produces a $W^\pm$, and another pp scattering in the same bunch crossing produces a J/ψ. These events are studied by considering the z-separation (the distance along the beam axis) between the $W^\pm$ and J/ψ vertices. Pileup has a very broad $|\Delta z_0|$ distribution, while the prompt $J/\psi + W^\pm$ signal is characterized by a sharp peak at $\Delta z_0 = 0\,\text{mm}$. Thus, the pileup background is effectively removed by the cut of $|\Delta z_0| < 0.5\,\text{mm}$.

To estimate the number of pileup events passing the $|\Delta z_0|$ cut and entering the signal region, I removed this Δz_0 cut. The distribution of this variable (without the cut) in prompt $J/\psi + W^{\pm}$ events is shown in Fig. 6.9. A fit is performed to the wide Gaussian component in the region $|\Delta z_0| \in (3, 30)$ mm. The value of the fit function in the region $|\Delta z_0| < 0.5$ mm is then used to estimate the pileup contribution. With this method, I find the pileup contribution is 1.2% of events integrated across all p_{T}/y bins.

6.3 Inclusive $W^{\pm}$ Background Estimations

I measure the backgrounds to the inclusive $W^{\pm}$ cross-secton using the same methodology developed in §6.2.3. The data are split into lepton flavor channels, and then further separated into six bins according to the selections of Table 6.3. I consider a number of electroweak backgrounds. Six-bin templates are generated from simulated events of Z+jets, $t\bar{t}$, single-t, di-boson (ZZ, WZ, and $W^{+}W^{-}$). Additionally, I use the QCD multi-jet template derived from a simulated sample of $b\bar{b}$ production. The signal template is generated from simulated W+jets events. Templates are generated separately for the electron and muon channels.

In the fit, the electroweak background templates are fixed to the normalization predicted by the MC generators, while the normalization parameters of the signal and QCD multi-jet samples are allowed to float. The results of the fits for the electron (muon) channel are shown in Fig. 6.10 (6.11). These fits result in an inclusive $W^{\pm}$ signal fraction estimate of 92.4% and 92.6% for the electron and muon channels, respectively. Systematic uncertainties relating to this background estimation are detailed in §8.3.

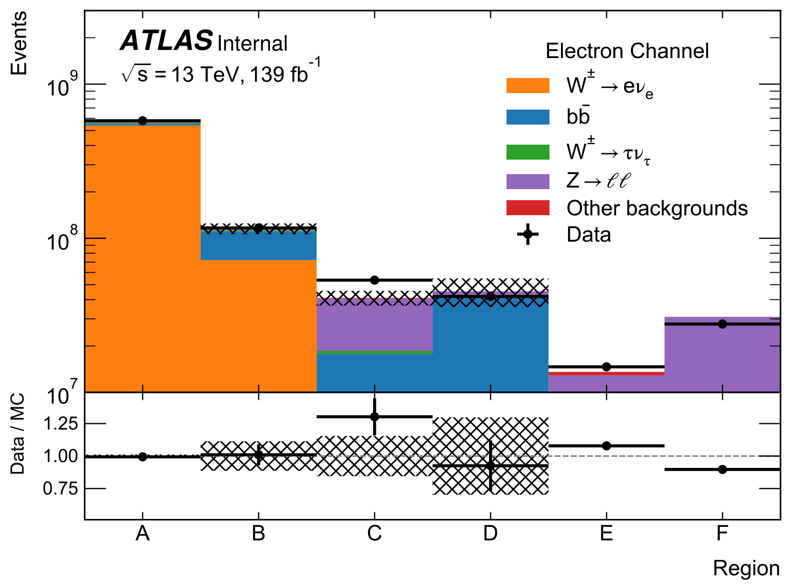

Figure 6.10: Estimation of the electroweak and QCD multi-jet backgrounds in the electron channel. A template fit is performed to the inclusive $W^{\pm}$ data to determine the signal fraction in the analysis region (A).

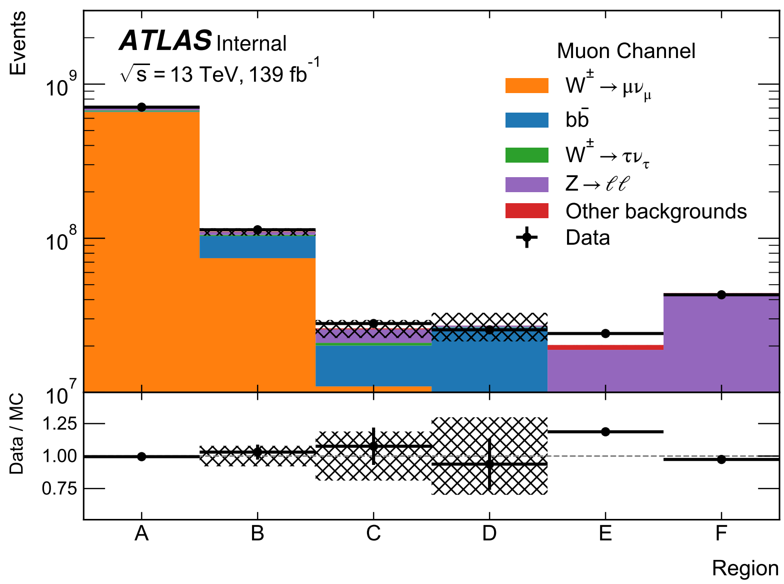

Figure 6.11: Estimation of the electroweak and QCD multi-jet backgrounds in the electron channel. A template fit is performed to the inclusive $W^{\pm}$ data to determine the signal fraction in the analysis region (A).

Chapter 7

Single and Double Parton Scattering

One of the components of prompt $J/\psi + W^{\pm}$ production is the simultaneous scattering of two *pairs* of partons in a single *pp* collision, called double-parton scattering. A sketch of DPS production is shown in Figure 1.5. This is prompt associated production in the sense that the two particles are always produced at the same vertex (with pseudo-proper time $\tau^{\mu\mu} = 0$). However, as this mode arises via an entirely different physical process as the QCD-based single-parton scattering production of heavy quarkonia, it is interesting for different physical reasons. Thus, it is useful to be able to measure these components individually. In this chapter, I will discuss how SPS and DPS may be distinguished experimentally, the issues that arise when using the standard separation techniques, and the methods I used to mitigate or avoid those issues.

7.1 Distinguishing Observables

It is not possible to separate the SPS and DPS production modes on an event-by-event basis. Instead, one can find a variable that is sensitive to the two production modes. Then, by building models for each production mode, one can estimate the relative contributions of each in data by performing a fit to a sum of those models. In previous studies of DPS interactions, a number of observables have been used for this purpose: some involve various combinations of the transverse momentum vectors of the system, while others use the angular separation between the two objects [122].

A variable which has been considered to experimentally distinguish SPS and DPS is the azimuthal separation between the J/ψ and the $W^{\pm}$ boson, $\Delta\varphi\,(J/\psi, W^{\pm})$. If one assumes that the two collisions in a DPS event are independent, then the directions of the J/ψ and $W^{\pm}$ momenta will be independent, corresponding to a flat $\Delta\varphi\,(J/\psi, W^{\pm})$ distribution. On the other hand, for SPS, the azimuthal separation between the two particles will be correlated, corresponding to a peaked distribution that peaks at $\Delta\varphi\,(J/\psi, W^{\pm}) = \pi$. In practice, one can produce MC samples for SPS and DPS, generate templates in the sensitive variable for each sample, and fit the data to a weighted sum of the templates.

7.2 $\Delta\varphi\,(J/\psi, W^{\pm})$ for DPS estimation

Using generator-level information, the MC templates of $\Delta\varphi\,(J/\psi, W^{\pm})$ accurately reproduce the expectation of a flat distribution for DPS and a back-to-back distribution for SPS. These distributions are shown as dotted lines in Figure 7.1. However, after the detector effects are applied, the shape of the distributions change. Using reconstruction information—the solid lines in Figure 7.1—the DPS likewise shows a strong peak at $\Delta\varphi\,(J/\psi, W^{\pm}) = \pi$. That is,

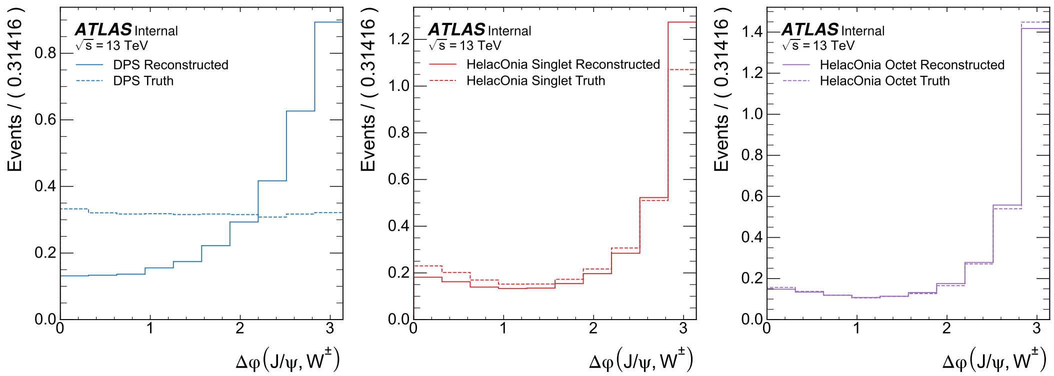

Figure 7.1: Distributions of $\Delta\varphi\left(J/\psi, W^{\pm}\right)$, the azimuthal angle separation between J/ψ and $W^{\pm}$, using reconstruction and truth information. SPS shapes are produced with the `HelacOnia` MC generator.

after the effects of reconstruction are applied, the shape of the $\Delta\varphi\left(J/\psi, W^{\pm}\right)$ MC templates for DPS and SPS are effectively indistinguishable. Consequently, fitting the data to a sum of these two components provides no predictive power on the relative yields of DPS and SPS in data, and $\Delta\varphi\left(J/\psi, W^{\pm}\right)$ is rendered ineffective as a distinguishing observable.

7.3 $E_{\mathrm{T}}^{\mathrm{miss}}$ Reconstruction Bias

I will now demonstrate how the observed mis-reconstruction of the $\Delta\varphi\left(J/\psi, W^{\pm}\right)$ is directly attributable to the experimental limitations of the detector. In each collision event, the momentum of a particle of interest (e.g. a J/ψ) is balanced in the transverse plane by hadronic activity. This is commonly called the "hadronic recoil." However, soft, forward, and neutral particles are all not reconstructed by the inner detector. Thus, these particles are not included in the track-based soft $E_{\mathrm{T}}^{\mathrm{miss}}$ term introduced in Chapter 3.

Consequently, the total $E_{\mathrm{T}}^{\mathrm{miss}}$ has a bias opposite the direction of the particle of interest. Finally, if this biased $E_{\mathrm{T}}^{\mathrm{miss}}$ variable is used to reconstruct a soft $W^{\pm}$, even a small bias in the reconstructed transverse momentum vector can have a significant impact on the reconstructed direction of the $W^{\pm}$. In the following sections, I will explore this topic in more depth.

7.3.1 Hadronic Recoil Acceptance

The $E_{\mathrm{T}}^{\mathrm{miss}}$ bias is best demonstrated using an inclusive J/ψ MC sample (not associated with a $W^{\pm}$). These simpler events consist of a J/ψ and a hadronic recoil; the true value of the $E_{\mathrm{T}}^{\mathrm{miss}}$ is 0. Using truth information, I calculate three quantities: the vector sum of all leptons in each event, the vector sum of all non-lepton particles in each event (the hadronic recoil), and the sum of all particles in each event. For an MC sample of J/ψ production, the first is effectively the momentum vector of the J/ψ. The second is essentially the sum of soft hadrons in the event, and is exactly the negative of the lepton vector. Thus, the third term was always identically zero. All of this was true *as long as no particle-level selections were applied.* The three quantities, projected onto the J/ψ momentum axis, are shown on the top half of Figure 7.2.

I then repeat this procedure with additional constraints: only particles with $q \neq 0$ and $|\eta| < 2.5$ are included in the vector sums, representing the subset of particles that lie within the acceptance of the ID and contribute to the track-based soft $E_{\mathrm{T}}^{\mathrm{miss}}$. The lepton vector sum is largely unchanged. However, a significant number of the hadronic recoil particles were not included, so the

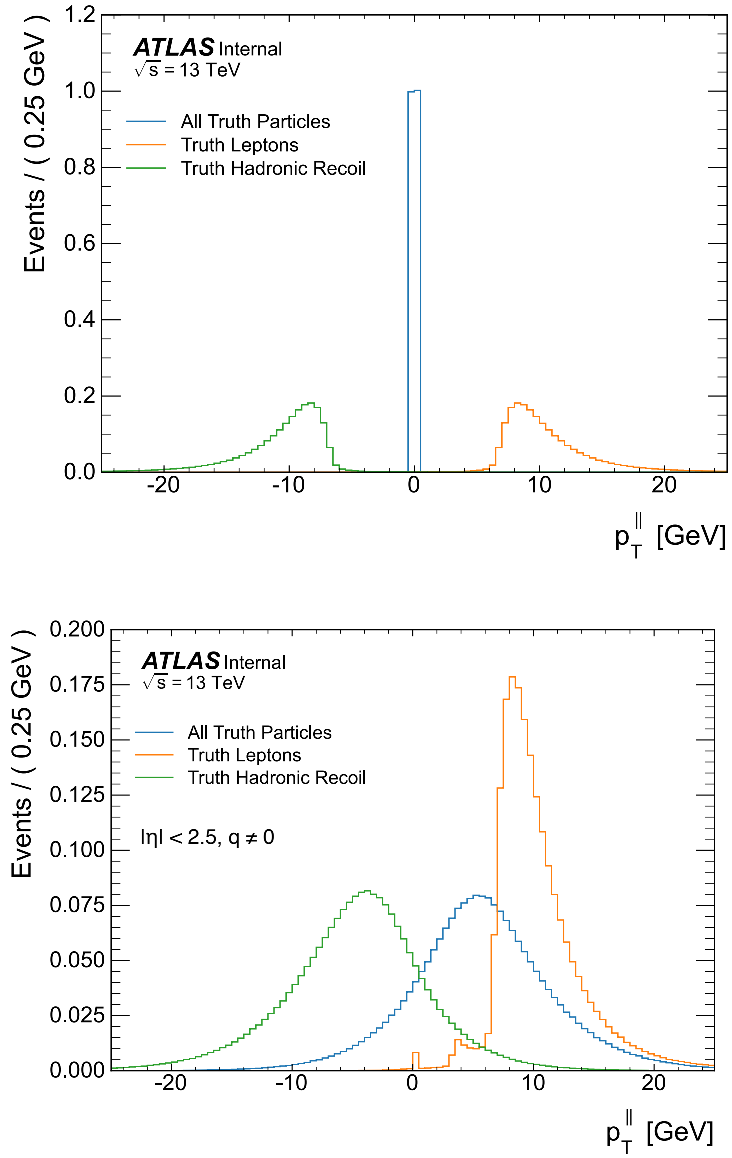

Figure 7.2: Vector sum of truth particle p_{T} in inclusive J/ψ production, projected onto the J/ψ momentum axis. On top, no selections have been applied. On the bottom, only particles with $|\eta| < 2.5$ and $q \neq 0$ are included. With those selections, a bias which peaks at 6 GeV in the direction of the J/ψ is observed.

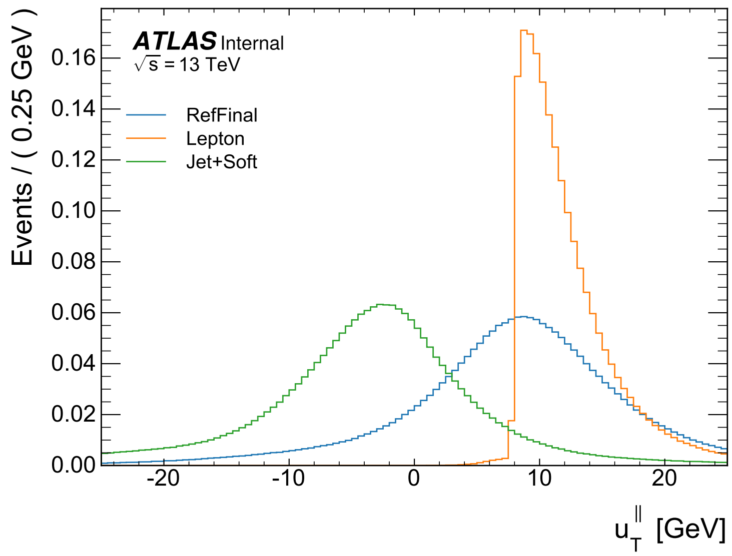

Figure 7.3: Negative of the reconstructed $E_{\mathrm{T}}^{\mathrm{miss}}$ vector, projected onto the J/ψ axis, in inclusive J/ψ production. The observed bias is consistent with excluding forward and neutral particles in the hadronic recoil.

recoil vector is biased towards the J/ψ. Consequently, the sum of all *trackable* particles in the event was biased in the direction of the J/ψ. The peak of this distribution, shown on the bottom half of Figure 7.2, is located around 8 GeV in the direction of the J/ψ.

7.3.2 Effects on Reconstructed $E_{\mathrm{T}}^{\mathrm{miss}}$

Finally, I repeated this procedure using the reconstructed $E_{\mathrm{T}}^{\mathrm{miss}}$ in the inclusive J/ψ sample. The two relevant terms are the muon term, which accounts for the J/ψ, and the soft track term, which accounts for the hadronic recoil. In Figure 7.3, I show the projections of these two terms, as well as the total missing energy, projected onto the J/ψ axis. (To be precise, I am showing

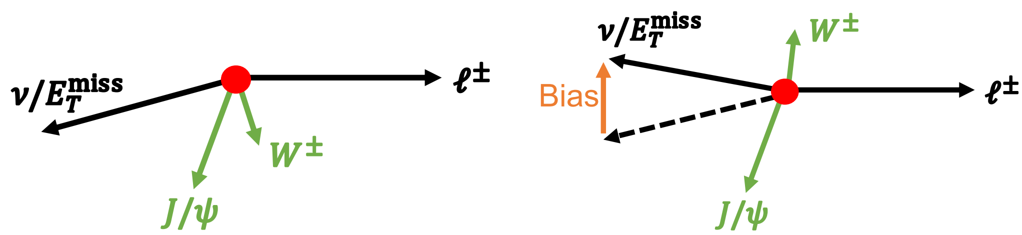

Figure 7.4: A schematic of the effects of a bias in the $E_{\mathrm{T}}^{\mathrm{miss}}$. Even a small bias opposite the direction of the J/ψ can vastly change the reconstructed value of $\Delta\varphi\left(J/\psi, W^{\pm}\right)$ for soft $W^{\pm}$ bosons.

projections of $-E_{\mathrm{T}}^{\mathrm{miss}}$ to make the comparison to Figure 7.2 more straightforward.) These distributions are directly analogous to the truth distribution in Figure 7.2 where the charge and rapidity cuts have been applied. By contrast, no bias is observed in the direction orthogonal to the J/ψ. Thus, from this simple generator-level model, I conclude that forward and neutral particles in the hadronic recoil are not included in the calculation of the $E_{\mathrm{T}}^{\mathrm{miss}}$, so the reconstructed $E_{\mathrm{T}}^{\mathrm{miss}}$ is biased opposite the direction of the J/ψ momentum. A bias of the same magnitude and direction is observed in associated production using both DPS and SPS MC samples.

7.3.3 Effects on $\Delta\varphi\left(J/\psi, W^{\pm}\right)$

A bias of a few GeV in the measurement of the $E_{\mathrm{T}}^{\mathrm{miss}}$ is often acceptable.[1] However, in this analysis, I use the $E_{\mathrm{T}}^{\mathrm{miss}}$ to reconstruct the momentum vector of a $W^{\pm}$ boson. For soft $W^{\pm}$ bosons, even a small mis-measurement

[1] Analyses which use a cut on $E_{\mathrm{T}}^{\mathrm{miss}}$ typically just lose some signal/background separation power. However, for other analyses like the $W^{\pm}$ mass measurement, a proper treatment of this bias is critical.

of the $p_{\mathrm{T}}^{W^\pm}$ vector can have a significant impact on the reconstructed φ of the $W^\pm$, and thus the measured value of $\Delta\varphi\,(J/\psi, W^\pm)$. A schematic of this effect is shown in Figure 7.4.

7.4 Other Angular Variables

The issues with accurately reconstructing the azimuthal direction of a soft $W^\pm$ boson can be avoided by utilizing angular other observables which do not rely on $E_{\mathrm{T}}^{\mathrm{miss}}$ information. I instead consider the rapidity and azimuthal separation between the J/ψ and the $W^\pm$ decay lepton, $\Delta y\,(J/\psi, \ell^\pm)$ and $\Delta\varphi\,(J/\psi, \ell^\pm)$. Specifically, I use the SPS and DPS simulation samples to produce two-dimensional templates in these variables, as shown in Figures 7.5 and 7.6. The SPS shapes are generated with `HelacOnia`. Then, using a maximum-likelihood fit, a weighted sum of these templates is fit to the two-dimensional distribution in data in each J/ψ bin. The results of these fits, projected onto the two axes, are shown in Figures 7.7 and 7.8. The likelihood function of each fit is shown in Figure 7.9. Additionally, the resulting fractional yields from each fit are shown in Figure 7.10.

The resulting yields from the fits have large statistical uncertainties. Thus, in many bins, it is not possible to definitively conclude what fraction of the data is DPS and SPS production. In the forward rapidity bins, the data are consistent with a DPS-dominated production at low-p_{T}, and a color-octet-SPS-dominated production at high-p_{T}. In the central rapidity bins, the fits to the data are less conclusive. At low-p_{T}, the data are consistent with a

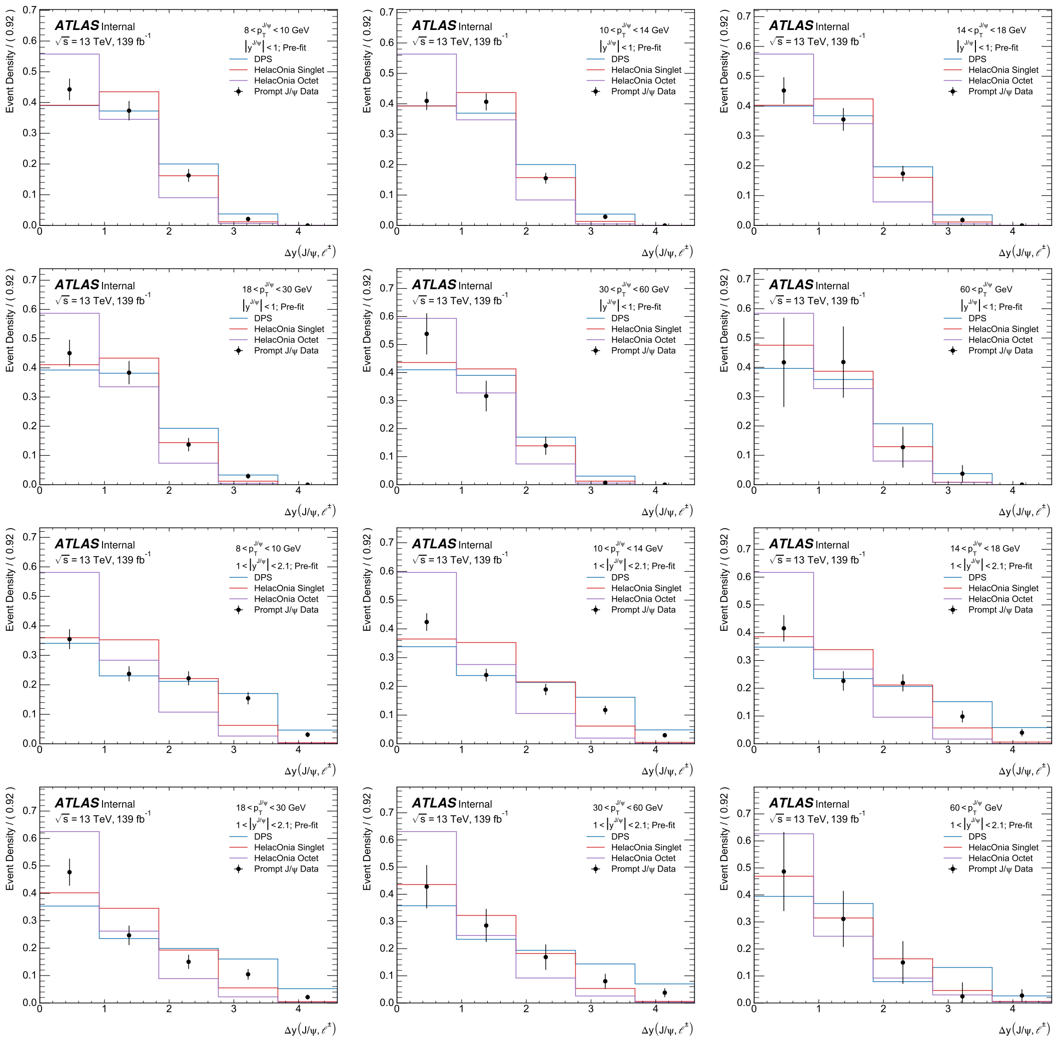

Figure 7.5: MC samples are used to produce templates of the variable $\Delta y\,(J/\psi, \ell^{\pm})$ for SPS and DPS. The templates for data and MC are shown in each analysis bin.

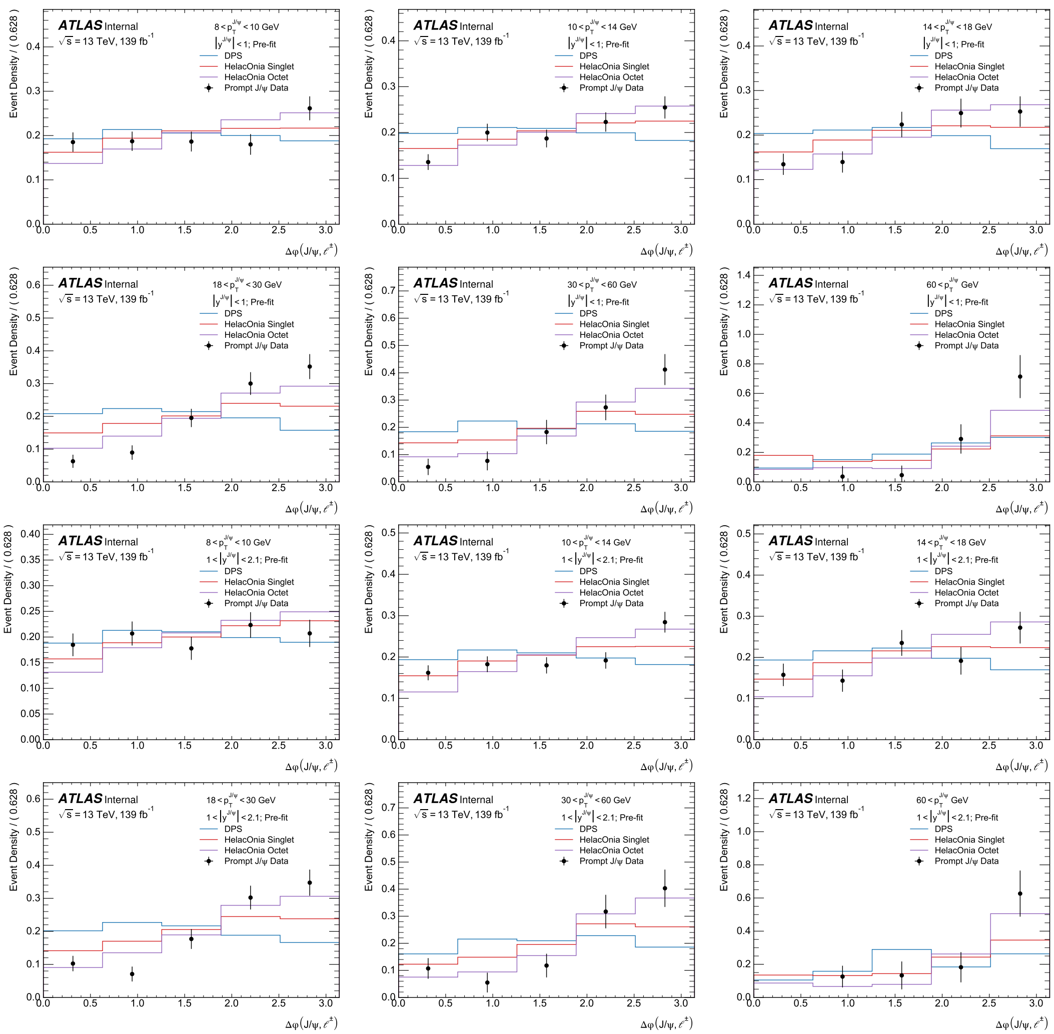

Figure 7.6: MC samples are used to produce templates of the variable $\Delta\varphi\,(J/\psi, \ell^{\pm})$ for SPS and DPS. The templates for data and MC are shown in each analysis bin.

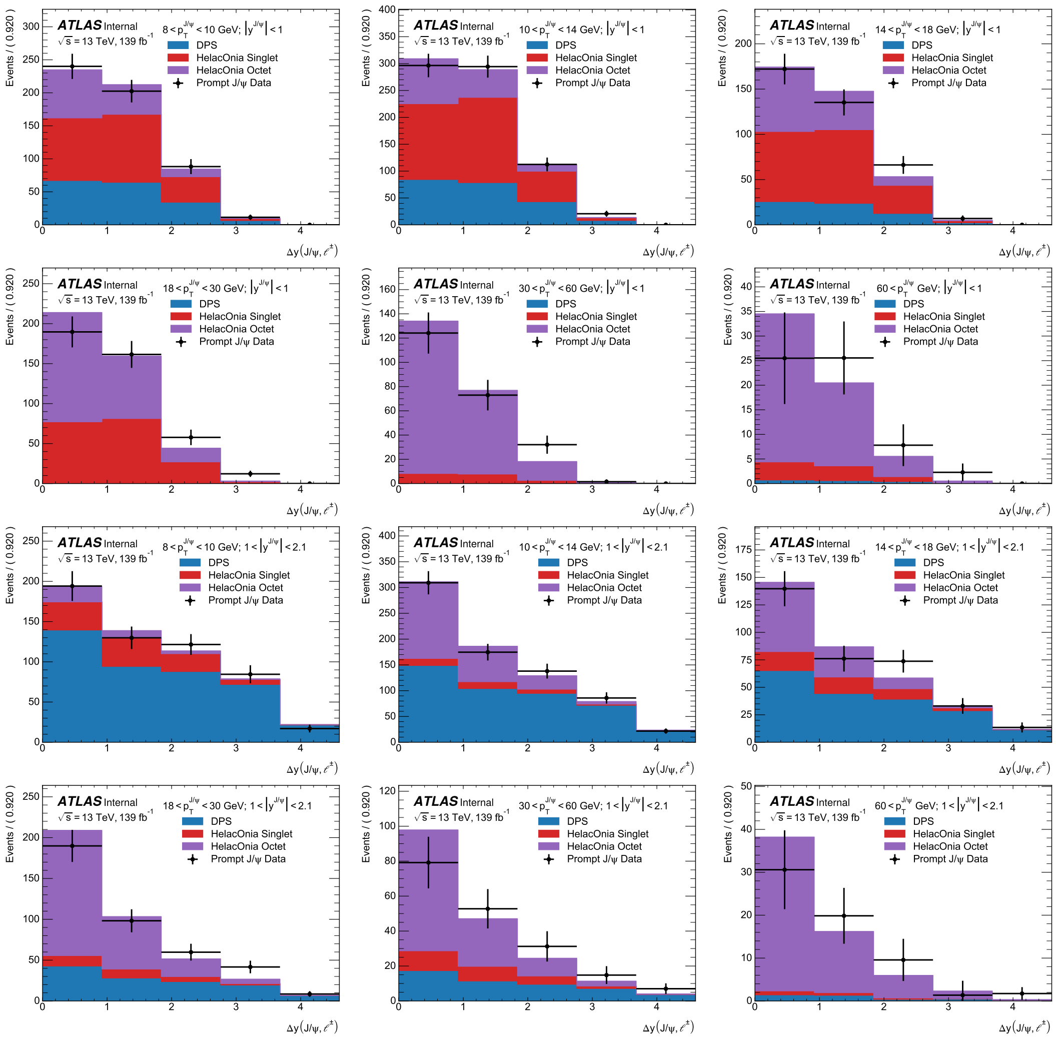

Figure 7.7: MC samples are used to produce two-dimensional templates of the variables $\Delta y\,(J/\psi, \ell^{\pm})$ and $\Delta\varphi\,(J/\psi, \ell^{\pm})$ for DPS and SPS. The distribution in data is fit to a weighted sum of the templates. The projection onto the $\Delta y\,(J/\psi, \ell^{\pm})$ axis is shown here.

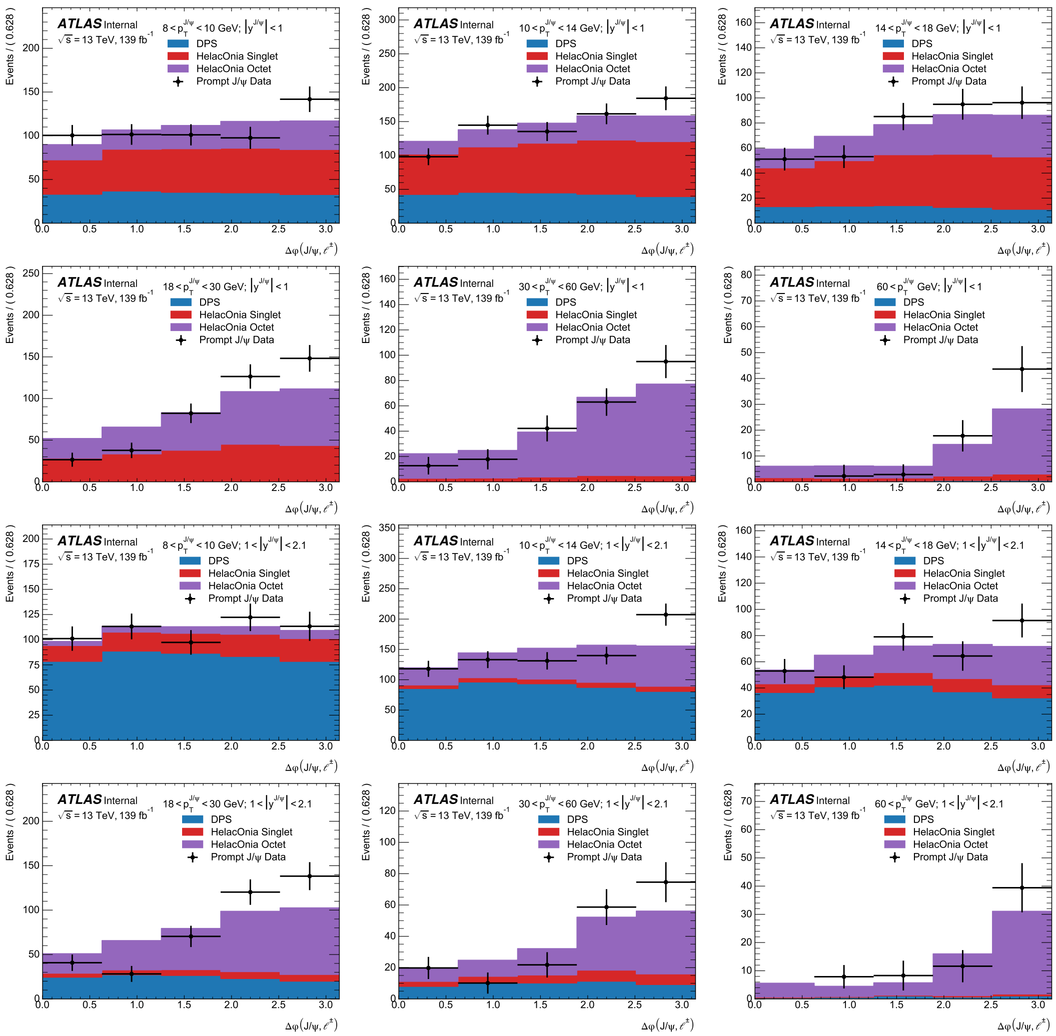

Figure 7.8: MC samples are used to produce two-dimensional templates of the variables $\Delta y\,(J/\psi, \ell^{\pm})$ and $\Delta\varphi\,(J/\psi, \ell^{\pm})$ for DPS and SPS. The distribution in data is fit to a weighted sum of the templates. The projection onto the $\Delta\varphi\,(J/\psi, \ell^{\pm})$ axis is shown here.

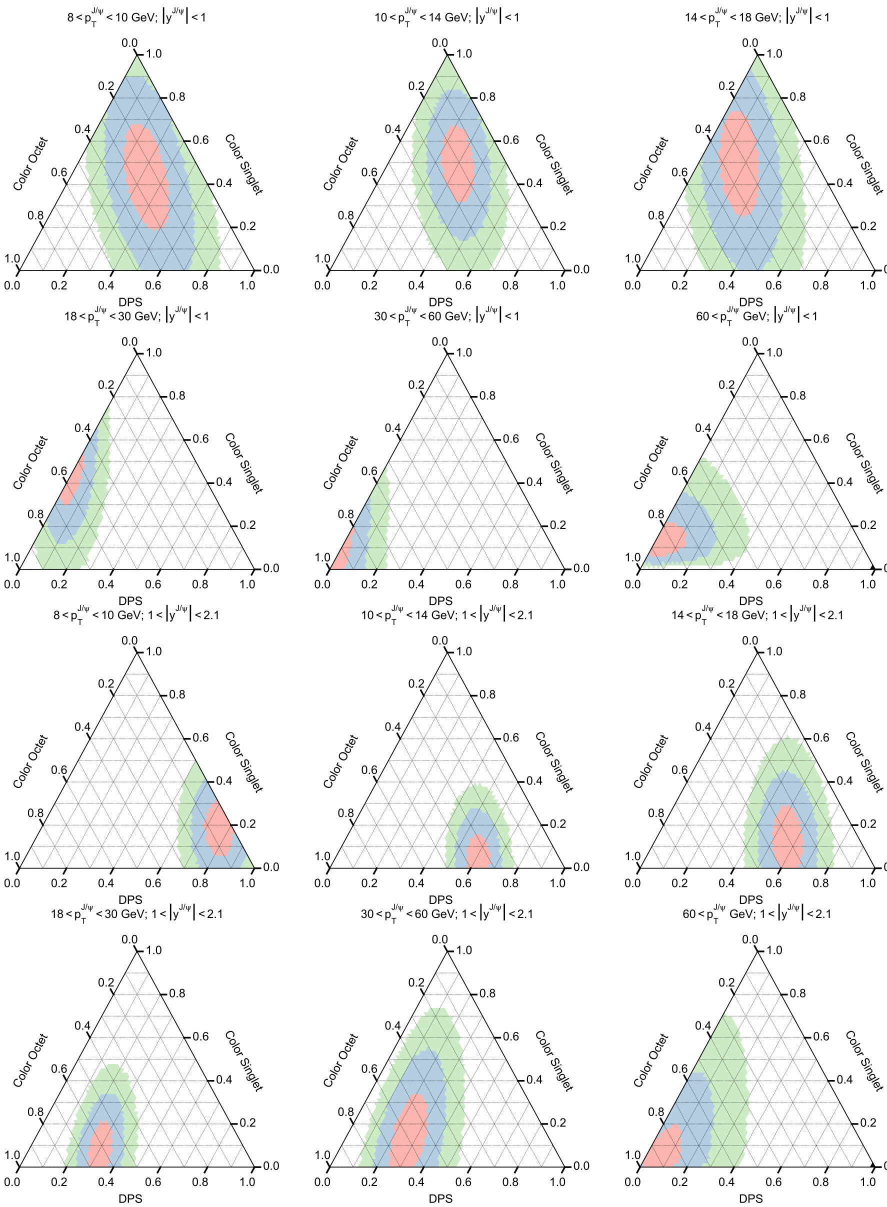

Figure 7.9: MC samples are used to produce two-dimensional templates of the variables $\Delta y\,(J/\psi, \ell^{\pm})$ and $\Delta\varphi\,(J/\psi, \ell^{\pm})$ for DPS and SPS. The distribution in data is fit to a weighted sum of the templates. For the three fitted yield parameters, 1σ, 2σ, and 3σ confidence intervals are shown.

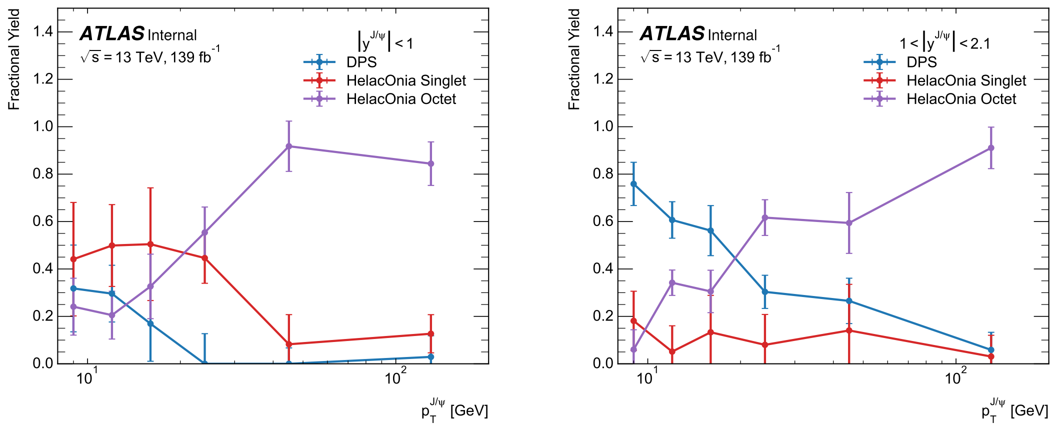

Figure 7.10: MC samples are used to produce two-dimensional templates of the variables $\Delta y\,(J/\psi, \ell^{\pm})$ and $\Delta\varphi\,(J/\psi, \ell^{\pm})$ for DPS and SPS. The distribution in data is fit to a weighted sum of the templates. The fractional yields are shown here.

wide variety of possible production modes. (In the $8 < p_{\mathrm{T}}^{J/\psi} < 10$ GeV and $\left|y^{J/\psi}\right| < 1$ bin, the data are 2σ-compatible with a 0% and 70% DPS fraction.) At high-p_{T}, the color-octet-SPS mode is preferred.

Chapter 8

Systematic Uncertainties

8.1 Prompt J/ψ Model

The choice of functions and fit procedure used to extract the prompt J/ψ component from the set of di-muon candidates is a source of systematic uncertainty. The first set of uncertainties comes from the use of a large inclusive J/ψ sample to fix some model parameters in the fit to the associated $J/\psi + W^{\pm}$ data. To estimate this uncertainty, I allow one of the nominally-fixed parameters to float and redo the associated fits. For example, I use the total J/ψ data to fix all parameters of the model except the component yields and the width of the τ resolution function, and record the variation of the measured yields. Then, I repeat the process for every other model parameter.

Another source of uncertainty relating to the prompt J/ψ extraction is the exact component functions used in the fit. Alternate choices of models were tried for each component, and the differences in yields from the nominal model were used as a systematic uncertainty. For the invariant mass model, I exchanged the signal model function from a double-Gaussian to a Crystal Ball + Gaussian, the linear background mass model for a quadratic polynomial, the τ double-Gaussian resolution function for a triple-Gaussian. Again I combine the variations in the estimated prompt J/ψ yield from these alternate functions in quadrature.

8.2 Lepton Background Estimations

In Chapter 6, I described the procedure used to estimate the presence of non-$W^{\pm}$ backgrounds from the associated $J/\psi + W^{\pm}$ and inclusive $W^{\pm}$ datasets. In both cases, the MC templates used in the fits to data are a source of systematic uncertainty. To estimate these systematic uncertainties, I use alternate templates and redo the fits to the data.

To estimate the systematic uncertainty of the QCD multi-jet background estimation, I use validation region C to constrain the QCD multi-jet template. I assume that all the observed excess events in data in that region are QCD multi-jet events, and use that normalization of the template to determine the number of QCD multi-jet events in the signal region A. The results of this variation are shown in Figure 8.1. The corresponding variation in the resulting signal fraction of region A is used as a systematic uncertainty.

There are numerous modeling uncertainties which exist for the Z+jets template. However, these modeling uncertainties should affect the template shape primarily due to their effect on the Z boson p_{T} distribution. That is, changing the p_{T} spectrum affects the acceptance for losing a lepton. Therefore, I fold all the Z-modeling systematic uncertainties into one by manually adjusting the p_T^Z spectrum in the MC sample. To do this, I re-weight the events according to the function $w = 1 + \frac{p_T^Z}{2000}$, effectively altering the p_{T}^Z dis-

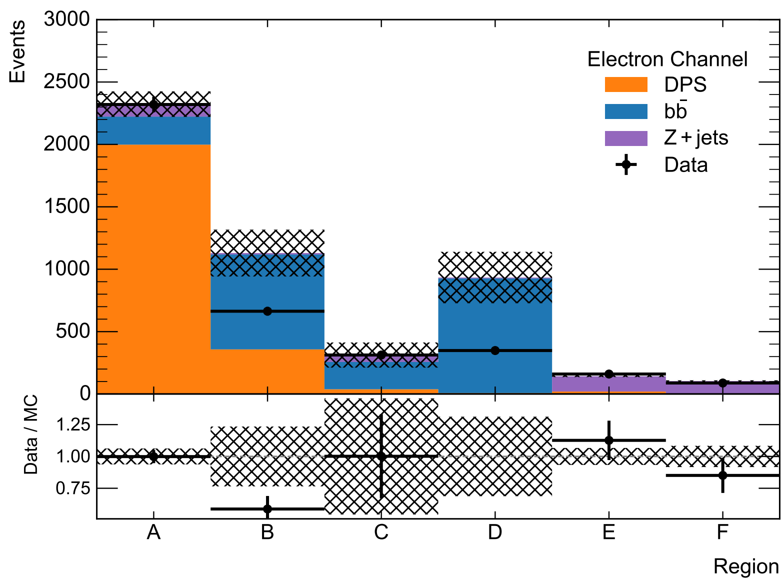

Figure 8.1: The systematic uncertainty originating from the QCD multi-jet MC template is estimated by scaling up the template normalization to match the data in validation region C, as seen here.

tribution. The templates generated from the re-weighted sample are fit to the data, and the variation on the signal fraction is used to estimate the systematic uncertainty associated with the Z+jets template.

8.3 Inclusive $W^{\pm}$ Backgrounds

The systematic uncertainties associated with the fit follow the method used to estimate the lepton backgrounds in the associated $J/\psi+W^{\pm}$ data. For the QCD template, I suppose that the difference in events in region C (isolated leptons with low $E_{\mathrm{T}}^{\mathrm{miss}}$ and $M_T\left(W^{\pm}\right)$) are QCD multi-jet events, and scale the QCD fraction in region A accordingly. Overall, I found that the uncertainties associated with the inclusive $W^{\pm}$ measurement are very small in comparison to other uncertainties in the analysis.

8.4 $W^{\pm}$ Acceptance and Efficiency

The act of taking the ratio $\sigma\left(J/\psi+W^{\pm}\right)/\sigma\left(W^{\pm}\right)$ causes most of the uncertainties relating to the $W^{\pm}$ acceptance and efficiency to cancel out. Similarly, the uncertainties relating to the integrated luminosity cancel. Using simulated DPS $J/\psi+W^{\pm}$ events, I calculated the $W^{\pm}$ acceptance as a function of $W^{\pm}$ transverse momentum, and find at most a 10% difference in acceptance throughout the range $p_{\mathrm{T}}^{W^{\pm}}<200\,\mathrm{GeV}$, as seen in Figure 8.2. Therefore, I use this upper bound as a maximum variation of the uncertainty associated with the cancellation of the $W^{\pm}$ acceptance in the numerator and denominator of the cross-section ratio.

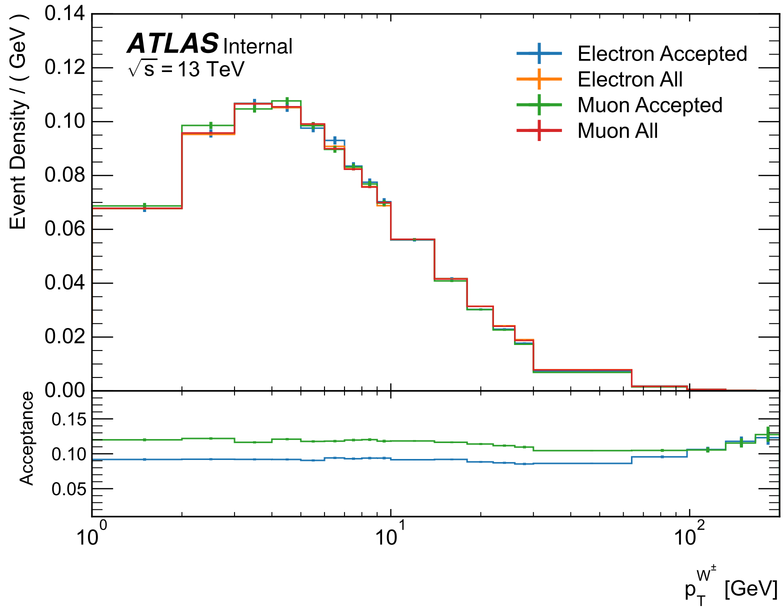

Figure 8.2: The systematic uncertainty originating from cancellation of the $W^{\pm}$ acceptance is estimated using a DPS MC sample. The ratio of selected to generated events is shown as a function of $p_{\mathrm{T}}^{W^{\pm}}$.

8.5 Muon Reconstruction Efficiency

The muon efficiency calculations have an accompanying systematic uncertainty. The prompt $J/\psi + W^{\pm}$ events are re-weighted using the systematic variation maps.

8.6 J/ψ Spin Alignment

A nominal uniform J/ψ spin-alignment profile is used to correct for acceptance effects of the J/ψ. However, six other spin-alignment scenarios are considered, following the procedure adopted and described in §6.1.2. Events are re-weighted according to these alternate acceptance maps. The maximal variation of the predicted yields is used as the systematic uncertainty associated with J/ψ spin alignment. This uncertainty is recorded separately from all other systematic uncertainties, which are added in quadrature.

8.7 Summary and Ranking

A complete table of systematic uncertainties is presented in Table 8.1. The contribution of each uncertainty to the cross-section ratio R are shown in Figures 8.3 and 8.4.

Table 8.1: List of systematic uncertainties considered in the analysis.

Group	**Systematic**
Fit model (fixed parameters)	Floating σ_m parameter
	Floating f_m parameter
	Floating prompt combinatorial slope
	Floating λ_S parameter
	Floating non-prompt combinatorial slopes
	Floating λ_{C1} parameter
	Floating λ_{C2} parameter
	Floating σ_τ parameter
	Floating f_R parameter
Fit model (function choice)	Signal mass function
	Background mass function (prompt)
	Background mass function (non-prompt 1)
	Background mass function (non-prompt 2)
	τ resolution function
Associated J/ψ+$W^\pm$ yield	Muon reconstruction efficiency
Associated J/ψ+$W^\pm$ backgrounds	QCD template shape
	QCD template statistics
	Prompt $J/\psi + Z$ template shape
	Prompt $J/\psi + Z$ template statistics
Inclusive $W^\pm$ backgrounds	QCD template shape
	QCD template statistics
$W^\pm$ acceptance	Cancellation of $W^\pm$ efficiency and acceptance
J/ψ spin-alignment	J/ψ acceptance dependence on polarization

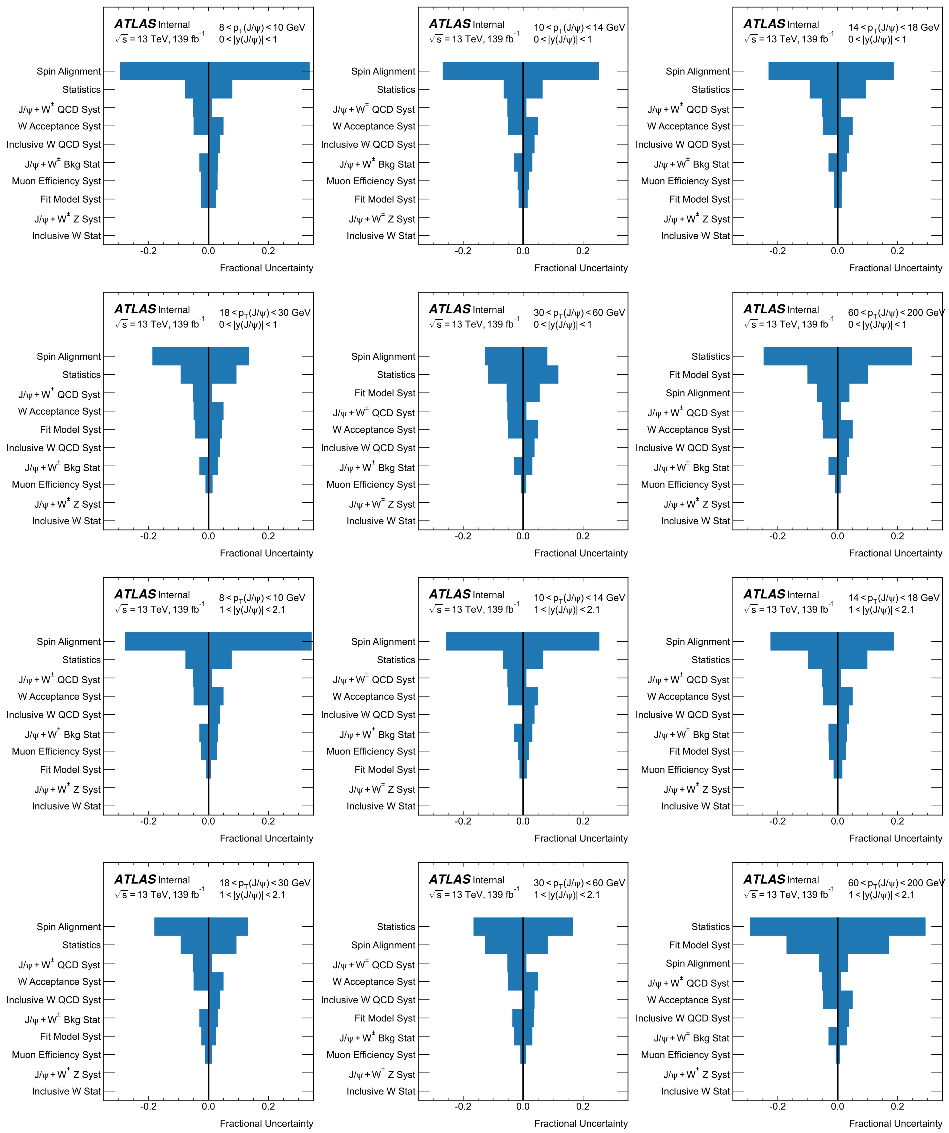

Figure 8.3: Ranking of systematic and statistical uncertainties in the electron channel.

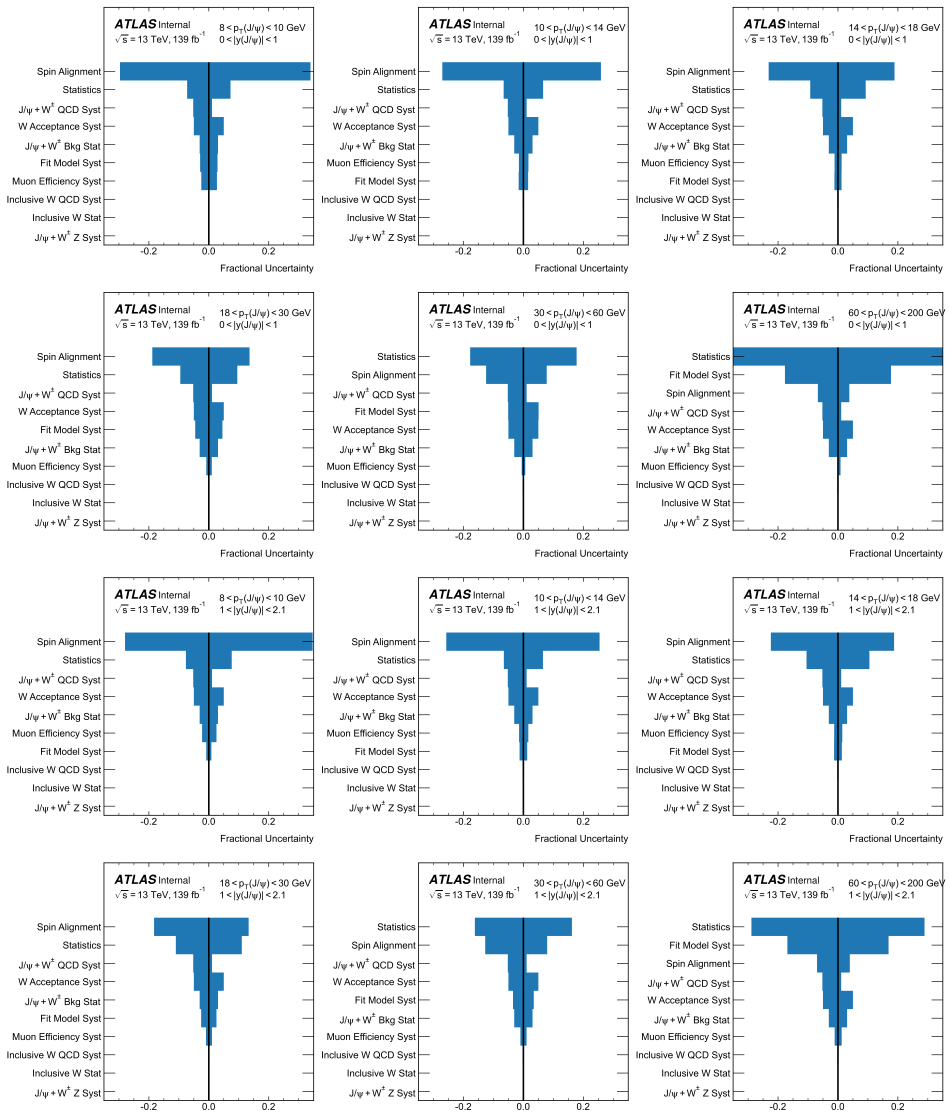

Figure 8.4: Ranking of systematic and statistical uncertainties in the muon channel.

Chapter 9

Results and Conclusions

The double-differential cross-section ratio measurements are presented in Figure 9.1 for the electron channel and Figure 9.2 for the muon channel. The points correspond to the central values, the shaded regions correspond to the spin-alignment systematic uncertainty, and the error bars correspond to the combination of the statistical and all other systematic uncertainties.

In Chapter 7, I discussed how angular distributions might be used to separate the SPS and DPS components experimentally. At the same time, the models of SPS and DPS make predictions about the $p_{\mathrm{T}}^{J/\psi}$ spectrum. Using the ansatz of Eq. 1.7, I compare the measured cross-section ratio to the DPS prediction. The value of $\sigma_{\mathrm{eff}} = 9.2\,\mathrm{mb}$ is chosen so that the lowest $p_{\mathrm{T}}^{J/\psi}$ bin is saturated with DPS. I find that the DPS distribution does not match that of data; this suggests that the SPS production mode is dominant at high-$p_{\mathrm{T}}^{J/\psi}$.

In summary, the production of heavy quarkonia associated with a vector boson can be used to probe models of QCD near the perterbative/non-perturbative boundary. The cross-section ratio of $J/\psi + W^{\pm}$ to $W^{\pm}$ production has been measured using the 13 TeV ATLAS Run 2 dataset, and data have been compared to multiple models of DPS and SPS production.

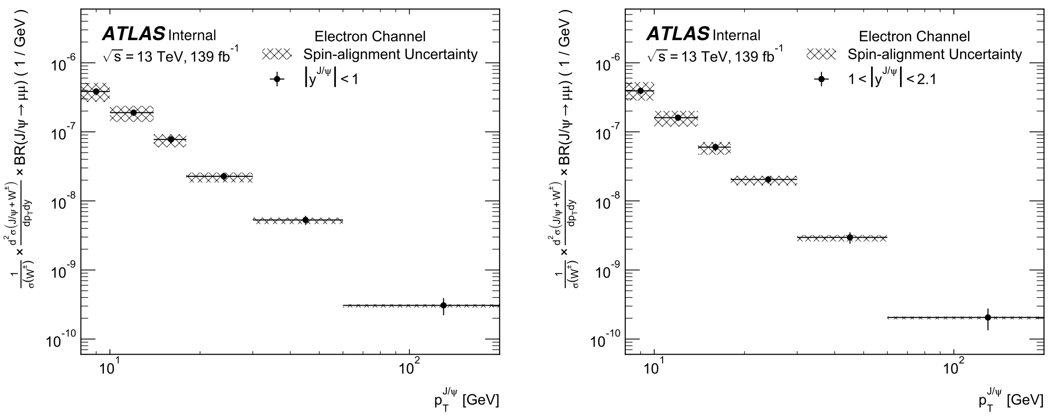

Figure 9.1: Measured ratio of the associated $J/\psi + W^{\pm}$ production cross-section to the inclusive $W^{\pm}$ production cross-section in the electron channel. Error bars on the data show the combination of statistical and systematic uncertainties. Shaded regions show the uncertainty due to the unknown spin alignment profile of the J/ψ.

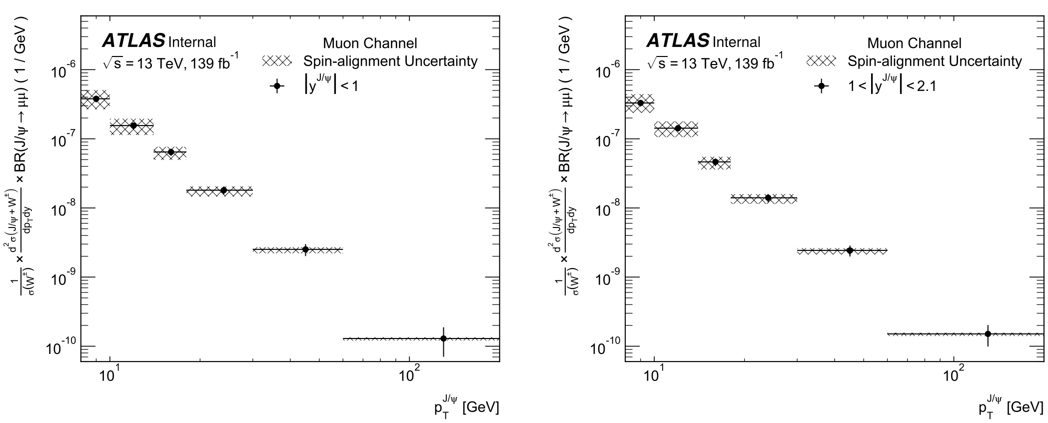

Figure 9.2: Measured ratio of the associated $J/\psi + W^{\pm}$ production cross-section to the inclusive $W^{\pm}$ production cross-section in the electron channel. Error bars on the data show the combination of statistical and systematic uncertainties. Shaded regions show the uncertainty due to the unknown spin alignment profile of the J/ψ.

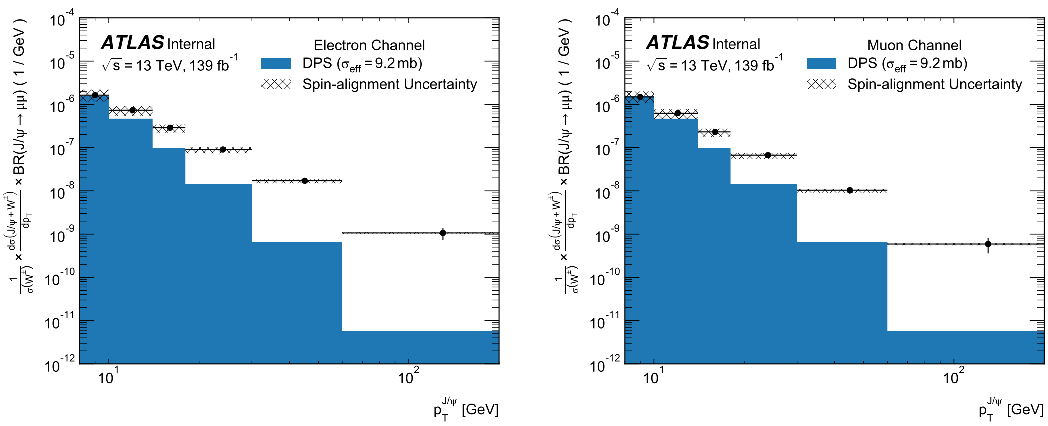

Figure 9.3: The measured cross-section ratio is compared to a model of double-parton scattering. The value of $\sigma_{\text{eff}} = 9.2\,\text{mb}$ is chosen so that the lowest $p_{\text{T}}^{J/\psi}$ bin is saturated with DPS. The $p_{\text{T}}^{J/\psi}$ distribution from DPS does not agree with data in all bins, suggesting the presence of an SPS contribution.

Appendices

Appendix A

Data Tables

The background estimates for the lepton backgrounds—QCD multi-jet and prompt $J/\psi + Z$ events—in the associated $J/\psi + W^{\pm}$ sample are listed for each bin in Tables A.1–A.4.

In Tables A.5 and A.6, the measured cross-section ratio values are presented. The statistical, spin-alignment, and the combination of all other systematic uncertainties are listed for each bin.

Table A.1: QCD multi-jet background estimates for the electron channel. Backgrounds are estimated by fitting the data in each p_{T}/y bin to a sum of DPS, $b\bar{b}$, and Z templates.

Bin $\lvert y\rvert \times p_{\mathrm{T}}$ (GeV)	QCD multi-jet Fraction
$(0,1) \times (8,10)$	0.023 ± 0.005 (stat) $\pm$ 0.023 (syst)
$(1,2.1) \times (8,10)$	0.022 ± 0.004 (stat) $\pm$ 0.022 (syst)
$(0,1) \times (10,14)$	0.024 ± 0.004 (stat) $\pm$ 0.024 (syst)
$(1,2.1) \times (10,14)$	0.028 ± 0.004 (stat) $\pm$ 0.028 (syst)
$(0,1) \times (14,18)$	0.028 ± 0.005 (stat) $\pm$ 0.028 (syst)
$(1,2.1) \times (14,18)$	0.045 ± 0.007 (stat) $\pm$ 0.045 (syst)
$(0,1) \times (18,30)$	0.045 ± 0.007 (stat) $\pm$ 0.045 (syst)
$(1,2.1) \times (18,30)$	0.035 ± 0.006 (stat) $\pm$ 0.035 (syst)
$(0,1) \times (30,200)$	0.041 ± 0.008 (stat) $\pm$ 0.041 (syst)
$(1,2.1) \times (30,200)$	0.068 ± 0.010 (stat) $\pm$ 0.068 (syst)

Table A.2: Prompt $J/\psi + Z$ background estimates for the electron channel. Backgrounds are estimated by fitting the data in each p_{T}/y bin to a sum of DPS, $b\bar{b}$, and Z templates.

Bin $\lvert y\rvert \times p_{\mathrm{T}}$ (GeV)	Prompt $J/\psi + Z$ Fraction
$(0,1) \times (8,10)$	0.061 ± 0.011 (stat) $\pm$ 0.001 (syst)
$(1,2.1) \times (8,10)$	0.053 ± 0.010 (stat) $\pm$ 0.001 (syst)
$(0,1) \times (10,14)$	0.063 ± 0.009 (stat) $\pm$ 0.001 (syst)
$(1,2.1) \times (10,14)$	0.050 ± 0.008 (stat) $\pm$ 0.001 (syst)
$(0,1) \times (14,18)$	0.038 ± 0.010 (stat) $\pm$ 0.000 (syst)
$(1,2.1) \times (14,18)$	0.047 ± 0.012 (stat) $\pm$ 0.001 (syst)
$(0,1) \times (18,30)$	0.095 ± 0.015 (stat) $\pm$ 0.001 (syst)
$(1,2.1) \times (18,30)$	0.077 ± 0.014 (stat) $\pm$ 0.001 (syst)
$(0,1) \times (30,200)$	0.095 ± 0.018 (stat) $\pm$ 0.001 (syst)
$(1,2.1) \times (30,200)$	0.052 ± 0.016 (stat) $\pm$ 0.001 (syst)

Table A.3: QCD multi-jet background estimates for the muon channel. Backgrounds are estimated by fitting the data in each p_{T}/y bin to a sum of DPS, $b\bar{b}$, and Z templates.

Bin $\|y\| \times p_{\mathrm{T}}$ (GeV)	QCD multi-jet Fraction
$(0,1) \times (8,10)$	0.019 ± 0.003 (stat) $\pm$ 0.019 (syst)
$(1,2.1) \times (8,10)$	0.019 ± 0.003 (stat) $\pm$ 0.019 (syst)
$(0,1) \times (10,14)$	0.020 ± 0.003 (stat) $\pm$ 0.020 (syst)
$(1,2.1) \times (10,14)$	0.023 ± 0.003 (stat) $\pm$ 0.023 (syst)
$(0,1) \times (14,18)$	0.022 ± 0.004 (stat) $\pm$ 0.022 (syst)
$(1,2.1) \times (14,18)$	0.034 ± 0.005 (stat) $\pm$ 0.034 (syst)
$(0,1) \times (18,30)$	0.038 ± 0.005 (stat) $\pm$ 0.038 (syst)
$(1,2.1) \times (18,30)$	0.029 ± 0.004 (stat) $\pm$ 0.029 (syst)
$(0,1) \times (30,200)$	0.032 ± 0.005 (stat) $\pm$ 0.032 (syst)
$(1,2.1) \times (30,200)$	0.049 ± 0.007 (stat) $\pm$ 0.049 (syst)

Table A.4: Prompt $J/\psi + Z$ background estimates for the muon channel. Backgrounds are estimated by fitting the data in each p_{T}/y bin to a sum of DPS, $b\bar{b}$, and Z templates.

Bin $\|y\| \times p_{\mathrm{T}}$ (GeV)	Prompt $J/\psi + Z$ Fraction
$(0,1) \times (8,10)$	0.045 ± 0.008 (stat) $\pm$ 0.000 (syst)
$(1,2.1) \times (8,10)$	0.040 ± 0.008 (stat) $\pm$ 0.000 (syst)
$(0,1) \times (10,14)$	0.046 ± 0.007 (stat) $\pm$ 0.000 (syst)
$(1,2.1) \times (10,14)$	0.038 ± 0.006 (stat) $\pm$ 0.000 (syst)
$(0,1) \times (14,18)$	0.030 ± 0.008 (stat) $\pm$ 0.000 (syst)
$(1,2.1) \times (14,18)$	0.037 ± 0.009 (stat) $\pm$ 0.000 (syst)
$(0,1) \times (18,30)$	0.070 ± 0.012 (stat) $\pm$ 0.000 (syst)
$(1,2.1) \times (18,30)$	0.057 ± 0.011 (stat) $\pm$ 0.000 (syst)
$(0,1) \times (30,200)$	0.069 ± 0.014 (stat) $\pm$ 0.000 (syst)
$(1,2.1) \times (30,200)$	0.038 ± 0.012 (stat) $\pm$ 0.000 (syst)

Table A.5: Measured ratio of the associated J/ψ+$W^{\pm}$ production cross-section to the inclusive $W^{\pm}$ production cross-section in the electron channel. Values are reported differentially in J/ψ transverse momentum and rapidity.

Bin $\|y\| \times p_{\mathrm{T}}$ (GeV)	Differential Cross-section Ratio ($\times 10^{-7}$/GeV)
$(0,1) \times (8,10)$	3.844 ± 0.305 (stat) ± 0.333 (syst) ± 1.297 (spin)
$(1,2.1) \times (8,10)$	3.926 ± 0.303 (stat) ± 0.326 (syst) ± 1.351 (spin)
$(0,1) \times (10,14)$	1.900 ± 0.123 (stat) ± 0.156 (syst) ± 0.482 (spin)
$(1,2.1) \times (10,14)$	1.606 ± 0.108 (stat) ± 0.131 (syst) ± 0.409 (spin)
$(0,1) \times (14,18)$	0.776 ± 0.073 (stat) ± 0.063 (syst) ± 0.146 (spin)
$(1,2.1) \times (14,18)$	0.601 ± 0.059 (stat) ± 0.051 (syst) ± 0.113 (spin)
$(0,1) \times (18,30)$	0.227 ± 0.021 (stat) ± 0.021 (syst) ± 0.030 (spin)
$(1,2.1) \times (18,30)$	0.204 ± 0.019 (stat) ± 0.017 (syst) ± 0.027 (spin)
$(0,1) \times (30,60)$	0.053 ± 0.006 (stat) ± 0.005 (syst) ± 0.004 (spin)
$(1,2.1) \times (30,60)$	0.030 ± 0.005 (stat) ± 0.003 (syst) ± 0.002 (spin)
$(0,1) \times (60,200)$	0.003 ± 0.001 (stat) ± 0.000 (syst) ± 0.000 (spin)
$(1,2.1) \times (60,200)$	0.002 ± 0.001 (stat) ± 0.000 (syst) ± 0.000 (spin)

Table A.6: Measured ratio of the associated J/ψ+$W^{\pm}$ production cross-section to the inclusive $W^{\pm}$ production cross-section in the muon channel. Values are reported differentially in J/ψ transverse momentum and rapidity.

Bin $\|y\| \times p_{\mathrm{T}}$ (GeV)	Differential Cross-section Ratio ($\times 10^{-7}$/GeV)
$(0,1) \times (8,10)$	3.793 ± 0.275 (stat) ± 0.331 (syst) ± 1.287 (spin)
$(1,2.1) \times (8,10)$	3.299 ± 0.252 (stat) ± 0.270 (syst) ± 1.143 (spin)
$(0,1) \times (10,14)$	1.554 ± 0.102 (stat) ± 0.126 (syst) ± 0.402 (spin)
$(1,2.1) \times (10,14)$	1.424 ± 0.093 (stat) ± 0.115 (syst) ± 0.362 (spin)
$(0,1) \times (14,18)$	0.645 ± 0.060 (stat) ± 0.052 (syst) ± 0.122 (spin)
$(1,2.1) \times (14,18)$	0.464 ± 0.049 (stat) ± 0.037 (syst) ± 0.087 (spin)
$(0,1) \times (18,30)$	0.181 ± 0.017 (stat) ± 0.016 (syst) ± 0.025 (spin)
$(1,2.1) \times (18,30)$	0.140 ± 0.015 (stat) ± 0.012 (syst) ± 0.019 (spin)
$(0,1) \times (30,60)$	0.025 ± 0.004 (stat) ± 0.002 (syst) ± 0.002 (spin)
$(1,2.1) \times (30,60)$	0.024 ± 0.004 (stat) ± 0.002 (syst) ± 0.002 (spin)
$(0,1) \times (60,200)$	0.001 ± 0.001 (stat) ± 0.000 (syst) ± 0.000 (spin)
$(1,2.1) \times (60,200)$	0.002 ± 0.000 (stat) ± 0.000 (syst) ± 0.000 (spin)

Bibliography

[1] Steven Weinberg. “A Model of Leptons”. In: *Phys. Rev. Lett.* 19 (21 Nov. 1967), pp. 1264–1266. DOI: 10.1103/PhysRevLett.19.1264.

[2] Sheldon L. Glashow. “Partial-symmetries of weak interactions”. In: *Nuclear Physics* 22.4 (1961), pp. 579–588. DOI: 10.1016/0029-5582(61)90469-2.

[3] Abdus Salam. “Weak and Electromagnetic Interactions”. In: *Conf. Proc. C* 680519 (1968), pp. 367–377. DOI: 10.1142/9789812795915_0034.

[4] Michael E. Peskin and Daniel V. Schroeder. *An Introduction to quantum field theory*. Reading, USA: Addison-Wesley, 1995.

[5] Matthew D. Schwartz. *Quantum Field Theory and the Standard Model*. Chapter 16.3. Cambridge University Press, Mar. 2014.

[6] John C. Collins, Davison E. Soper, and George Sterman. “FACTORIZATION OF HARD PROCESSES IN QCD”. In: *Perturbative QCD*, pp. 1–91. DOI: 10.1142/9789814503266_0001.

[7] P.A. Zyla et al. “Review of Particle Physics”. In: *PTEP* 2020.8 (2020). and 2021 update, p. 083C01. DOI: 10.1093/ptep/ptaa104.

[8] Richard D. Ball et al. “Parton distribution benchmarking with LHC data”. In: *Journal of High Energy Physics* 2013.4 (2013), p. 125. DOI: 10.1007/JHEP04(2013)125.

[9] Jun Gao, Lucian Harland-Lang, and Juan Rojo. “The structure of the proton in the LHC precision era”. In: *Physics Reports* 742 (2018). The Structure of the Proton in the LHC Precision Era, pp. 1–121. DOI: https://doi.org/10.1016/j.physrep.2018.03.002.

[10] Johannes Blümlein. “The theory of deeply inelastic scattering”. In: *Progress in Particle and Nuclear Physics* 69 (2013), pp. 28–84. DOI: https://doi.org/10.1016/j.ppnp.2012.09.006.

[11] A. De Roeck and R.S. Thorne. “Structure functions”. In: *Progress in Particle and Nuclear Physics* 66.4 (2011), pp. 727–781. DOI: https://doi.org/10.1016/j.ppnp.2011.06.001.

[12] E Perez and E Rizvi. “The quark and gluon structure of the proton”. In: *Reports on Progress in Physics* 76.4 (Mar. 2013), p. 046201. DOI: 10.1088/0034-4885/76/4/046201.

[13] Stefano Forte and Graeme Watt. "Progress in the Determination of the Partonic Structure of the Proton". In: *Annual Review of Nuclear and Particle Science* 63.1 (2013), pp. 291–328. DOI: 10.1146/annurev-nucl-102212-170607.

[14] Jacob J. Ethier and Emanuele R. Nocera. "Parton Distributions in Nucleons and Nuclei". In: *Annual Review of Nuclear and Particle Science* 70.1 (2020), pp. 43–76. DOI: 10.1146/annurev-nucl-011720-042725.

[15] Tie-Jiun Hou et al. "New CTEQ global analysis of quantum chromodynamics with high-precision data from the LHC". In: *Phys. Rev. D* 103 (1 Jan. 2021), p. 014013. DOI: 10.1103/PhysRevD.103.014013.

[16] S. Alekhin et al. "Parton distribution functions, α_s, and heavy-quark masses for LHC Run II". In: *Phys. Rev. D* 96 (1 July 2017), p. 014011. DOI: 10.1103/PhysRevD.96.014011.

[17] S. Bailey et al. "Parton distributions from LHC, HERA, Tevatron and fixed target data: MSHT20 PDFs". In: *The European Physical Journal C* 81.4 (2021), p. 341. DOI: 10.1140/epjc/s10052-021-09057-0.

[18] Richard D. Ball, Valerio Bertone, Stefano Carrazza, et al. "Parton distributions from high-precision collider data". In: *The European Physical Journal C* 77.10 (2017), p. 663. DOI: 10.1140/epjc/s10052-017-5199-5.

[19] H. Abramowicz et al. "Combination of measurements of inclusive deep inelastic $e^{\pm}p$ scattering cross sections and QCD analysis of HERA data". In: *The European Physical Journal C* 75.12 (2015), p. 580. DOI: 10.1140/epjc/s10052-015-3710-4.

[20] R. P. Feynman. "Space-Time Approach to Quantum Electrodynamics". In: *Phys. Rev.* 76 (6 Sept. 1949), pp. 769–789. DOI: 10.1103/PhysRev.76.769.

[21] *Standard Model Summary Plots February 2022*. Tech. rep. Geneva: CERN, Mar. 2022. URL: https://cds.cern.ch/record/2804061.

[22] Wolfgang Pauli. *Niels Bohr and the development of physics; essays dedicated to Niels Bohr on the occasion of his seventieth birthday.* eng. London: Pergamon Press, 1955.

[23] David J. Gross and Frank Wilczek. "Ultraviolet Behavior of Non-Abelian Gauge Theories". In: *Phys. Rev. Lett.* 30 (26 June 1973), pp. 1343–1346. DOI: 10.1103/PhysRevLett.30.1343.

[24] G Altarelli. "Experimental Tests of Perturbative QCD". In: *Annual Review of Nuclear and Particle Science* 39.1 (1989), pp. 357–406. DOI: 10.1146/annurev.ns.39.120189.002041.

[25] J. J. Aubert et al. "Experimental Observation of a Heavy Particle J". In: *Phys. Rev. Lett.* 33 (23 Dec. 1974), pp. 1404–1406. DOI: 10.1103/PhysRevLett.33.1404.

[26] J. -E. Augustin et al. "Discovery of a Narrow Resonance in e^+e^- Annihilation". In: *Phys. Rev. Lett.* 33 (23 Dec. 1974), pp. 1406–1408. DOI: 10.1103/PhysRevLett.33.1406.

[27] C. E. Carlson and R. Suaya. "Hadronic Production of psi/J Mesons". In: *Phys. Rev. D* 14 (1976), p. 3115. DOI: 10.1103/PhysRevD.14.3115.

[28] A. Donnachie and P. V. Landshoff. "Production of Lepton Pairs, J/ψ and Charm with Hadron Beams". In: *Nucl. Phys. B* 112 (1976), pp. 233–255. DOI: 10.1016/0550-3213(76)90532-0.

[29] S. D. Ellis, Martin B. Einhorn, and C. Quigg. "Comment on Hadronic Production of Psions". In: *Phys. Rev. Lett.* 36 (1976), p. 1263. DOI: 10.1103/PhysRevLett.36.1263.

[30] F. Abe et al. "Inclusive J/ψ, ψ(2S), and b-quark production in $p\bar{p}$ collisions at $\sqrt{s} = 1.8$ TeV". In: *Phys. Rev. Lett.* 69 (26 Dec. 1992), pp. 3704–3708. DOI: 10.1103/PhysRevLett.69.3704.

[31] F. Abe et al. "J/ψ and $\psi(2S)$ Production in $p\bar{p}$ Collisions at $\sqrt{s} = 1.8$ TeV". In: *Phys. Rev. Lett.* 79 (4 July 1997), pp. 572–577. DOI: 10.1103/PhysRevLett.79.572.

[32] C. Albajar et al. "J/ψ and ψ' production at the CERN $p\bar{p}$ collider". In: *Physics Letters B* 256.1 (1991), pp. 112–120. DOI: 10.1016/0370-2693(91)90227-H.

[33] S. Abachi et al. "J/ψ production in pp collisions at s = 1.8 TeV". In: *Physics Letters B* 370.1 (1996), pp. 239–248. DOI: 10.1016/0370-2693(96)00067-6.

[34] Eric Braaten and Sean Fleming. "Color-Octet Fragmentation and the ψ' Surplus at the Fermilab Tevatron". In: *Phys. Rev. Lett.* 74 (17 Apr. 1995), pp. 3327–3330. DOI: 10.1103/PhysRevLett.74.3327.

[35] Peter Cho and Mark B. Wise. "Spin symmetry predictions for heavy quarkonia alignment". In: *Physics Letters B* 346.1 (1995), pp. 129–136. DOI: 10.1016/0370-2693(94)01658-Y.

[36] Matteo Cacciari et al. “Charmonium production at the Tevatron”. In: *Physics Letters B* 356.4 (1995), pp. 553–560. DOI: 10.1016/0370-2693(95)00868-L.

[37] Peter Cho and Adam K. Leibovich. “Color-octet quarkonia production”. In: *Phys. Rev. D* 53 (1 Jan. 1996), pp. 150–162. DOI: 10.1103/PhysRevD.53.150.

[38] Peter Cho and Adam K. Leibovich. “Color-octet quarkonia production. II”. In: *Phys. Rev. D* 53 (11 June 1996), pp. 6203–6217. DOI: 10.1103/PhysRevD.53.6203.

[39] Yan-Qing Ma, Kai Wang, and Kuang-Ta Chao. “A complete NLO calculation of the J/ψ and ψ' production at hadron colliders”. In: *Phys. Rev. D* 84 (2011), p. 114001. DOI: 10.1103/PhysRevD.84.114001.

[40] Bin Gong, Xue Qian Li, and Jian-Xiong Wang. “QCD corrections to J/ψ production via color octet states at Tevatron and LHC”. In: *Phys. Lett. B* 673 (2009). [Erratum: Phys.Lett.B 693, 612–613 (2010)], pp. 197–200. DOI: 10.1016/j.physletb.2009.02.026.

[41] Mathias Butenschoen and Bernd A. Kniehl. “Reconciling J/ψ production at HERA, RHIC, Tevatron, and LHC with NRQCD factorization at next-to-leading order”. In: *Phys. Rev. Lett.* 106 (2011), p. 022003. DOI: 10.1103/PhysRevLett.106.022003.

[42] Betty Abelev et al. “J/ψ polarization in pp collisions at $\sqrt{s} = 7$ TeV”. In: *Phys. Rev. Lett.* 108 (2012), p. 082001. DOI: 10.1103/PhysRevLett.108.082001.

[43] Serguei Chatrchyan et al. “Measurement of the Prompt J/ψ and $\psi(2S)$ Polarizations in pp Collisions at $\sqrt{s} = 7$ TeV”. In: *Phys. Lett. B* 727 (2013), pp. 381–402. DOI: 10.1016/j.physletb.2013.10.055.

[44] R Aaij et al. “Measurement of J/ψ polarization in pp collisions at $\sqrt{s} = 7$ TeV”. In: *Eur. Phys. J. C* 73.11 (2013), p. 2631. DOI: 10.1140/epjc/s10052-013-2631-3.

[45] V. Barger, S. Fleming, and R.J.N. Phillips. “Double gluon fragmentation to J/ψ pairs at the tevatron”. In: *Physics Letters B* 371.1 (1996), pp. 111–116. DOI: 10.1016/0370-2693(95)01592-2.

[46] Bernd A. Kniehl, Caesar P. Palisoc, and Lennart Zwirner. “Associated production of heavy quarkonia and electroweak bosons at present and future colliders”. In: *Phys. Rev. D* 66 (11 Dec. 2002), p. 114002. DOI: 10.1103/PhysRevD.66.114002.

[47] Gang Li et al. "QCD corrections to J/ψ production in association with a W-boson at the LHC". In: *Phys. Rev. D* 83 (2011), p. 014001. DOI: 10.1103/PhysRevD.83.014001.

[48] J. P. Lansberg and C. Lorce. "Reassessing the importance of the colour-singlet contributions to direct $J/\psi+W$ production at the LHC and the Tevatron". In: *Phys. Lett. B* 726 (2013). [Erratum: Phys.Lett.B 738, 529–529 (2014)], pp. 218–222. DOI: 10.1016/j.physletb.2013.07.059.

[49] Georges Aad et al. "Measurement of the production cross section of prompt J/ψ mesons in association with a $W^{\pm}$ boson in pp collisions at $\sqrt{s} = 7$ TeV with the ATLAS detector". In: *JHEP* 04 (2014), p. 172. DOI: 10.1007/JHEP04(2014)172.

[50] Morad Aaboud et al. "Measurement of J/ψ production in association with a $W^{\pm}$ boson with pp data at 8 TeV". In: *JHEP* 01 (2020), p. 095. DOI: 10.1007/JHEP01(2020)095.

[51] Paolo Bartalini and Jonathan Richard Gaunt. *Multiple parton interactions at the LHC*. Advanced series on directions in high energy physics. Singapore: World Scientific, 2019. DOI: 10.1142/10646.

[52] Armen Tumasyan et al. "Observation of triple J/ψ meson production in proton-proton collisions at $\sqrt{s} = 13$ TeV". In: (Nov. 2021). arXiv: 2111.05370 [hep-ex].

[53] "LHC Machine". In: *JINST* 3 (2008). Ed. by Lyndon Evans and Philip Bryant, S08001. DOI: 10.1088/1748-0221/3/08/S08001.

[54] Oliver Sim Brüning et al. *LHC Design Report*. CERN Yellow Reports: Monographs. Geneva: CERN, 2004. DOI: 10.5170/CERN-2004-003-V-1.

[55] Oliver Sim Brüning et al. *LHC Design Report*. CERN Yellow Reports: Monographs. Geneva: CERN, 2004. DOI: 10.5170/CERN-2004-003-V-2.

[56] Michael Benedikt et al. *LHC Design Report*. CERN Yellow Reports: Monographs. Geneva: CERN, 2004. DOI: 10.5170/CERN-2004-003-V-3.

[57] Ewa Lopienska. "The CERN accelerator complex, layout in 2022. Complexe des accélérateurs du CERN en janvier 2022". In: (Feb. 2022). General Photo. URL: https://cds.cern.ch/record/2800984.

[58] Wikimedia Commons. *A simplified diagram of an SRF cavity in a helium bath with RF coupling and a passing particle beam.* File: `SRF Cavity Diagram 1.png`. 2008.
[59] AC Team. "Schéma d'un aimant dipôle du LHC". June 1999. URL: `https://cds.cern.ch/record/40524`.
[60] D. Boussard and T. Linnecar. "The LHC Superconducting RF System". In: *Adv. Cryog. Eng. A* 45 (2000). Ed. by Q. S. Shu et al., pp. 835–844.
[61] G Papotti et al. "Longitudinal Beam measurements at the LHC: The LHC Beam Quality Monitor". In: (Nov. 2011), 3 p.
[62] The ATLAS Collaboration, G Aad, et al. "The ATLAS Experiment at the CERN Large Hadron Collider". In: *Journal of Instrumentation* 3.08 (Aug. 2008), S08003–S08003. DOI: `10.1088/1748-0221/3/08/s08003`.
[63] S Chatrchyan, G Hmayakyan, V Khachatryan, et al. "The CMS experiment at the CERN LHC. The Compact Muon Solenoid experiment". In: *JINST* 3 (2008). Also published by CERN Geneva in 2010, S08004. 361 p. DOI: `10.1088/1748-0221/3/08/S08004`.
[64] K. Aamodt et al. "The ALICE experiment at the CERN LHC". In: *JINST* 3 (2008), S08002. DOI: `10.1088/1748-0221/3/08/S08002`.
[65] A Augusto Alves, L M Andrade, F Barbosa-Ademarlaudo, et al. "The LHCb Detector at the LHC". In: *JINST* 3 (2008). Also published by CERN Geneva in 2010, S08005. DOI: `10.1088/1748-0221/3/08/S08005`.
[66] G. Avoni et al. "The new LUCID-2 detector for luminosity measurement and monitoring in ATLAS". In: *JINST* 13.07 (2018), P07017. DOI: `10.1088/1748-0221/13/07/P07017`.
[67] *Luminosity determination in pp collisions at $\sqrt{s} = 13$ TeV using the ATLAS detector at the LHC*. Tech. rep. Geneva: CERN, June 2019. URL: `https://cds.cern.ch/record/2677054`.
[68] S van der Meer. *Calibration of the effective beam height in the ISR*. Tech. rep. Geneva: CERN, 1968. URL: `https://cds.cern.ch/record/296752`.
[69] Adomeit, Stefanie. "Hard And Soft QCD Physics In ATLAS". In: *EPJ Web of Conferences* 70 (2014), p. 00030. DOI: `10.1051/epjconf/20147000030`.
[70] *ATLAS magnet system: Technical Design Report, 1*. Technical design report. ATLAS. Geneva: CERN, 1997. DOI: `10.17181/CERN.905C.VDTM`.

[71] Tiago Barreiro Goncalves. “3D Printing the ATLAS’ barrel toroid”. In: (Aug. 2016).
[72] *ATLAS inner detector: Technical Design Report, 1*. Technical design report. ATLAS. Geneva: CERN, 1997. URL: https://cds.cern.ch/record/331063.
[73] S Haywood et al. *ATLAS inner detector: Technical Design Report, 2*. Technical design report. ATLAS. Geneva: CERN, 1997. URL: https://cds.cern.ch/record/331064.
[74] Norbert Wermes and G Hallewel. *ATLAS pixel detector: Technical Design Report*. Technical design report. ATLAS. Geneva: CERN, 1998. URL: http://cds.cern.ch/record/381263.
[75] Y Unno. “ATLAS silicon microstrip detector system (SCT)”. In: *Nuclear Instruments and Methods in Physics Research Section A: Accelerators, Spectrometers, Detectors and Associated Equipment* 511.1 (2003). Proceedings of the 11th International Workshop on Vertex Detectors, pp. 58–63. DOI: https://doi.org/10.1016/S0168-9002(03)01751-0.
[76] The ATLAS TRT collaboration. “The ATLAS Transition Radiation Tracker (TRT) proportional drift tube: design and performance”. In: *Journal of Instrumentation* 3.02 (Feb. 2008), P02013–P02013. DOI: 10.1088/1748-0221/3/02/p02013.
[77] *ATLAS liquid-argon calorimeter: Technical Design Report*. Technical design report. ATLAS. Geneva: CERN, 1996. DOI: 10.17181/CERN.FWRW.FOOQ.
[78] *ATLAS tile calorimeter: Technical Design Report*. Technical design report. ATLAS. Geneva: CERN, 1996. DOI: 10.17181/CERN.JRBJ.7O28.
[79] A Artamonov, D Bailey, G Belanger, et al. “The ATLAS Forward Calorimeter”. In: *Journal of Instrumentation* 3.02 (Feb. 2008), P02010–P02010. DOI: 10.1088/1748-0221/3/02/p02010.
[80] Morad Aaboud et al. “Performance of the ATLAS Trigger System in 2015”. In: *Eur. Phys. J. C* 77.5 (2017), p. 317. DOI: 10.1140/epjc/s10052-017-4852-3.
[81] Georges Aad et al. “Operation of the ATLAS trigger system in Run 2”. In: *JINST* 15.10 (2020), P10004. DOI: 10.1088/1748-0221/15/10/P10004.
[82] Peter Jenni et al. *ATLAS high-level trigger, data-acquisition and controls: Technical Design Report*. Technical design report. ATLAS. Geneva: CERN, 2003. URL: https://cds.cern.ch/record/616089.

[83] T Cornelissen et al. *Concepts, Design and Implementation of the ATLAS New Tracking (NEWT).* Tech. rep. Geneva: CERN, Mar. 2007. URL: `https://cds.cern.ch/record/1020106`.

[84] G. Aad, B. Abbott, J. Abdallah, et al. "Topological cell clustering in the ATLAS calorimeters and its performance in LHC Run 1". In: *The European Physical Journal C* 77.7 (2017), p. 490. DOI: `10.1140/epjc/s10052-017-5004-5`.

[85] Morad Aaboud et al. "Electron reconstruction and identification in the ATLAS experiment using the 2015 and 2016 LHC proton-proton collision data at $\sqrt{s} = 13$ TeV". In: *Eur. Phys. J. C* 79.8 (2019), p. 639. DOI: `10.1140/epjc/s10052-019-7140-6`.

[86] Georges Aad et al. "Electron and photon performance measurements with the ATLAS detector using the 2015–2017 LHC proton-proton collision data". In: *JINST* 14.12 (2019), P12006. DOI: `10.1088/1748-0221/14/12/P12006`.

[87] Georges Aad et al. "Muon reconstruction and identification efficiency in ATLAS using the full Run 2 *pp* collision data set at $\sqrt{s} = 13$ TeV". In: *Eur. Phys. J. C* 81.7 (2021), p. 578. DOI: `10.1140/epjc/s10052-021-09233-2`.

[88] Morad Aaboud et al. "Performance of missing transverse momentum reconstruction with the ATLAS detector using proton-proton collisions at $\sqrt{s} = 13$ TeV". In: *Eur. Phys. J. C* 78.11 (2018), p. 903. DOI: `10.1140/epjc/s10052-018-6288-9`.

[89] Johan Alwall et al. "MadGraph 5: going beyond". In: *Journal of High Energy Physics* 2011.6 (2011), p. 128. DOI: `10.1007/JHEP06(2011)128`.

[90] Paolo Nason. "A New method for combining NLO QCD with shower Monte Carlo algorithms". In: *JHEP* 11 (2004), p. 040. DOI: `10.1088/1126-6708/2004/11/040`.

[91] Stefano Frixione, Paolo Nason, and Carlo Oleari. "Matching NLO QCD computations with Parton Shower simulations: the POWHEG method". In: *JHEP* 11 (2007), p. 070. DOI: `10.1088/1126-6708/2007/11/070`.

[92] Simone Alioli et al. "A general framework for implementing NLO calculations in shower Monte Carlo programs: the POWHEG BOX". In: *JHEP* 06 (2010), p. 043. DOI: `10.1007/JHEP06(2010)043`.

[93] Johan Alwall et al. "A Standard format for Les Houches event files". In: *Comput. Phys. Commun.* 176 (2007), pp. 300–304. DOI: `10.1016/j.cpc.2006.11.010`.

[94] E. Boos et al. "Generic User Process Interface for Event Generators". In: *2nd Les Houches Workshop on Physics at TeV Colliders*. Sept. 2001. arXiv: hep-ph/0109068.

[95] Torbjorn Sjostrand, Stephen Mrenna, and Peter Z. Skands. "PYTHIA 6.4 Physics and Manual". In: *JHEP* 05 (2006), p. 026. DOI: 10.1088/1126-6708/2006/05/026.

[96] Torbjörn Sjöstrand et al. "An introduction to PYTHIA 8.2". In: *Comput. Phys. Commun.* 191 (2015), pp. 159–177. DOI: 10.1016/j.cpc.2015.01.024.

[97] G. Corcella et al. "HERWIG 6: An Event generator for hadron emission reactions with interfering gluons (including supersymmetric processes)". In: *JHEP* 01 (2001), p. 010. DOI: 10.1088/1126-6708/2001/01/010.

[98] M. Bahr et al. "Herwig++ Physics and Manual". In: *Eur. Phys. J. C* 58 (2008), pp. 639–707. DOI: 10.1140/epjc/s10052-008-0798-9.

[99] Johannes Bellm et al. "Herwig 7.0/Herwig++ 3.0 release note". In: *Eur. Phys. J. C* 76.4 (2016), p. 196. DOI: 10.1140/epjc/s10052-016-4018-8.

[100] T. Gleisberg et al. "Event generation with SHERPA 1.1". In: *JHEP* 02 (2009), p. 007. DOI: 10.1088/1126-6708/2009/02/007.

[101] G. Aad et al. "The ATLAS Simulation Infrastructure". In: *Eur. Phys. J. C* 70 (2010), pp. 823–874. DOI: 10.1140/epjc/s10052-010-1429-9.

[102] S. Agostinelli et al. "GEANT4–a simulation toolkit". In: *Nucl. Instrum. Meth. A* 506 (2003), pp. 250–303. DOI: 10.1016/S0168-9002(03)01368-8.

[103] Morad Aaboud et al. "Study of the material of the ATLAS inner detector for Run 2 of the LHC". In: *JINST* 12.12 (2017), P12009. DOI: 10.1088/1748-0221/12/12/P12009.

[104] *The new Fast Calorimeter Simulation in ATLAS*. Tech. rep. Geneva: CERN, July 2018. URL: https://cds.cern.ch/record/2630434.

[105] *ATLAS Pythia 8 tunes to 7 TeV data*. Tech. rep. Geneva: CERN, Nov. 2014. URL: https://cds.cern.ch/record/1966419.

[106] J. Pumplin et al. "New generation of parton distributions with uncertainties from global QCD analysis". In: *JHEP* 07 (2002), p. 012. DOI: 10.1088/1126-6708/2002/07/012.

[107] Stefano Carrazza, Stefano Forte, and Juan Rojo. "Parton Distributions and Event Generators". In: *43rd International Symposium on Multiparticle Dynamics*. 2013, pp. 89–96. arXiv: 1311.5887 [hep-ph].

[108] Pierre Artoisenet, Fabio Maltoni, and Tim Stelzer. "Automatic generation of quarkonium amplitudes in NRQCD". In: *Journal of High Energy Physics* 2008.02 (Feb. 2008), pp. 102–102. DOI: 10.1088/1126-6708/2008/02/102.

[109] Hua-Sheng Shao. "HELAC-Onia 2.0: an upgraded matrix-element and event generator for heavy quarkonium physics". In: *Comput. Phys. Commun.* 198 (2016), pp. 238–259. DOI: 10.1016/j.cpc.2015.09.011.

[110] Estia J. Eichten and Chris Quigg. "Quarkonium wave functions at the origin". In: *Phys. Rev. D* 52 (3 Aug. 1995), pp. 1726–1728. DOI: 10.1103/PhysRevD.52.1726.

[111] Mathias Butenschoen and Bernd A. Kniehl. "J/psi polarization analyses in NLO NRQCD". In: *PoS* ConfinementX (2012). Ed. by Matthias Berwein, Nora Brambilla, and Stephan Paul, p. 129. DOI: 10.22323/1.171.0129.

[112] Mathias Butenschoen and Bernd A. Kniehl. "Fits of $\psi(2S)$ NRQCD LDMEs to global hadroproduction data at NLO". In: (July 2022). arXiv: 2207.09346 [hep-ph].

[113] Yan-Qing Ma, Kai Wang, and Kuang-Ta Chao. "QCD radiative corrections to χ_{cJ} production at hadron colliders". In: *Phys. Rev. D* 83 (2011), p. 111503. DOI: 10.1103/PhysRevD.83.111503.

[114] Bin Gong et al. "Polarization for Prompt J/ψ and ψ(2s) Production at the Tevatron and LHC". In: *Phys. Rev. Lett.* 110.4 (2013), p. 042002. DOI: 10.1103/PhysRevLett.110.042002.

[115] Geoffrey T. Bodwin et al. "Fragmentation contributions to hadroproduction of promptJ/ψ, χ_{cJ}, and $\psi(2S)$ states". In: *Phys. Rev. D* 93.3 (2016), p. 034041. DOI: 10.1103/PhysRevD.93.034041.

[116] Nora Brambilla et al. "Production and polarization of S-wave quarkonia in potential nonrelativistic QCD". In: *Phys. Rev. D* 105 (11 June 2022), p. L111503. DOI: 10.1103/PhysRevD.105.L111503.

[117] Mathias Butenschoen and Bernd A. Kniehl. "New constraints on NRQCD long-distance matrix elements from J/ψ plus W/Z production at the CERN LHC". In: (July 2022). arXiv: 2207.09366 [hep-ph].

[118] ATLAS Collaboration. "Performance of electron and photon triggers in ATLAS during LHC Run 2". In: *Eur. Phys. J. C* 80 (2020), p. 47. DOI: 10.1140/epjc/s10052-019-7500-2.

[119] ATLAS Collaboration. "Performance of the ATLAS muon triggers in Run 2". In: *JINST* 15 (2020), P09015. DOI: 10.1088/1748-0221/15/09/p09015.

[120] Rustem Ospanov, Rhys Thomas Roberts, and Terry Richard Wyatt. *Tagging non-prompt electrons and muons*. Tech. rep. Geneva: CERN, Oct. 2016. URL: https://cds.cern.ch/record/2220954.

[121] M. Pivk and F.R. Le Diberder. "sPlots: A statistical tool to unfold data distributions". In: *Nuclear Instruments and Methods in Physics Research Section A: Accelerators, Spectrometers, Detectors and Associated Equipment* 555.1 (2005), pp. 356–369. DOI: https://doi.org/10.1016/j.nima.2005.08.106.

[122] Paolo Bartalini and Jonathan Richard Gaunt, eds. *Multiple Parton Interactions at the LHC*. Vol. 29. WSP, 2019. DOI: 10.1142/10646.

Vita

Charles D. Burton was born in Mayfield Heights, Ohio on 13 June 1994, the son of Mr. and Mrs. Jay and Brenda Burton. He received Bachelor of Arts degrees in Physics and Mathematics from Cornell University in Ithaca, New York in May 2016. He applied to the PhD program of the Physics Department at The University of Texas in Austin, Texas, was accepted, and started graduate studies in August 2016. As a PhD student, he joined the ATLAS Collaboration, contributing to measurements of heavy quarkonia production and the top quark mass. He developed software for the ATLAS Data Quality group and performed LAr Calorimeter electronics upgrade research, which will be installed for the HL-LHC.

Address: burton@utexas.edu

This dissertation was typeset with LaTeX by the author.